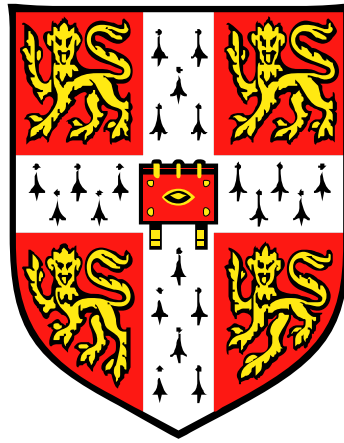


Integration of liquid crystals with redox electrolytes in dye-sensitised solar cells



A thesis submitted for the degree of doctor of philosophy

by

Muhammad Akmal Bin Kamarudin

St. John's College

Department of Engineering

Electrical Engineering

University of Cambridge

February 2017

Abstract

Integration of liquid crystals with redox electrolytes in dye-sensitised solar cells

Muhammad Akmal Bin Kamarudin

This thesis examines the electro-optic, electric and electrochemical properties of liquid crystal (LC) materials in self-assembly systems, that is, liquid crystal-polymer electrolyte composites (LC-PEs), LC binary mixtures, and their potential application in dye-sensitised solar cells (DSSCs). The birefringence of LCs causes light modulation, which can be controlled by an applied voltage and electric field. In particular, the LCs are used as one of the components for the electrolyte redox couple which is responsible for charge transfer mechanism in DSSCs.

In this work, LC-PEs were developed by dissolving LCs in polymer electrolytes; using a homologous series of cyanobiphenyls in a range of concentrations, alkyl chain lengths and dielectric permittivities. We found that doping the polymer electrolyte with 15% 4'-cyano-4'-pentylbiphenyl (5CB) improved ionic conductivity by up to 13 % compared to pure polymer electrolyte. Materials with positive dielectric permittivity and shorter alkyl chain length have been identified to be compatible with iodide/triiodide (I^-/I_3^-)-based polymer electrolytes. In DSSCs, 15% 5CB and 15% E7 LC-PEs exhibited the best efficiencies of 3.6 % and 4.0 %, respectively.

In addition to LC-PEs, the self-assembly properties of smectic phase LCs were also utilised as templates for controlling the polymer structure in polymer electrolytes. A porous polymer network was prepared using various techniques including self-assembly, by applying an electric field and using a polyimide (PI) alignment layer. We found that the electrochemical and photovoltaic properties of these materials strongly correlated to the morphology/structure with the self-assembled structure, thus showing the best photovoltaic performance (5.9 %) even when compared with a reference solar cell (4.97 %).

Finally, this thesis explores the interaction of LCs with graphene (Gr) in DSSC device architectures. Gr-based DSSCs were fabricated using different processing conditions, with the result being that Gr improved the performance of the DSSCs. The highest efficiency

obtained was 5.48 % compared to the 4.86 % of a reference DSSC. The incorporation of LC-PEs in Gr-based DSSCs improved the performance of DSSCs was observed in devices with low concentrations of LCs due to the Gr inducing planar alignment of LCs.

These results suggest a new strategy to improve DSSC efficiency by incorporating LC materials in the polymer electrolyte component. Even though these LCs are highly insulating, their self-assembly and dielectric polarisability help enhance ionic conductivity and optical scattering when doped into polymer electrolytes. This work can be extended in a fundamental way to elucidate the ionic conduction mechanism of LC-based electrolyte systems. Furthermore, it would be interesting if the benefits of using LC-PEs and smectic-templated polymer electrolytes (Sm-Pes) can be translated further in commercial electrochemical energy conversion systems.

Declaration

This thesis is the result of the work done by the author whilst registered for postgraduate candidature at the University of Cambridge. The work is entirely original except where due reference is made, and no portion of the work referred to in this thesis has been submitted in support of an application for another degree or qualification at this or any other university or institute of learning.

This thesis contains 42,523 words and 79 figures which do not exceed the limits set by the Department of Engineering.

Acknowledgements

I would like to express my gratitude to several people, without whom this work would not have been possible.

First and foremost, I would like to express my deepest gratitude to my supervisor, Prof. Timothy Wilkinson for giving me the freedom of exploring my research interest. Tim has been very supportive and patience throughout this research despite my lack of knowledge on the subject.

For day-to-day supervision and guidance, I must thank Dr. Malik Qasim. Malik has endlessly giving me advice and insightful ideas for my research. He has also giving me direction as to where my research should be focused on.

I would also like to thank Prof. Suhana Mohd Said for giving the support and guidance throughout my PhD. She has been kind enough to proofread this thesis and gave me valuable suggestions to improve this thesis.

I would also like to thank all the CMMPE research group members during my time there for making the labs a very entertaining place to spend three years. Especially to Ammar Khan who had been very patient putting up with my stupid questions, lame jokes and mood swings. Thanks also to Alex Macfaden, Amalya Konstanyan, Calum Williams, James Dolan, Jennifer Jones, Richard Barthlomew, Rachel Garsed and Shabeena Nosheen.

Also, million thanks to these people: Hazwan Daut for all the countless trips to the city centre and impromptu trips to London. Asyraf Nazmi for the awesome trip to Switzerland and for putting up with all my silly requests. Amer Izzat for the movie nights, karaoke sessions and ski-trip. Norhayati Idros for being a sister figure to me. Edward Tan and Girish Rughoobur for stopping by at my desk every single day and for all the gossips. Hassan Mohamed and family, Nik Hafidzi, Zurina Mokhtar, Zuraidah Zobir, Norbaya Ahmad, Ummi Abdullah and Fathullah Nawawi for feeding me with good food and making my Cambridge experience ever more exciting!

Most of all, I would like to thank my family who has been there from the very beginning, who has given me the utmost support, encouragement and love throughout my life.

Table of Contents

Abstract	i
Declaration	iii
Acknowledgements	iv
Table of Contents	v
List of Figures	x
List of Tables	xiii
List of Abbreviations	xiv
List of Publications	xix
Chapter 1 Introduction	- 1 -
1.1 Background	- 1 -
1.2 Outline	- 3 -
Chapter 2 Literature review and theory	- 6 -
2.1 Foreword	- 6 -
2.2.1 Lyotropic liquid crystals	- 6 -
2.2.2 Thermotropic liquid crystals	- 7 -
2.2.3 Reactive mesogens	- 12 -
2.2.4 Polymer dispersed liquid crystals	- 13 -
2.2.5.1 Dielectric anisotropies	- 14 -
2.2.5.2 Birefringence	- 15 -
2.2.5.3 Diamagnetic anisotropy	- 16 -
2.2.5.4 Conductivity anisotropy	- 17 -
2.2.5.5 Fluid viscosity	- 17 -
2.2.5.6 Alignment layers	- 18 -
2.2.5.7 Elastic constants	- 19 -
2.3 Solar cells	- 25 -
2.3.1 Introduction	- 25 -

2.3.2 Introduction to DSSCs	- 27 -
2.3.3 Working principle	- 28 -
2.3.4 Electrolytes	- 29 -
2.3.5 Counter electrodes	- 34 -
2.4 Summary	- 35 -
Chapter 3 Materials and Experimental Methods	- 36 -
3.1 Foreword	- 36 -
3.2 Fabrication	- 36 -
3.2.1 LC cell fabrication	- 36 -
3.2.2 DSSC fabrication	- 37 -
3.2.3 LC-PEs preparation	- 41 -
3.2.4 LC binary mixture preparation	- 41 -
3.2.5 LC template preparation	- 42 -
3.3 Characterisations	- 43 -
3.3.1 Polarising Optical Microscopy	- 43 -
3.3.2 Differential Scanning Calorimetry	- 44 -
3.3.3 Ultraviolet-Visible spectroscopy	- 44 -
3.3.4 Fourier transformed infra-red spectroscopy	- 45 -
3.3.5 Scanning electron microscopy	- 45 -
3.3.5 Atomic force microscopy	- 46 -
3.3.6 Dielectric permittivity	- 46 -
3.3.7 Current-Voltage conductivity measurement	- 47 -
3.3.8 Linear sweep voltammetry	- 47 -
3.3.9 Light scattering	- 48 -
3.3.10 Photovoltaic parameters	- 48 -
3.3.11 Electrochemical Impedance Spectroscopy	- 50 -
3.4 Summary	- 51 -

Chapter 4 Device development	- 52 -
4.1 Foreword	- 52 -
4.2 Effect of different electrolytes	- 52 -
4.3 Effect of different spacers and sealants	- 54 -
4.4 Effect of different compact layers	- 56 -
4.6 Effect of dye immersion	- 58 -
4.7 Optimised device structure	- 59 -
4.7 Summary	- 60 -
Chapter 5 Liquid crystal-polymer composite electrolytes	- 61 -
5.1 Foreword	- 61 -
5.2 Different variations of LC content	- 61 -
5.2.1 Polarising optical microscopy	- 61 -
5.2.2 Differential scanning calorimetry	- 63 -
5.2.3 Current-Voltage measurements	- 64 -
5.2.4 Light scattering effect	- 67 -
5.2.5 Photovoltaic properties	- 69 -
5.2.6 Impedance spectroscopy	- 70 -
5.3 LC with different alkyl chain lengths	- 73 -
5.3.1 Polarising optical microscopy	- 73 -
5.3.2 Differential scanning calorimetry	- 76 -
5.3.3 Current-Voltage measurement	- 77 -
5.3.4 Photovoltaic properties	- 79 -
5.3.5 Electrochemical Impedance Spectroscopy	- 81 -
5.4 Effect of dielectric permittivity	- 83 -
5.4.1 Dielectric permittivities	- 83 -
5.4.2 Polarising optical microscopy	- 85 -
5.4.3 Current-Voltage measurement	- 86 -

5.4.4 Photovoltaic properties	- 88 -
5.4.5 Electrochemical impedance spectroscopy	- 89 -
5.5 Summary	- 91 -
Chapter 6 Liquid crystalline templates	- 93 -
6.1 Foreword	- 93 -
6.2 Highly ordered polymer template using optimised NLC:SmA binary mixture	- 94 -
6.2.1 Preparation of optimised NLC:SmA binary mixture	- 94 -
6.2.2 Preparation of LC template	- 97 -
6.2.3 Fourier-transform infrared spectroscopy	- 99 -
6.2.4 Morphology and structure characterisation	- 99 -
6.2.5 Current-Voltage measurements	- 100 -
6.2.6 Light scattering	- 102 -
6.2.7 Photovoltaic properties	- 104 -
6.2.8 Electrochemical Impedance Spectroscopy	- 105 -
6.3 Control of LC template alignment	- 106 -
6.3.3 Preparation of LC template through the application of E	- 106 -
6.3.4 Preparation of LC template using PI alignment layer	- 108 -
6.3.5 Current-Voltage measurement	- 109 -
6.3.6 Photovoltaic properties	- 111 -
6.3.7 Electrochemical impedance spectroscopy	- 112 -
6.4 Conclusion	- 113 -
Chapter 7 Graphene counter electrodes	- 115 -
7.1 Foreword	- 115 -
7.2 Interaction of LCs with graphene	- 115 -
7.3 Graphene counter electrode DSSCs	- 116 -
7.3.1 Comparison of different graphene-based electrodes	- 116 -
7.3.2 Photovoltaic properties	- 118 -

7.3 Interaction of LC-PEs with graphene electrode	- 120 -
7.3.1 Polarising optical microscopy	- 120 -
7.4.2 Photovoltaic properties	- 121 -
7.4.3 Electrochemical impedance spectroscopy	- 123 -
7.5 Summary	- 124 -
Chapter 8 Conclusion and Future Work	- 125 -
8.1 Conclusion	- 125 -
8.2 Future work	- 126 -
8.2.1 Doping of liquid electrolyte with alkoxy cyanobiphenyl LCs	- 126 -
8.2.2 LC-templating with DLCs	- 126 -
8.2.3 DLC template with graphene electrode	- 127 -
8.2.4 Thermoelectric devices	- 127 -
8.2.5 Batteries	- 128 -

List of Figures

Figure 2.1 Schematic diagram of micelle formation in water.....	- 7 -
Figure 2.2 Schematic diagram of thermotropic LCs as a function of temperature.	- 8 -
Figure 2.3 a) Schematic diagram of a single LC molecule showing the director.....	- 9 -
Figure 2.4 a) Schematic representation of the SmA phase... Error! Bookmark not defined.	
Figure 2.5 a) Schematic diagram of a columnar DLC where the molecules.....	- 12 -
Figure 2.6 Chemical structure of some reactive mesogens. a) RM 82 and b) RM 21.	- 13 -
Figure 2.7 Schematic diagram of PDLC device a) before and b) after applying E	- 14 -
Figure 2.8 Dielectric permittivity as a function of temperature of a nematic LC.	- 15 -
Figure 2.9 Schematic diagram of an LC molecule showing the different refractive.....	- 15 -
Figure 2.10 Schematic diagram showing the effect of H a) parallel	- 17 -
Figure 2.11 Schematic diagram of the measurement to determine the shear viscosity	- 18 -
Figure 2.12 Schematic diagram of the a) homeotropic and b) planar alignment	- 19 -
Figure 2.13 Schematic diagram of the various deformation modes in LC materials.....	- 19 -
Figure 2.14 Energy level diagram of a bilayer OLED.....	- 21 -
Figure 2.15 Schematic diagram of a a) p-type and b) n-type OFET.....	- 22 -
Figure 2.16 a) Schematic diagram of a polychromatic LC laser.....	- 23 -
Figure 2.17 Energy level diagram of a heterojunction organic solar cell.....	- 24 -
Figure 2.18 World's energy consumption according to different regions	- 26 -
Figure 2.19 Energy generation according to different energy sources	- 26 -
Figure 2.20 Schematic diagram of a typical DSSC.....	- 28 -
Figure 2.21 Schematic diagram showing the working principle of a working DSSC	- 29 -
Figure 2.22 Chemical structure of spiro-OMeTAD.....	- 31 -
Figure 2.23 Ionic conduction mechanism of a polymer electrolyte.....	- 33 -
Figure 3.1 Schematic diagram of wet transfer process of graphene on a substrate.....	- 40 -
Figure 3.2 Chemical structures of the homologous cyanobiphenyl LCs.....	- 41 -
Figure 3.3 Chemical structures of a) E7 and b) 8/2 organosiloxane.	- 42 -
Figure 3.4 Schematic diagram of the preparation of LC template.	- 42 -
Figure 3.5 Chemical structures of the reactive mesogen and the photoinitiator	- 43 -
Figure 3.6 Schematic diagram of a POM.	- 44 -
Figure 3.7 Schematic diagram of the light scattering setup.	- 48 -
Figure 3.8 a) Typical $J-V$ curve of a solar cell under light soaking	- 49 -
Figure 3.9 A typical EIS curve of a solar device measured at a specific point.	- 50 -

Figure 3.10 Equivalent circuit for liquid junction DSSC	51 -
Figure 4.1 $J-V$ curves of DSSCs using different liquid electrolytes.	54 -
Figure 4.2 $J-V$ curves of DSSCs using different spacers/sealants.	55 -
Figure 4.3 $J-V$ curves of DSSCs using different compact layers.....	57 -
Figure 4.4 UV-Vis plot of N719 dye solution before and after immersion.....	59 -
Figure 4.5 $J-V$ curve of the optimised DSSC under light soaking.	60 -
Figure 5.1 POM images of a) pure polymer electrolyte and LC-PEs.	63 -
Figure 5.2 Chemical structure of the DMPII ionic liquid.	63 -
Figure 5.3 DSC curves of pure polymer electrolyte and 5CB-doped.	64 -
Figure 5.4 Steady-state voltammogram of different polymer electrolyte composition.	65 -
Figure 5.5 Plot of a) ionic conductivity and b) VTF as a function of temperature	67 -
Figure 5.6 Scattering image projected in the far-field with different polymer.....	68 -
Figure 5.7 a) Light and b) dark $J-V$ curves of DSSC.....	69 -
Figure 5.8 a) Nyquist and b) Bode plot of the DSSCs employing LC-PEs.	72 -
Figure 5.9 Optical micrographs of pure LC materials.....	74 -
Figure 5.10 DSC curves of LC-PEs.....	76 -
Figure 5.11 Plot of a) ionic conductivity across different LC materials	78 -
Figure 5.12 Linear sweep voltammetry of LC-PEs.	78 -
Figure 5.13 a) Dark and b) light $J-V$ curves of DSSCs using polymer electrolytes	79 -
Figure 5.14 Schematic diagram of LC adsorption onto TiO_2 in a) 5CB and b) 10CB.....	81 -
Figure 5.15 Impedance spectra of the DSSCs employing the LC-PEs..	81 -
Figure 5.16 Dielectric permittivity of the different samples	84 -
Figure 5.17 Schematic representation of a) positive dielectric permittivity LC.....	85 -
Figure 5.18 POM micrographs of capillary filled LC-PEs in $9\ \mu\text{m}$ ITO cell.....	86 -
Figure 5.19 a) Ionic conductivity as a function of temperature and b) Arrhenius plot	87 -
Figure 5.20 $J-V$ curves of the photovoltaic devices fabricated with LC-PEs	89 -
Figure 5.21 Nyquist plot and b) Bode plot of the photovoltaic devices	91 -
Figure 6.1 a) DSC curves under heating at 5°C min^{-1} and b) phase diagram.	95 -
Figure 6.2 POM micrographs of LC mixture at different 8/2:E7 ratio.	97 -
Figure 6.3 POM micrographs of SmA:E7 mixture with RM 257 and IR 819.....	98 -
Figure 6.4 FTIR spectra of the different components of the pure E7.....	99 -
Figure 6.5 a) SEM image of LC-templated polymer with a thin layer of chromium.....	100 -
Figure 6.6 Steady-state voltammetry curve of the reference electrolyte and Sm-PE. ...	101 -
Figure 6.7 Light scattering profile of a) empty cell, b) cell filled with liquid electrolyte	103 -

Figure 6.8 J - V curves of DSSC with reference liquid electrolyte.....	- 105 -
Figure 6.9 a) Nyquist and b) Bode plot of DSSCs measured under dark	- 106 -
Figure 6.10 POM images of reactive mesogen mixtures after applying E	- 107 -
Figure 6.11 POM images of reactive mesogen mixtures with PI alignment layer.	- 109 -
Figure 6.12 Linear sweep voltammetry curve of E aligned sample and PI aligned	- 110 -
Figure 6.13 a) Light and b) dark J - V of the best performing solar devices.....	- 111 -
Figure 6.14 a) Nyquist plot and b) Bode plot.....	- 113 -
Figure 7.1 POM images of BL006 spin-coated onto a) graphene electrode.....	- 116 -
Figure 7.2 Raman spectroscopy of graphene on different electrodes	- 117 -
Figure 7.3 J - V curves for different photocathode configurations.	- 118 -
Figure 7.4 POM images of LC-PEs in Gr-ITO cell observed from the graphene side -	121 -
Figure 7.5 J - V curves of Gr-based DSSCs using pure polymer electrolyte.....	- 122 -
Figure 7.6 a) Nyquist plot and b) Bode plot of the photovoltaic devices.....	- 123 -

List of Tables

Table 4.1 Different components of the three different electrolytes.	53 -
Table 4.2 Result of DSSCs using different liquid electrolytes.	54 -
Table 4.3 Result of DSSCs using different spacers.	55 -
Table 4.4 Different compositions of compact layer mixtures.	56 -
Table 4.5 Result of DSSCs using different compact layers.	58 -
Table 5.1 Ionic diffusion and conductivity data for LC-PEs.	65 -
Table 5.2 Photovoltaic performance of the DSSCs	70 -
Table 5.3 Summary of charge resistance at interfaces and electron lifetime.....	72 -
Table 5.4 Transition temperatures of the different alkyl-cyanobiphenyl LCs	77 -
Table 5.5 Summary of the ionic conductivity for different LC-PEs.....	79 -
Table 5.6 Photovoltaic performance of DSSCs based on LC-PEs.....	80 -
Table 5.7 of the charge resistances and electron lifetime for different LC-PEs.	83 -
Table 5.8 Photovoltaic performance of DSSCs	89 -
Table 5.9 Summary of EIS parameters for DSSCs incorporating LCs.	90 -
Table 6.1 Ionic conductivity data for reference liquid electrolyte and electrolyten.	102 -
Table 6.2 Photovoltaic performance of DSSCs based on reference liquid electrolyte . -	104 -
Table 6.3 Summary of EIS parameters for liquid electrolyte and Sm-PE DSSCs.	105 -
Table 6.4 Ionic diffusion and conductivity data of E aligned sample.....	110 -
Table 6.5 Photovoltaic properties of DSSC devices prepared using E aligned.....	111 -
Table 6.6 Summary of EIS parameters for E aligned and PI aligned.....	112 -
Table 7.1 Summary of photovoltaic parameters for different photoanode.....	118 -
Table 7.2 Photovoltaic performance of the Gr-based DSSCs.....	122 -
Table 7.3 Electron lifetime at different 5CB composition	124 -

List of Abbreviations

5CB	4-cyano-4'-pentylbiphenyl
6CB	4-cyano-4'-hexylbiphenyl
7CB	4-cyano-4'-heptylbiphenyl
9CB	4-cyano-4'-nonylbiphenyl
10CB	4-cyano-4'-decylbiphenyl
12CB	4-cyano-4'-dodecylbiphenyl
AFM	Atomic force microscopy
BuOH	Butyl alcohol
CdTe	Cadmium teluride
CIGS	Copper indium gallium selenide
C_{Pt}	Capacitance at the platinum electrode
C_{TCO}	Capacitance at the TCO
CuI	Copper iodide
CVD	Chemical vapour deposition
DLC	Discotic liquid crystal
DMAP	4-dimethylaminopyridine
DMPII	1, 2-dimethyl-3-propylimidazolium iodide
DSC	Differential scanning calorimetry
DSSC	Dye-sensitised solar cell
<i>E</i>	Electric field
E_{F}	Fermi energy
EIS	Electrochemical impedance spectroscopy

ETL	Electron transporting layer
<i>F</i>	Free energy density
FF	Fill factor
FTIR	Fourier-transformed infra-red
FTO	Fluorine-doped tin oxide
GBL	γ -butyrolactone
GPE	Gel polymer electrolyte
Gr	Graphene
H	Magnetic field
HAT6	2, 3, 6, 7, 10, 11-hexakis(hexyloxy)triphenylene
HCl	Hydrochloric acid
HOMO	Highest occupied molecular orbital
HTL	Hole transporting layer
I^-/I_3^-	Iodide/triiodide
I_2	Iodine
IP	Ionisation potential
IPA	Isopropyl alcohol
IR	Bis(2, 4, 6-trimethylbenzoyl)-phenylphosphineoxide
ITO	Indium-doped tin oxide
$I-V$	Current-Voltage
J_{lim}	Limiting current density
J_{sc}	Short-circuit current density
$J-V$	Current density-voltage

K	Crystal
K_{11}	Splay elastic constant
K_{22}	Twist elastic constant
K_{33}	Bend elastic constant
LC	Liquid crystal
LC-PC	Liquid crystal polymer composite
LC-PE	Liquid crystal polymer electrolyte
LED	Light emitting diode
LiI	Lithium iodide
LUMO	Lowest un-occupied molecular orbital
M	Induced magnetisation
Mtoe	Mega tonne of oil equivalent
<i>n</i>	LC director
n_e/n_{\parallel}	Extraordinary refractive index (perpendicular)
n_o/n_{\perp}	Ordinary refractive index (parallel)
NLC	Nematic liquid crystal
OECD	Organisation for economic co-operation and development
OFET	Organic field effect transistor
OLED	Organic light emitting diode
OSC	Organic solar cell
PCE, η	Power conversion efficiency
POM	Polarising Optical Microscopy
PDLC	Polymer dispersed liquid crystal

PEO	Polyethylene oxide
PI	Polyimide
PIPS	Polymerisation-induced phase separation
POM	Polarising optical microscopy
Pt	Platinum
PVA	Polyvinyl alcohol
PVDF-HFP	Poly(vinylidene fluoride-co-hexafluoropropylene)
R_D	Resistance of the charge diffusion
RM 257	4-(3-Acryloyloxypropyloxy)-benzoic acid 2-methyl-1, 4-phenylester; 2-Methylbenzene-1,4-diyl bis{4-[3-(acryloyloxy)propoxy]benzoate}
R_{Pt}	Charge transfer at the platinum electrode
R_s	Sheet resistance of the TCO
R_{sh}	Shunt resistance
R_t/R_{TiO_2}	Charge transfer resistance at the TiO_2 /electrolyte interface
S	Order parameter
SEM	Scanning electron microscopy
SiO_2	Silicon dioxide
SIPS	Solvent-induced phase separation
SmA	Smectic A liquid crystal
Sm-PE	Smectic-templated polymer electrolyte
Spiro-OMeTAD	2, 2', 7, 7'-Tetrakis[N, N-di(4-methoxyphenyl)amino]-9, 9'-spirobifluorene
TBAI	Tetrabutylammonium iodide

TBP	4-tert-butylpyridine
TCO	Transparent conductive oxide
T_g	Glass transition temperature
TiO ₂	Titanium (IV) oxide
TIPS	Thermally-induced phase separation
TTIP	Titanium isopropoxide
UV	Ultra-violet
UV-vis	Ultra-violet visible
V_{DS}	Voltage at drain source
V_{GS}	Voltage at gate source
V_{oc}	Open-circuit voltage
VTF	Vogel-Tamman-Fulcher
V_{th}	Threshold voltage
WF	Work function
ZnO	Zinc oxide
ZT	Thermoelectric figure of merit
$\epsilon_{\parallel}/\epsilon_{\perp}$	Dielectric constant parallel/perpendicular
$\Delta\epsilon$	Dielectric anisotropy
Δn	Birefringence
Γ	Optical retardance
λ	Wavelength
$\sigma_{\perp}/\sigma_{\parallel}$	Conductivity perpendicular/parallel
ϵ_0	Permittivity of vacuum

List of Publications

Journal articles included in this thesis

M. A. Kamarudin, A. A. Khan, M. M. Qasim, T. D. Wilkinson, "Integration of liquid crystal-polymer composite electrolyte in graphene-based dye-sensitised solar cells." *Soft Matter* (In preparation).

M. A. Kamarudin, A. A. Khan, S. M. Said, E. Tan, M. M. Qasim, T. D. Wilkinson, "Induced alignment of reactive mesogen polymer electrolyte for dye-sensitized solar cells." *RSC Advances*, 2017, 7, 51, 31989-31996.

M. A. Kamarudin, A. A. Khan, S.M. Said, M. M. Qasim, T. D. Wilkinson, "Composite liquid crystal-polymer electrolytes in dye-sensitised solar cells: effects of mesophase alkyl chain length." *Liquid Crystals*, 2017, 1-10.

M. A. Kamarudin, A. A. Khan, C. Williams, G. Rughoobur, S. M. Said, S. Nosheen, A. J. Flewitt, M. M. Qasim, T. D. Wilkinson, "Self-assembled nanostructure through templating of Smectic:Nematic binary liquid crystal mixture for dye-sensitized solar cells." *Electrochimica Acta*, 2016, 222, 657-667.

M. A. Kamarudin, A. A. Khan, M. M. Qasim, T. D. Wilkinson, "Effect of dielectric permittivity on the performance of polymer dispersed-liquid crystal electrolyte dye-sensitized solar cell." *Proceedings of SPIE*, 2016, 9940, 994010-994019.

Journal articles published during PhD which are not related to this thesis

A. Khan, M. A. Kamarudin, M. M. Qasim, T. D. Wilkinson, "Formation of physical-gel redox electrolytes through self-assembly of discotic liquid crystals: Applications in dye-sensitized solar cells." *Electrochimica Acta*, 2017, 244, 162-171.

A. A. Khan, G. Rogubor, M. A. Kamarudin, Alessandro Seppe, James A. Dolan, Andrew J. Flewitt, M. M. Qasim, T. D. Wilkinson, "Homologous binary mixtures and improved hole conduction of self-assembled discotic liquid crystals." *Organic Electronics*, 2016, 36, 35-44.

A. A. Khan, M. A. Kamarudin, P. R. Kidambi, S. Hofmann, T. D. Wilkinson, "Graphene and chiral nematic liquid crystals: a focus on lasing." *RSC Advances*, 2015, 5, 57437-57443.

Conferences

M. A. Kamarudin, A. A. Khan, M. M. Qasim, T. D. Wilkinson, “Effect of dielectric permittivity on the performance of polymer dispersed liquid crystal (PDLC) electrolyte dye-sensitized solar cell (DSSC)” SPIE Optics + Photonics 2016, San Diego, United States, 2016.

A. A. Khan, M. A. Kamarudin, M. M. Qasim, T. D. Wilkinson, “Discotic liquid crystalline hole transport layers: towards capillary filled organic-inorganic photovoltaic devices” 2016 MRS Spring Meeting and Exhibit, Arizona, United States, 2016.

A. A. Khan, G. Rughoobur, M. A. Kamarudin, A. Sepe, J. A. Dolan, A. J. Flewitt, M. M. Qasim, T. D. Wilkinson, “Developing hole transport layers using doped triphenylene discotic liquid crystals” Joint Conference of the British & German Liquid Crystal Societies, Edinburgh, United Kingdom, 2016.

M. A. Kamarudin, A. A. Khan, S. Nosheen, M. M. Qasim, T. D. Wilkinson, “Liquid Crystal as a Template for Efficient Polymer Electrolyte Dye-sensitized Solar Cells”, 2015 Asia-Pacific Solar Research Conference, Brisbane, Australia, 2015.

M. A. Kamarudin, A. A. Khan, M. M. Qasim, T. D. Wilkinson, “Polymer dispersed liquid crystal (PDLC) as next generation gel polymer electrolyte for dye-sensitized solar cells (DSSCs)”, International Conference on Hybrid and Organic Photovoltaics 2015, Rome, Italy, 2015.

A. A. Khan, M. A. Kamarudin, M. M. Qasim, T. D. Wilkinson, “Discotic Liquid Crystal Dye Sensitized Solar Cells (DLC-DSSC)”, International Conference on Hybrid and Organic Photovoltaics 2015, Rome, Italy, 2015.

Chapter 1 Introduction

1.1 Background

Liquid crystal (LC) materials exhibit physical properties that are between those of solids and liquids under certain conditions, that is, temperature variation and solvent concentration. In addition, different molecular compositions lead to the formation of different phases, such as nematic, smectic and columnar phases (Chandrasekhar 1992). These characteristics are due to intermolecular interactions and molecular geometry (cylinder or disc-like) that tends to self-assemble in a given direction and sometimes in positional order. The nematic phase is the simplest LC phase and shows thread-like defects when observed under a cross polarised microscope. The thread-like discontinuities form what is called a Schlieren texture, where two or four dark brushes meet. The molecules tend to assemble, with the long axes pointing toward a certain direction. Unlike the nematic phase, the smectic phase are typically more viscous due to the increased order that is closer to a solid, as smectic phases not only have orientational order but also a positional order: the molecules also tend to align in layers.

Thermotropic (i.e. temperature dependent LCs) can be formed by rod-shaped (calamitic), or disc-shaped (discotic) molecules, and bulk phases typically exhibit dielectric and optical anisotropy because properties along and perpendicular to the molecular longitudinal axis are significantly different (Chandrasekhar 1992). Even for homologous LC materials, the mesophase morphology, phase transition temperature and physical properties are different due to strong dependence on the molecular structure. Small variations, such as changing the length of the alkyl chain, can have a significant effect on mesophase properties. LC materials are made up of a rigid core structure that gives an elongated shape, alkyl chains that introduce flexibility to the molecule and end groups that are often responsible for the anisotropic behaviour. Alkyl chain length often affects the melting point of the material and thus the nematic phase stability. Increasing the alkyl chain length of a molecular template that exhibits a nematic phase tends to encourage smectic phase formation (Singh and Dunmur 2002).

Due to the presence of a polar group, LC molecules can be oriented by applying an electric or magnetic field (Blinov and Chigrinov 1994). The morphology of LCs can also be controlled using a thin surface treatment or alignment layer (Geary et al. 1987). A thin layer of polymer that is baked and then rubbed in one direction is employed, and the LC molecules

usually align in the grooves produced by the rubbing action. Self-assembly in the bulk LC phase is achieved naturally, either due to hydrogen bonding or π - π stacking of the molecules (Kato 2002; Pouzet et al. 2009). This characteristic allows researchers to manipulate this material and use it in a wide range of applications including displays, lasers and, solar cells (Coles and Morris 2010; Ding and Yang 2012; Uchida 2014; Zheng et al. 2011).

The incorporation of LCs in polymeric materials produces liquid crystal/polymer composites (LCPCs) or polymer dispersed liquid crystals (PDLCs), as proposed by Fergason in 1973 (Fergason 1973). PDLCs are prepared by dispersing LCs in the form of nano/microdroplets in a polymer medium. These droplets contain directionally oriented nematic or smectic LCs. The self-assembly of LCs within this polymer matrix allows tunability of their birefringence as a function of an applied electric field. The LC molecules still retain their unique electro-optical properties. These properties are governed by the LC and polymer components. More specifically, the chemical structure of the LCs, and in turn the mesophase and anchoring characteristics of the polymer interface determine the properties and application of the PDLCs. Despite their unique properties, typical applications of PDLCs are limited to optoelectronic applications, such as switchable windows and displays; this is because only their birefringence is exploited for applications (Cupelli et al. 2009; Doane et al. 1988). An interesting direction PDLCs could take relates to the exploitation of their electrical properties for electronic devices, which have largely gone unexplored to date. In recent years, there have been attempts to integrate PDLCs in dye-sensitised solar cells (DSSCs), which has substantially improved the efficiency of DSSCs (Högberg et al. 2014; Karim et al. 2010).

DSSCs were first demonstrated in 1991 by O'Regan and Grätzel (O'Regan and Grätzel 1991). These hybrid organic-inorganic solar cells have the advantage of being environmentally friendly whilst allowing easy and low-cost fabrication without sacrificing their relatively high efficiency compared to organic solar cells. One of the major components of DSSCs is the electrolyte, which is a redox mediator responsible for the regeneration of the dye and the electrolyte itself. The electrolytes in DSSC devices can be of three different types-liquid electrolytes, gel polymer electrolytes or solid-state electrolytes. Liquid electrolyte DSSCs give the highest efficiency of up to 13 % for a cobalt-based electrolyte (Mathew et al. 2014). However, this type of electrolyte suffers from evaporation of the solvent, which reduces its long-term stability. To address this issue, researchers have proposed solid electrolytes that are more stable but that sacrifice efficiency of the device because they exhibit

low ionic conductivity. It has been found that by employing various additives and plasticisers, gel polymer electrolytes provide a compromise between solid and liquid electrolytes, and thus making it possible to extend the lifetime of the device without having to sacrifice efficiency (Bella et al. 2014; Jovanovski et al. 2005; Stathatos et al. 2004; Stergiopoulos et al. 2011). One example is the addition of LC materials to the electrolyte matrix (Ahn et al. 2012; Koh et al. 2013).

In organic electronics, controlling the morphology and structure of the organic compounds is essential to realise high-efficiency devices, such as organic field effect transistors and organic solar cells (Park et al. 2007). The idea in controlling the morphology is to improve the interfacial area between electron donors and acceptors for efficient exciton dissociations in the case of organic solar cells. Some of the methods employed to control the morphology and molecular packing include thermal and; solvent annealing and; the choice of solvents and additives (Chen et al. 2014; Liao et al. 2013; Shi et al. 2015; Yi et al. 2014). The use of an electric field, E , to control the morphology of organic thin films has been demonstrated by Ma *et al.*, who applied E during solvent evaporation (Ma et al. 2012). Regarding LCs, their intrinsic ability to self-assemble provides a promising pathway for templating and enhancing the electronic charge transfer in polymer electrolytes containing LCs, which will be the main premise of this thesis.

1.2 Outline

In this thesis, the potential of LCs in an electrolyte redox couple is investigated. The development of liquid crystal-polymer composite electrolytes (LC-PEs) and LC-templated polymer electrolytes is explored using direct examples of applications in DSSCs.

An introduction to LC materials is given in Chapter 2, including an explanation of the key differences between various LC phases. The properties that make LCs unique, such as birefringence, dielectric anisotropy, conductivity and charge transfer, are described in detail. These properties originate from the structure of the molecule itself, which has a long and short axis. Examples of existing and possible applications of LCs are given at the end of the section. The following section discusses typical DSSCs, the different components and, where applicable, the challenges associated with the materials/components.

Chapter 3 explains the development of new polymer electrolytes based on LC materials. It also discusses the fabrication methods and characterisation techniques used to evaluate the properties of polymer electrolytes and the final device structure.

Since the first development of DSSCs in early 1990s, different groups have introduced various methods of fabricating them. In Chapter 4, the fabrication methods are described. This involves the study of different electrolyte materials, titanium dioxide (TiO_2) compact layers, spacers/sealants and the effect of dye-immersion time. At the end of the chapter, a summary about the final working device is given.

Chapter 5 focuses on the development of LC-PEs. In the first section, the effect of doping polymer electrolytes with nematic LCs is explored. The optimised concentration is then applied to LC materials having the same core but different alkyl chain lengths, as these materials have different LC phases and hence different properties. The effect of different dielectric anisotropies is also examined. Morphological and thermal characterisations of these materials are performed using polarising optical microscopy (POM) and differential scanning calorimetry (DSC). The addition of LC materials to polymer electrolytes affects the ionic conduction mechanism and thus the efficiency of the resulting DSSCs.

The smectic phases are known to possess higher order parameters than nematic phases and the application of LC materials as synthetic templates has been explored in various studies. In Chapter 6, a method of developing a highly ordered polymer network through the templating of a smectic A LC is explored. Because LC materials react to external stimuli such as electric field and alignment layers, the effect on the morphology is also investigated. The differences between these three polymer structures are compared based on their morphology/structure, electrical properties and photovoltaic parameters.

In LC materials, the choice of electrodes and alignment layers might affect the orientation of the molecules that can be exploited to give preferential orientation according to device applications. Gr electrodes have been shown to improve the performance of DSSCs. The interaction between Gr and LCs has been explored in numerous studies and LCs have shown some alignment effects on Gr. In Chapter 7, we first study the effect of alignment of LC materials on graphene. Next, different Gr-based counter electrodes in DSSCs are compared. The integration of LC-PEs with Gr-based DSSCs are explored in the next section in this chapter.

Finally, in Chapter 8, the conclusions and future works are presented. Further work is proposed with the hope of improving the ionic conductivity and thus the performance of DSSCs. We also suggest new device applications using LC materials.

Chapter 2 Literature review and theory

2.1 Foreword

The concept of LCs is presented in this chapter, including descriptions of the main LC phases, such as the nematic LC (NLC) and smectic LC phases. The key difference between these phases is that, in addition to orientational ordering, such as in the NLC phase, the smectic A (SmA) phase also possesses positional ordering. For each of the phases, the optical and electro-optic responses such as birefringence and, dielectric and conductivity anisotropy, are explained. These properties arise from the inherent anisotropy of the LC molecules themselves. The formation and properties of PDLCs; which is the basis for Chapter 4, are also described. Some examples of the application of LC materials are also presented in this chapter.

LC materials were first discovered in 1888 by Friedrich Reinitzer, who was working with cholesteryl benzoate at the time (Reinitzer 1888). He found that LC material exhibits two different melting points; the first from crystalline solid to cloudy liquid and the second from cloudy liquid to clear solution. With the help of Otto Lehmann, Reinitzer succeeded in observing the LC phase using a microscope under a polarised light with the aid of a hotstage. This discovery led to the birth of a new field that explores the physics and chemistry of LC materials.

What makes LCs interesting is that they have unique properties possessing an additional phase on top of the well observed crystalline solid and liquid. This mesophase, is an intermediate phase between the solid and liquid phases. LCs have the ability to flow like a liquid while still maintaining some degree of crystalline order. They can be divided into two major groups- hermotropic and lyotropic.

2.2 Liquid crystals

2.2.1 Lyotropic liquid crystals

Lyotropic LCs are materials that show mesophases depending on the concentration of solvent, which can be a water or organic solvent. These materials are classified as amphiphilic molecules made up of polar 'head' group (hydrophilic) and a non-polar 'tail' (hydrophobic)

group. In a polar solvent such as water, the hydrophobic tail group tends to assemble away from the water molecules, whereas the hydrophilic head group is in contact with water, forming micelles. An example of this can be found in soapy water. Figure 2.1 shows the formation of micelles in water. In a non-polar solvent such as hexane, the system behaves differently. Now the hydrophobic tail group is in contact with the solvent and the hydrophilic head group assembles toward the inside. Phospholipids are another example of lyotropic LCs, which is why lyotropic LCs are usually found in living organisms. However, lyotropic LCs are not covered in this study.

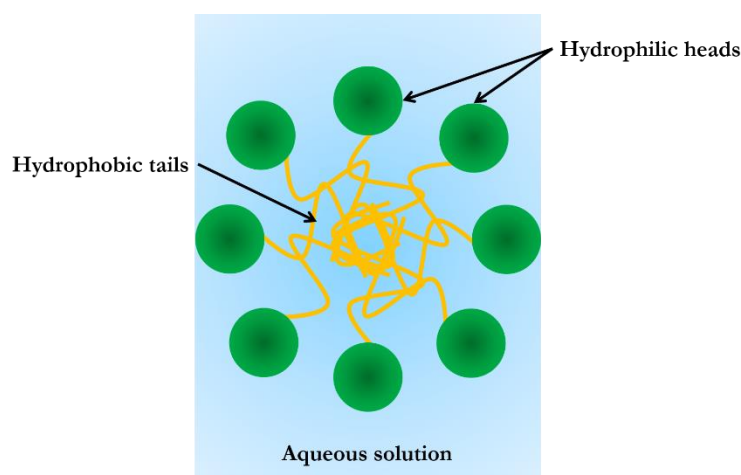


Figure 2.1 Schematic diagram of micelle formation in water.

2.2.2 Thermotropic liquid crystals

Thermotropic LCs are soft matter that show different mesophases depending on the temperature. These materials are stable in a given temperature range. Thermotropic LCs can be divided into three different groups depending on the structure of the molecules are calamitic (rod-like), discotic (disc-like) and sanidic (board-like). The structure is composed of a rigid core and, a flexible alkyl or alkoxy chain with or without a polar terminal group. Examples of the polar terminal group are CN, F, NCS and NO₂. The cores of the molecules are usually made up of aromatic hydrocarbons, although there are also LCs based on alicyclic compounds. Finally, the alkyl or alkoxy flexible chain determines the melting point of the LC molecules and stabilises alignment in the LC phase.

Calamitic LCs have different phases- nematic and smectic. The nematic phase exhibits long-range orientational order but not positional order. The smectic phase is characterised by both positional and orientational order. The nematic phase can be achieved with a short flexible

chain, and the smectic phase can be achieved with a long chain. Figure 2.2 shows a schematic diagram of calamitic LCs as thermotropic materials.

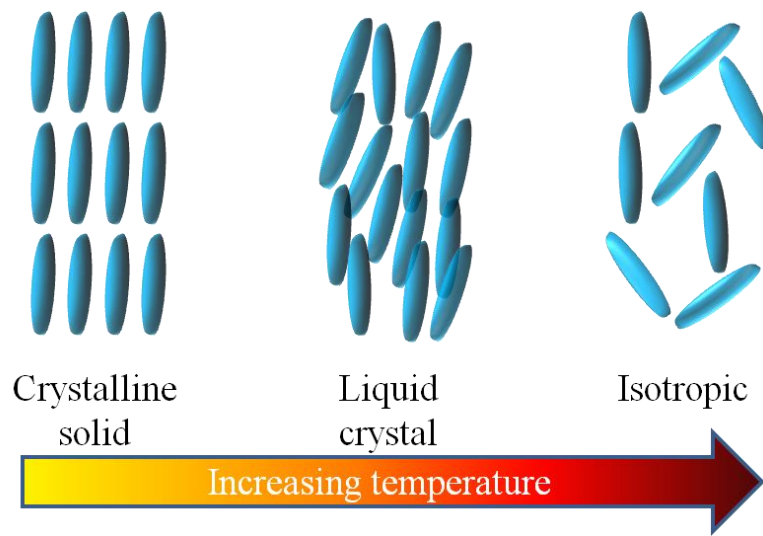


Figure 2.2 Schematic diagram of thermotropic LCs as a function of temperature.

2.2.2.1 The nematic phase

The nematic phase is the lowest ordered of the LC phases. It is named after the Greek word *nema*, meaning thread, due to the thread-like discontinuities when observed under a cross polarised microscope. The thread-like discontinuities form what is called the Schlieren texture with point defects and extinction. The presence of Schlieren texture where two or four dark brushes meet, is due to the discontinuity of the director orientation. The molecules tend to assemble with their long axes pointing toward a certain direction. The direction of these molecules is called the director, \mathbf{n} , which is the average direction of all molecules. The orientational order of LCs can be calculated from the order parameter, S , given by the following equation (Equation 2.1):

$$S = \frac{1}{2} \langle 3 \cos^2 \theta - 1 \rangle \quad (2.1)$$

where θ is the angle between the long axis of individual molecules and their direction. The bracketed part denotes the statistical average of all molecules. For a typical LC, the value of S is in the range of $0.4 < S < 0.6$: $S = 0$ for the isotropic phase and $S = 1$ for a crystal of a perfectly ordered system. Figure 2.3 shows the nematic phase and a typical nematic texture seen under crossed polarisers. The regions with the dark brushes are where the incident light

is parallel or perpendicular to the director. The defects are situated at the centre of the brushes.

The nematic phase is manifested in molecules possessing two or more rigid aromatic cores, a linking group and a terminal group. The aromatic core provides the elongated shape, the linking group introduces flexibility and controls the LC phase range and the terminal group often introduces anisotropy in its physical properties.

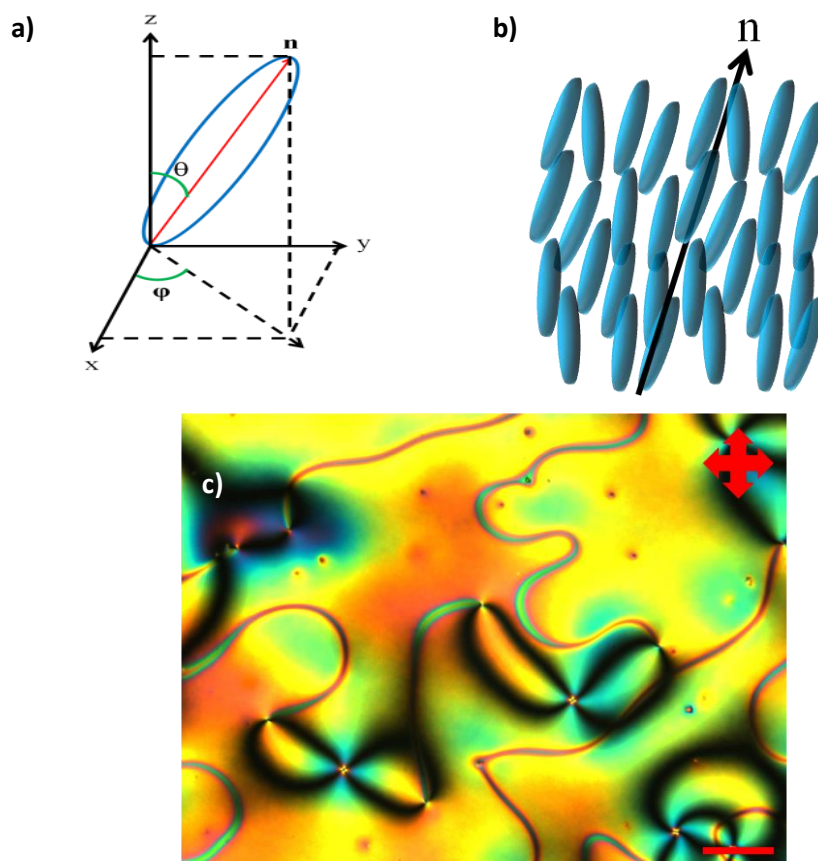


Figure 2.3 a) Schematic diagram of a single LC molecule showing the director. b) Schematic representation of a nematic phase showing the average director. c) POM of E7 LC under crossed polarisers at 20X magnification at 58 °C in a 20 μm ITO-ITO glass cell. The scale bar is 100 μm .

2.2.2.2 The smectic phase

The smectic phase is also seen in thermotropic LCs. The word smectic derives from the Greek word meaning soap. Unlike the nematic phase, the smectic phase shows both orientational and positional order. The molecules tend to align themselves in layers, as shown in Figure 2.4a, making the smectic phase more ordered than the nematic phase. An interesting characteristic of smectic LCs is that they show polymorphism, meaning that several types of smectic phase exist, such as A, B, C, and F. In this thesis, only SmA is introduced.

SmA is the simplest form of the smectic phase. In SmA, the director is aligned parallel to the normal axis. In other words, the director is perpendicular to the smectic layers. The SmA shows a typical focal conic fan texture when observed under crossed polarisers (Figure 2.4 b). Incident light polarised parallel or orthogonal to the director will result in a dark image.

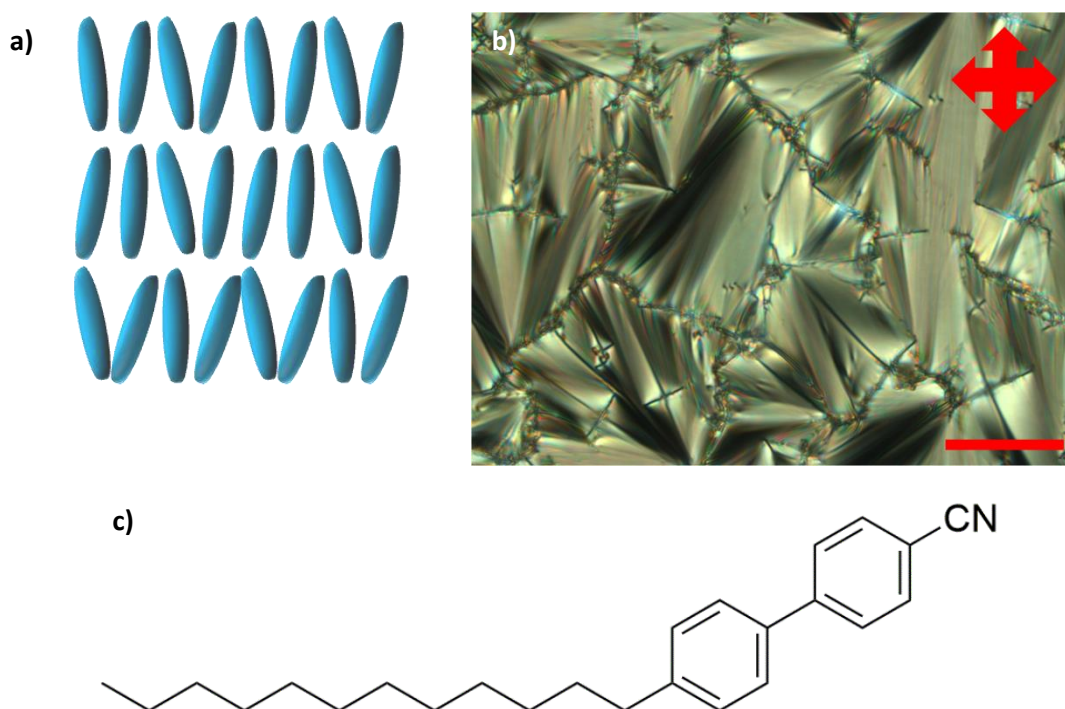
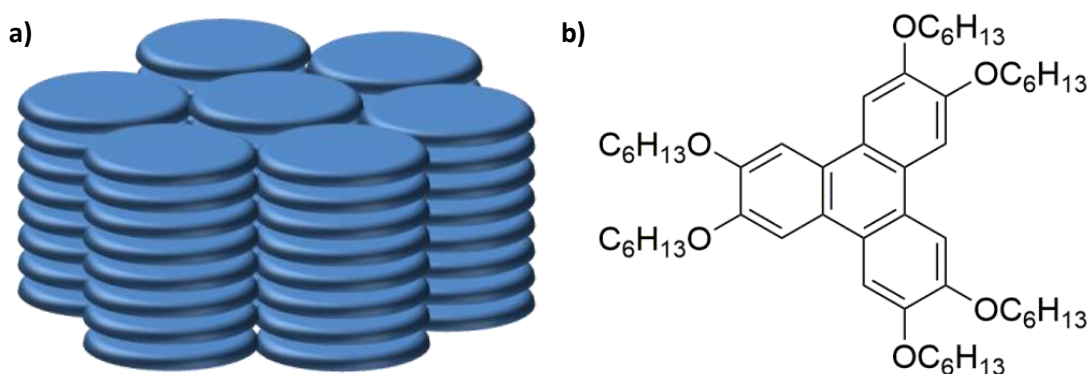


Figure 2.4 a) Schematic representation of the SmA phase. b) POM image of 12CB SmA LC phase observed under crossed polarisers at 50 °C. c) Chemical structure of 12CB. The scale bar is 50 μm .

Typically, the SmA phase is obtained with molecules having non-polar aromatic cores with two alkyl side chains or even with one alkyl chain provided that the alkyl chain is long enough to give separation. This separation allows the SmA phase to form a lamellar structure, which is due to chemical compatibility. This segregation is driven by molecules showing amphiphilic behaviour, such as in the case of organosiloxane and hydrocarbon. Figure 2.4c shows the chemical structure of 4-n-dodecyl-4'-cyanobiphenyl (12CB) which shows a SmA phase.

2.2.2.3 Discotic liquid crystals

Discotic LCs (DLCs) are another class of thermotropic LCs. The name comes from the shape of the molecules that show a disc-like structure and that tend to stack on top of each other to form columns (Pal et al. 2013; Sergeyev, Pisula, and Geerts 2007). There are two main phases possible for DLCs, the columnar and nematic phases. In the columnar phase, the molecules stack on top of each other, forming 2D arrays. The stacking of DLCs into a columnar structure is due to steric packing and π - π interactions. Like nematic LCs, DLCs are the least ordered where the director is orthogonal to the plane of the molecule. Typical DLC structure consists of benzene or polyaromatic compounds such as triphenylene or phthalocyanine. Figure 2.5 shows a) a schematic diagram of the columnar discotic phase, b) the chemical structure of 2,3,6,7,10,11-hexakis(hexyloxy)triphenylene (HAT6) and c) a POM image of HAT6.



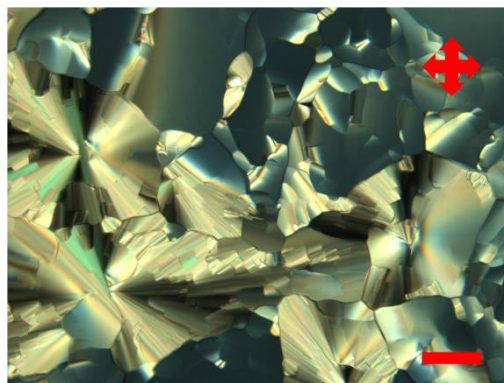
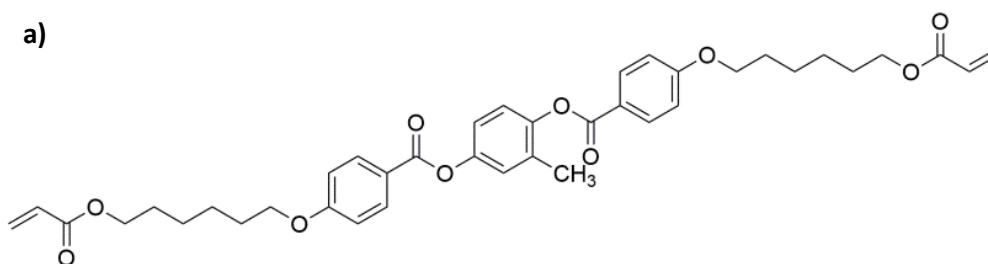


Figure 2.5 a) Schematic diagram of a columnar DLC where the molecules stack on top of each other. b) Chemical structure of HAT6. c) POM image of HAT6 in the LC phase that has been capillary-filled in a 20 μm ITO-ITO cell. The scale bar is 50 μm .

2.2.3 Reactive mesogens

Reactive mesogens, also known as LC monomers, are molecules that are very similar to calamitic LC molecules in general structure, but possess reactive end groups at one or both ends of the molecules. The reactive end groups can undergo a crosslinking reaction to form a polymer network whilst maintaining the mesophase structure. Some examples of polymerisable reactive groups are acrylate, methacrylate, diene and oxetane groups. Typical applications of reactive mesogens include 3D displays and autostereoscopic and anti-reflection films for organic light emitting diodes (OLEDs) (Aldred et al. 2005; Oh and Escuti 2007; Wu et al. 2008). The fact that reactive mesogens can be applied on any kind of surface, including rigid and flexible surfaces, makes it an interesting material. Figure 2.6 shows the chemical structure of some reactive mesogen materials.



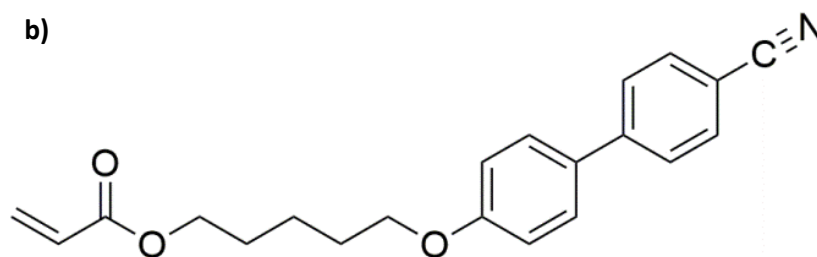


Figure 2.6 Chemical structure of some reactive mesogens. a) RM 82 and b) RM 21.

2.2.4 Polymer dispersed liquid crystals

Another interesting application of LCs is in PDLCs. PDLCs were first introduced in the late 1970s as a new class of material that showed promise in display applications (Bouteiller and Barny 1996). PDLCs combine polymer chemistry and LCs and they are formed by making an emulsion of LCs and polymer. The unique properties of PDLCs are due to the presence of small droplets of LCs in the polymer which can be controlled by an electrical or magnetic field.

PDLCs are typically fabricated using an encapsulation or a phase separation method (Serbutoviez et al. 1996). In an encapsulation method, LCs are dispersed in water soluble polymers such as polyvinyl alcohol. The water is then evaporated at a fixed rate, resulting in the LCs being surrounded by a polymer host. The disadvantages of this method are that the droplets are not uniform in size and that they tend to interconnect to form bigger droplets. The phase separation method can be divided into three types: polymerisation-induced phase separation (PIPS), thermally-induced phase separation (TIPS) and solvent-induced phase separation (SIPS). In the PIPS method, the LCs are mixed together with monomer and throughout the polymerisation process the LC is encapsulated within the polymer. The polymerisation process is usually done in the presence of ultra violet light. Droplet size is determined by two factors- the curing time and the ratio of the materials used. The TIPS method involves cooling a homogenous mixture of LCs and melted polymer at a fixed rate. The LC droplets will continue to grow until the temperature reaches the glass transition temperature of the polymer. Droplet size is mainly affected by the cooling rate; a fast cooling rate will result in small droplets. In the SIPS method, the LCs and the polymer are dissolved in a common solvent, which is evaporated at a fixed rate. Droplet size is greatly affected by the evaporation rate of the solvent. However, the evaporation rate is difficult to control and

therefore the same results are not reproducible. Figure 2.7 shows a schematic representation of the light scattering profile of PDLCs before and after applying E .

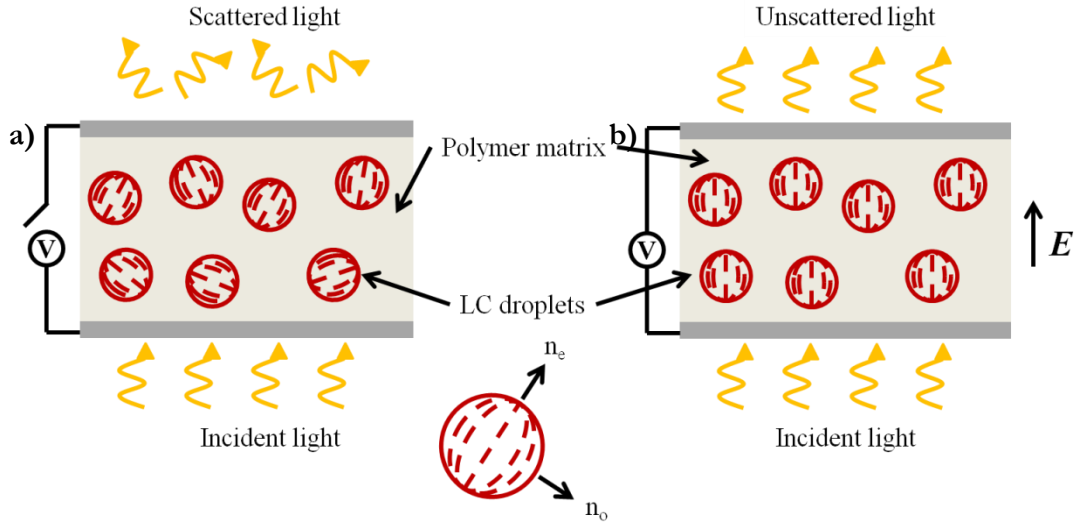


Figure 2.7 Schematic diagram of PDLC device a) before applying E and b) after applying E .

2.2.5 Properties of liquid crystals

2.2.5.1 Dielectric anisotropies

For non-polar molecules under an applied electric field, the internal charges are polarised. This involves induced polarisation comprised of two components- electronic and ionic polarisation. In polar molecules, such as in the case of LC materials, in addition to induced polarisation there is also orientational polarisation. This is due to the polarisation of dipoles by the electric field.

The dielectric anisotropy, $\Delta\epsilon$, of the LCs is given by the following equation (Equation 2.2):

$$\Delta\epsilon = \epsilon_{\parallel} - \epsilon_{\perp} \quad (2.2)$$

where ϵ_{\parallel} and ϵ_{\perp} are the dielectric constants measured parallel and perpendicular, respectively, to the long molecular axis of the LCs. $\Delta\epsilon$ depends on molecular properties such as polarisability, the dipole angle and the macroscopic orientational order. These factors also determine the sign of $\Delta\epsilon$, which can either be positive or negative. In addition, the magnitude of $\Delta\epsilon$ is highly dependent on the strength of the dipole, the frequency of the applied electric field and the temperature. As the LC material becomes isotropic, the $\Delta\epsilon$ decreases because the system is becoming less ordered. Figure 2.8 shows the dielectric permittivity of nematic LC material as a function of temperature.

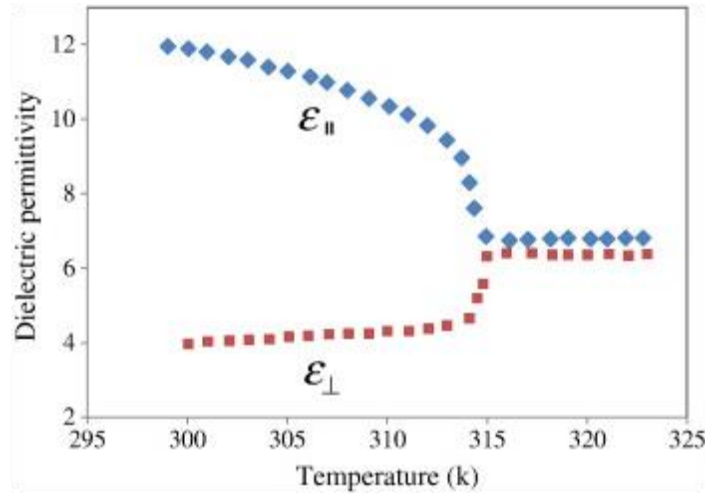


Figure 2.8 Dielectric permittivity as a function of the temperature of nematic W-1680 LC material (Zakerhamidi, Ara, and Maleki 2013).

2.2.5.2 Birefringence

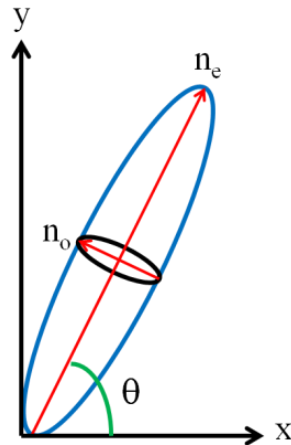


Figure 2.9 Schematic diagram of an LC molecule showing the different refractive index according to the axis.

LC materials exhibit different refractive indices along the long and short axes of the molecules due to the shape, composition and orientational order of the molecules. Light polarised perpendicular to the director of the molecule experiences a refractive index called the ordinary refractive index, n_o , whereas light polarised parallel to the director is called the extraordinary refractive index, n_e . The birefringence of uniaxial material is given by $\Delta n = n_e - n_o = n_{||} - n_{\perp}$.

The refractive index of the LC material is given by the following equation (Equation 2.3):

$$n(\theta) = \frac{n_e n_o}{\sqrt{n_e^2 \sin^2 \theta + n_o^2 \cos^2 \theta}} \quad (2.3)$$

where θ is the angle between the x -axis and the molecule and the light is travelling in the y direction and is polarised in the x direction. A schematic diagram of the optical anisotropy of LC material (known as an optical indicatrix) is shown in Figure 2.9. The birefringence is also dependent on the wavelength of the incident light and temperature. This unique characteristic of LC materials allows the material to be observed under a polarising optical microscope because the incident light has been polarised.

Using the refractive index, the optical retardance, Γ , of an LC in a cell with thickness, d and an illuminated light of wavelength, λ , can be calculated as follows (Equation 2.4):

$$\Gamma = \frac{2\pi d(n(\theta) - n_o)}{\lambda} \quad (2.4)$$

The phase shift occurs because some of the illuminated light experiences a different refractive index (either ordinary or extraordinary), which results in different velocities through the material.

2.2.5.3 Diamagnetic anisotropy

In addition to electric fields, LC materials are also sensitive to magnetic fields that cause their realignment. Under an applied magnetic field, LC molecules tend to align parallel to the magnetic field to decrease distortion in the magnetic field. This magnetic effect is mainly caused by the benzene ring which has the lowest energy configuration parallel to the magnetic field, as shown in Figure 2.10.

The susceptibility of a material to be aligned by the magnetic field is given by the following equation (Equation 2.5):

$$\mathbf{M} = \chi_{\perp} \mathbf{H} + (\chi_{\parallel} - \chi_{\perp})(\mathbf{H} \cdot \mathbf{n})\mathbf{n} \quad (2.5)$$

where \mathbf{M} is the induced magnetisation, \mathbf{H} is the magnetic field strength and \mathbf{n} is the director of the LC. In LC materials, the diamagnetic properties are different along the long and short axes of the molecules. There are two magnetic susceptibility components (parallel and

perpendicular to the director) that give rise to the diamagnetic anisotropy, defined as $\Delta\chi = (\chi_{\parallel} - \chi_{\perp})$. In most cases, nematic LCs show positive diamagnetic anisotropy and therefore will align parallel to the magnetic field.

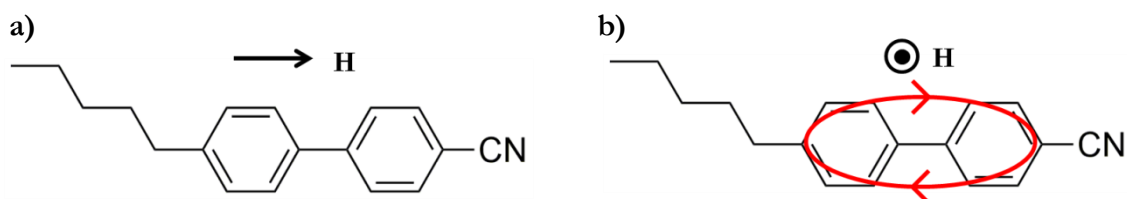


Figure 2.10 Schematic diagram showing the effect of \mathbf{H} a) parallel to a 5CB molecule and b) perpendicular to a 5CB molecule.

2.2.5.4 Conductivity anisotropy

LC materials are usually known as insulating dielectrics. However, due to impurities in the material during synthesis, they show ionic conduction with conductivities in the range of $10^{-8} - 10^{-12} \Omega^{-1} \text{ cm}^{-1}$ (Blinov 1983). Charge injection from the cell electrodes might cause ions to migrate from the substrates into the material and render it conductive. There are also semiconducting LC materials that show electronic conduction instead of ionic conduction (Woon et al. 2006). However, these are beyond the scope of this thesis.

Conductive LC materials also show anisotropic behaviour. It has been shown that the conductivity parallel to the director, σ_{\parallel} , is larger than the conductivity perpendicular to the director, σ_{\perp} . This can be attributed to the ionic mobility which is greater along the director, μ_{\parallel} , rather than perpendicular to it, μ_{\perp} . This is particularly relevant for DLCs, where the stacking of the DLC molecules results in a charge transfer along the core due to the π orbital delocalisation. Charge hopping is only possible along the molecular columns (Boden, Bushby, and Clements 1994).

2.2.5.5 Fluid viscosity

Viscosity is defined as the internal friction of a fluid to deform under a shear stress present due to velocity gradients in the system. For LC material that is confined in a cell of a few microns thick, measuring the force required to move one substrate while the other is held anchored at a constant speed will give the shear bulk viscosity. The viscosity is defined by the ratio of the shear stress to the shear strain; shear stress is defined as the force F_x per unit across the sectional area, and shear strain is defined as the velocity v_x divided by the thickness

of the cell. When the thickness becomes small enough, the effect of surface-induced ordering becomes increasingly important. The shear stress is dependent on the direction of the flow field and the configuration of the flow gradient both relative to the director field. This was shown by Miesowicz who found that LCs have three viscosity coefficients (Miesowicz 1946).

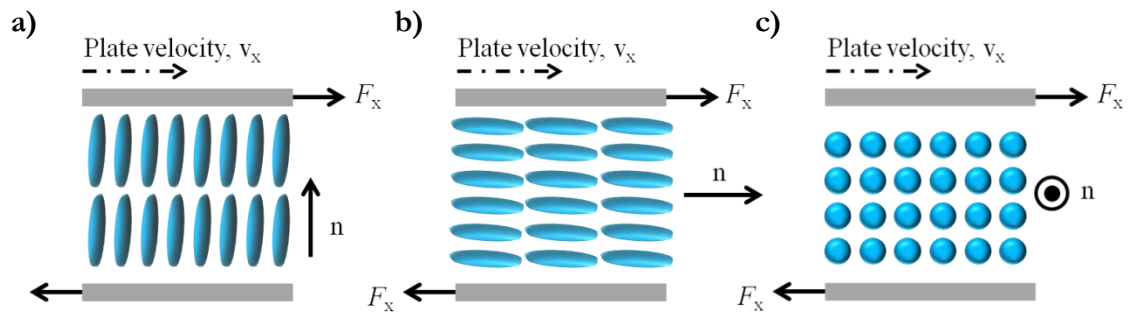


Figure 2.11 Schematic diagram of the measurement to determine the shear viscosity of a nematic LC where a force of F_x with a constant velocity of v_x is exerted on the top plate while the bottom plate is static. The director is a) homeotropic and parallel to the z-axis, b) planar and parallel to the x-axis, and c) planar and parallel to the y-axis.

2.2.5.6 Alignment layers

In LC cells, there are mainly two types of alignment that can be used to align the LC molecules either parallel or perpendicular to the substrates, which are better known as homogenous (planar), homeotropic orientation respectively or angles in between (pretilt). This is achieved by depositing a layer of polymer (alignment layer) on the glass substrates; the consequent alignment of the LCs is a result of the surface anchoring of the LC molecules with the alignment layer. A different alignment layer will result in different contact angles. This is very important for an electro-optic device where using an alignment layer can eliminate the defects and disinclination lines. Although the alignment layer is only applied to the surface of the substrates, its effect can propagate throughout the bulk material. Figure 2.12 shows the two different types of alignment layers.

In the case of the homeotropic alignment layer, typically a layer of amphiphilic molecules such as lecithin is coated on the surface of the substrate where the polar end of the molecule will attach to the surface, leaving the long alkyl chain standing up (Hiltrop, Hasse, and Stegemeyer 1994). When the LC molecules are filled into the cell, they tend to align parallel to these alkyl chains.

For planar (homogenous) alignment in a cell, a polyimide (PI) is used (Wu et al. 1996). This type of alignment is induced by rubbing the PI in one direction to create microgrooves, and the LC molecules tend to lie along these microgrooves.

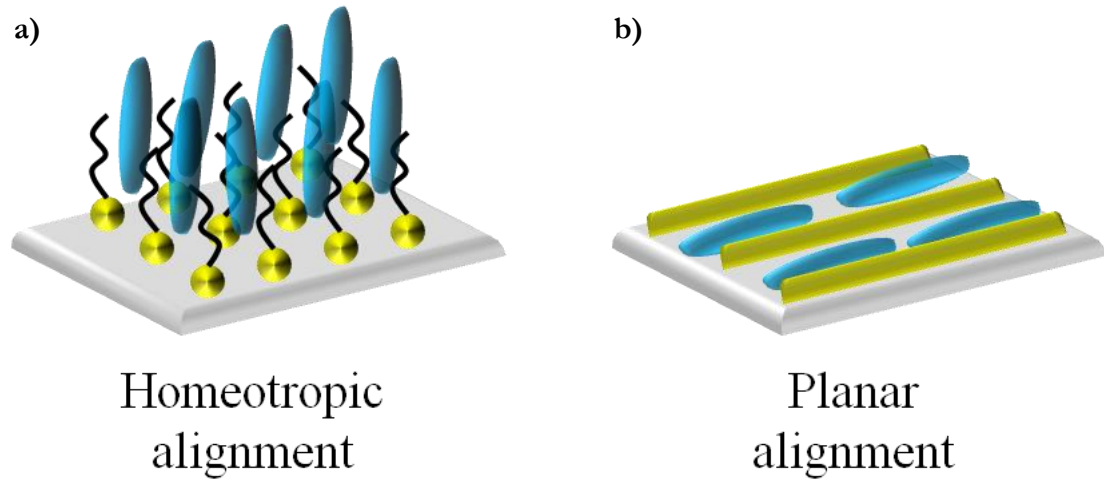


Figure 2.12 Schematic diagram of the a) homeotropic and b) planar alignment of LC molecules.

2.2.5.7 Elastic constants

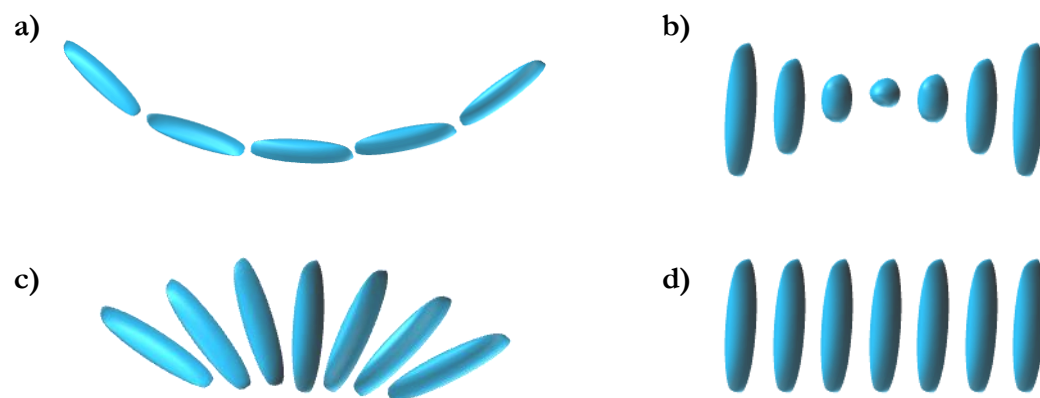


Figure 2.13 Schematic diagram of the various deformation modes in LC materials. a) bend, b) twist, c) splay and d) normal.

LC molecules are most stable in nematic LCs without an applied electric field because the free energy is at a minimum. Applying an electric field to the LCs will distort the molecules and removing it will allow the molecules to relax back to their original state. Apart from electric fields, magnetic fields, shear stresses and boundary conditions can also contribute to the distortion of LCs, as noted previously. The relaxation of the molecules comes with an elastic restoring force and an energy cost relative to the director. There are three main

distortions that can happen in LCs-splay, twist and bend (Frank 1958). The free energy of the system can be expressed using the following equation (Equation 2.6):

$$F = \frac{1}{2} [K_{11}(\nabla \cdot \mathbf{n})^2 + K_{22}(\mathbf{n} \cdot \nabla \times \mathbf{n})^2 + K_{33}(\mathbf{n} \times \nabla \mathbf{n})^2] \quad (2.6)$$

where F is the free energy densit; K_{11} , K_{22} and K_{33} are the splay, twist and bend elastic constants, respectively and \mathbf{n} is the LC director, defined earlier in the chapter. This equation indicates that all deformations of the LC orientation can be described in terms of its splay, bend and twist deformations as illustrated, in Figure 2.12.

The reorientation of the LCs from the homogenous aligned state to a deformed state under an applied field is known as the Fréedericksz transition, which is a first-order transition upon the application of voltage (Fréedericksz and Zolina 1933). As noted above, the alignment of LCs differs depending on the dielectric anisotropy and the alignment layer of the electrodes. In the case of positive dielectric anisotropy LCs, a voltage above its threshold voltage, V_{th} , must be applied to switch the molecules from planar alignment to homeotropic orientation. V_{th} is given by the following equation (Equation 2.7):

$$V_{th} = \pi \sqrt{\frac{K_{11}}{\varepsilon_0 \Delta \varepsilon}} \quad (2.7)$$

where ε_0 is the vacuum permittivity, and $\Delta \varepsilon$ is the dielectric anisotropy of the LC.

2.2.3 Applications of liquid crystals

2.2.3.1 Template for material syntheses

Templating is an important technique to impart the shapes or structures to materials that are normally difficult to achieve. The templating technique allows synthesised materials to possess similar morphologies and properties as the template up to nano-size dimensions (Dutt, Siril, and Remita 2017; Karanikolos et al. 2005). Due to their highly ordered nature, LCs have been used as templates for the synthesis of organic and inorganic materials (Oliver and Ozin 1998; Parent et al. 2012). The first report on the use of LCs as templates was by Shirakawa *et al.*, who succeeded in producing a film with highly aligned fibrils (Shirakawa et al. 1988). LCs were used as an ordered matrix solvent, assuming the alignment was under an applied magnetic field. This method has also been proven to increase the carrier mobility and

electrical conductivity of the template material (Kang et al. 2004; Watanabe, Suda, and Akagi 2013).

2.2.3.2 Organic light emitting diodes

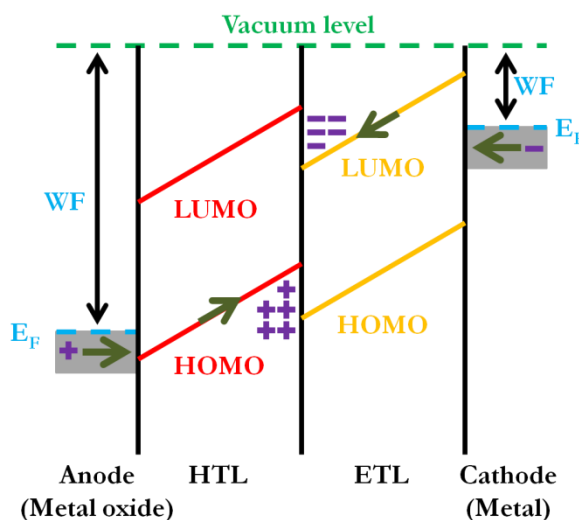


Figure 2.14 Energy level diagram of a bilayer OLED. WF is the work function of the electrodes, E_F is the Fermi level energy, HTL is the hole transporting material and ETL is the electron transporting material also known as the emissive layer.

The operating principle of the OLEDs is that the application of voltage causes the charge carriers (holes and electrons) to be injected into the organic semiconductor from the cathode and anode (Thejo Kalyani and Dhoble 2012). The holes in the HTL and the electrons in the ETL move in opposite directions until they recombine into excitons due to electrostatic forces. The recombination reaction occurs near the emissive layer, resulting in the emission of light in the frequency of the visible region. The wavelength of the light emission can be tuned by controlling the highest occupied molecular orbital (HOMO) and lowest unoccupied molecular orbital (LUMO) energy gap of the emissive layer. Figure 2.14 shows a schematic energy level diagram of an OLED. The attractiveness of OLEDs lies in the fact that they are thinner, lighter and more flexible than their crystalline counterparts. Furthermore, OLEDs are brighter and consume less energy because they do not require backlighting. It has also been shown that LCs can exhibit electroluminescence (Contoret et al. 2001). This opens up the possibility of using LCs in OLED applications. The application of LCs in OLEDs requires the materials to be semiconducting. Therefore, there have been efforts to synthesise LC materials with semiconducting properties (Aldred et al. 2004; Zhang et al. 2007). To

control the HOMO and the LUMO, the chemical structure can be tuned by changing the mesogenic core, spacer, side chain and end group.

2.2.3.3 Organic field effect transistors

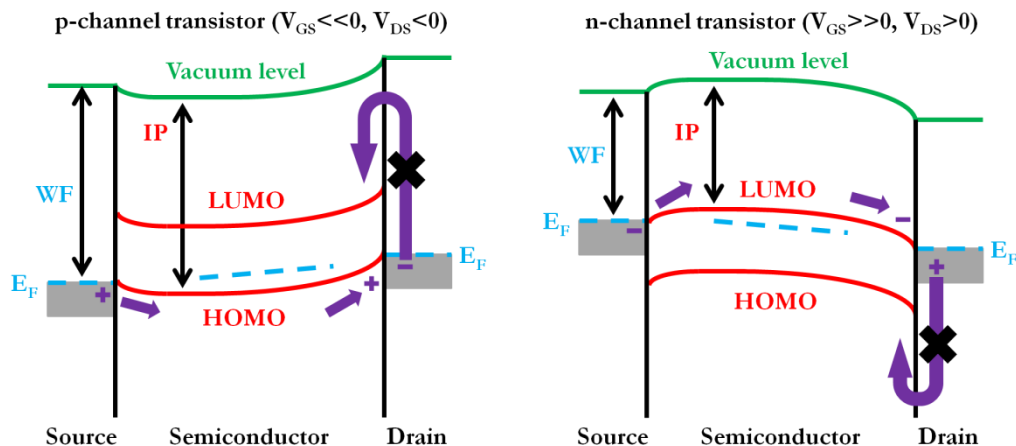


Figure 2.15 Schematic diagram of a a) p-type and b) n-type OFET. IP is the ionisation potential of the material.

Organic field effect transistors (OFETs) are electronic devices that control the flow of charge carriers using an electric field based on organic materials where the charges flow in-plane between two electrodes (Horowitz 1998). Figure 2.15 shows the energy level diagram for a) a p-type and b) an n-type OFET. In a p-type OFET, which is the more common, a negative voltage is applied causing the holes to be accumulated near the semiconductor-dielectric interface. This accumulation of holes forms a conduction route between the source and drain which allows the current to flow. When applying a positive bias, the holes are removed from the semiconductor-dielectric interface, which means the device is in the 'off' state. The threshold voltage is defined as the gate bias during which the transistor switches between the low current depletion region and the high current accumulation region. The requirement for OFETs is that the materials need to be highly ordered and possess excellent charge transport properties. With this in mind, the self-assembly characteristic and anisotropic behaviour make LCs promising candidates (Funahashi 2009). In addition, LCs have been shown to have high carrier mobilities. Discotic and smectic LCs alone have charge carrier mobility values of $0.4\text{--}0.1\text{ cm}^2\text{ V}^{-1}\text{ s}^{-1}$, which is considerably higher than that of amorphous materials (less than $10^{-3}\text{ cm}^2\text{ V}^{-1}\text{ s}^{-1}$) (Bushby and Lozman 2002; Funahashi and Hanna 2000).

2.2.3.4 Liquid crystal lasers

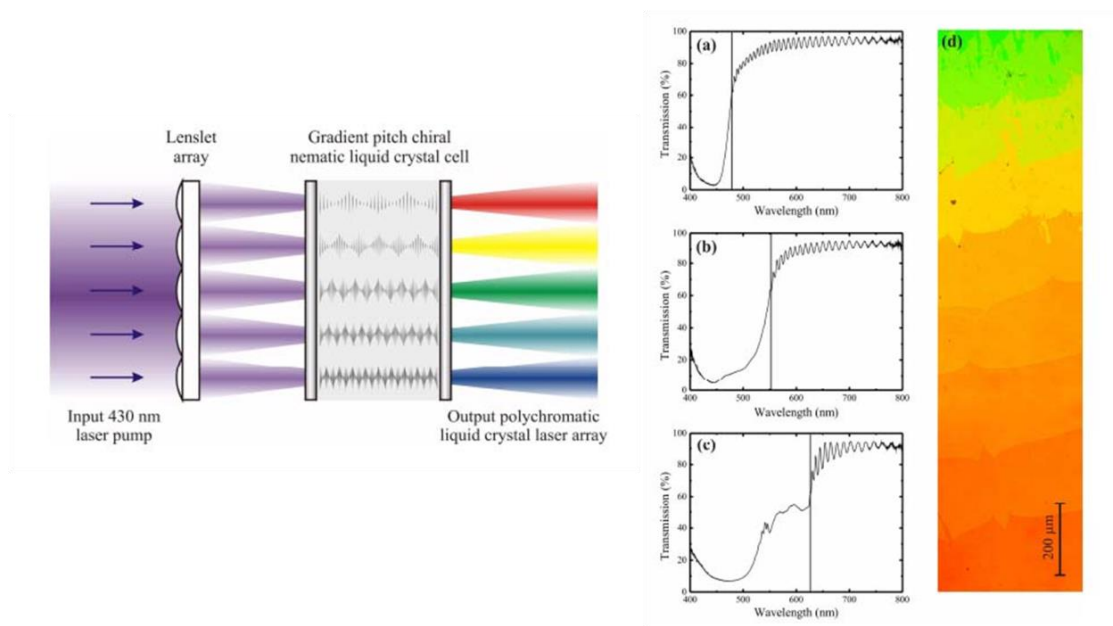


Figure 2.16 a) Schematic diagram of a polychromatic LC laser and b) transmission spectra of different colours within the same cell (Morris et al. 2008).

Compared to the well-established solid-state lasers, LC lasers are still in their infancy. The first example of LC lasers was shown by Kopp *et al.* and Taheri *et al.* using band edge lasing in dye-doped nematic LCs (Kopp et al. 1998; Taheri et al. 2001). In both cases, the fabrication of LC lasers involved the mixing of chiral nematic LCs with a laser dye. When the mixture is optically excited by a pump source, the dye will fluoresce and emit light. The chirality gives rise to the photonic band edge that can be tuned to give different colours by controlling the degree of chirality. Figure 2.16 shows a schematic diagram of a polychromatic LC laser and the resulting transmission spectra. Some of the advantages of LC lasers are their potential ease of tuning the emitted wavelength and they reduce the need for bulky components because the LC molecules are small and can be applied to flexible substrates. LC lasers have been adapted using various LC structures and phases including polymeric LCcholesteric elastomers and blue phases (Finkelmann et al. 2001; Ohta et al. 2004; Yokoyama et al. 2006).

2.2.3.5 Solar cells

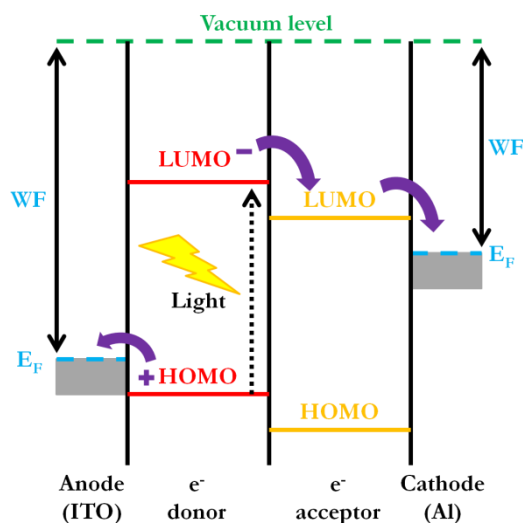


Figure 2.17 Energy level diagram of a heterojunction organic solar cell.

The first reported work on the use of LCs in a solar cell was that by Chandra *et al.* based on a heterojunction device (Chandra, Srivastava, and Khare 1986). The authors found that the addition of nematic n-(p-methoxy-benzylidene)p-butylaniline to a chlorophyll electrode enhanced the photovoltage, photocurrent and photoconductivity values. The working mechanism of heterojunction solar cells involves the use of two different organic materials (e^- donor and acceptor) with matching HOMO and LUMO. When the donor absorbs photons from the light, tightly bound electron-hole pairs are excited into the LUMO of the donor. The electron-hole pairs are subsequently separated by the internal electric field where the electrons are then moved into the e^- acceptor material via electron hopping between localised states. Finally, the charges are then extracted at the electrodes with the electrons collecting at the anode and the holes collecting at the cathode. In 1972, Kamei *et al.* showed the photovoltaic effect in a nematic LC, although the mechanism of this effect was not clear (Kamei, Katayama, and Ozawa 1972). However, the magnitude of this effect was not significant, showing an open-circuit voltage (V_{oc}) of only 0.5 V; this investigation was not followed up. In 2009, Kim *et al.* showed that LCs can be used in DSSC applications with good efficiencies of up to 6.64 %, which was attributed to the ordering of the LCs and their high optical scattering (Kim *et al.* 2009). In addition to the light scattering effect, the passivation of the TiO_2 surface by the cyano groups in LC materials has been cited for this improvement in photovoltaic parameters (Ahn *et al.* 2012; Koh *et al.* 2013). Since then, there have been similar reports investigating the effect of LCs in DSSCs (Högberg *et al.* 2014; Karim *et al.* 2010). Furthermore, due to the large LC phase range temperatures, solar cells

employing LCs can be operated at elevated temperatures while still maintaining high power conversion efficiency (Högberg et al. 2014). LCs have also been applied in bulk heterojunction organic solar cells. LC-based organic solar cells have been investigated in many studies that make full use of the self-assembly nature of LCs and their high mobility (Carrasco-Orozco et al. 2006; Sun et al. 2015).

2.3 Solar cells

2.3.1 Introduction

Every year, the world's population is increasing at a drastic rate, resulting in various problems such as a depleted food supply, health problems and, environmental problems. By 2050, it is expected the world population will reach between 8 and 10 billion (United Nations 2017). As the population increases, so do the energy demands. Currently, the world is using about 13,000 megatonnes of oil equivalent (Mtoe) per year, the main sources of which are oil and charcoal. Naturally, the burning of oil and natural gasses will release carbon dioxide into the atmosphere, making them a significant source of air pollution. To make matters worse, the oil and natural gas supplies are limited, which leads people to look for alternative energy sources. Renewable energy sources, such as wind, waves and the sun, are all promising due to their abundance and environmental friendliness. However, renewable energy currently represents only 5% of the total global energy supply. In addition, the sun, which provides the earth with thousands of exajoules of energy per year in the form of sunlight, is scarcely used. One reason for this is the lack of efficient technology to harvest the sun's vast amount of energy. Current technology that can make full use of this energy is solar cells that can convert sunlight directly into electricity. Solar cells can be divided into three categories-first generation, second generation and third generation. Figure 2.18 shows a graph of the world's energy consumption of the Organisation for Economic Co-operation and Development (OECD) countries and non-OECD countries, and Figure 2.19 shows the energy generated by various sources.

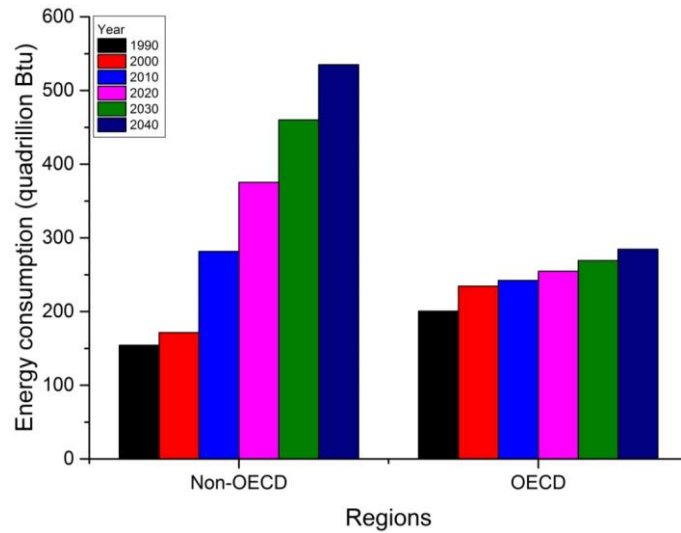


Figure 2.18 World's energy consumption according by OECD and non-OECD regions (Leahy et al. 2013).

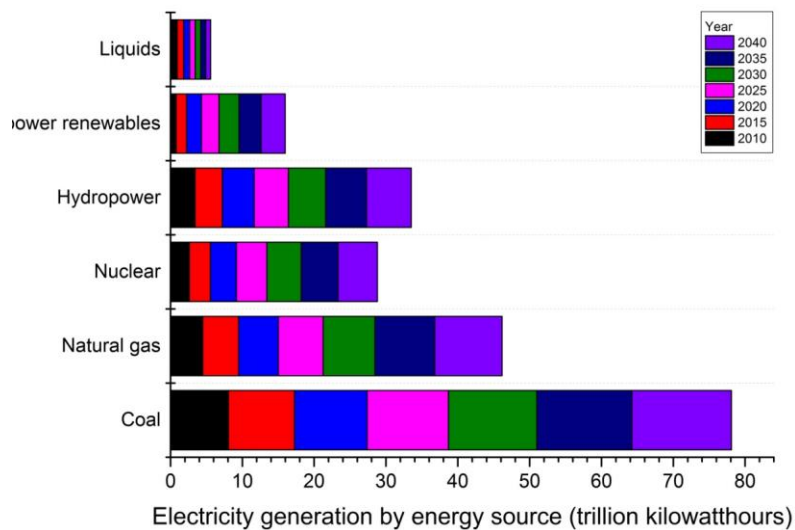


Figure 2.19 Energy generation according to different energy sources(Leahy et al. 2013).

First-generation solar cells, which are made from silicon, are the most efficient type of solar cells commercially available. This type of solar cells shows the highest efficiency of 25.6 % (Green et al. 2014). They are usually made from nanocrystalline silicon, polycrystalline silicon, amorphous silicon and hybrid silicon. Unfortunately, they are rigid and require pure silicon for the fabrication. They are also expensive to produce.

Second-generation solar cells, also known as thin-film solar cells, are usually made from non-silicon materials such as copper indium gallium selenide (CIGS) and cadmium telluride (CdTe). With average efficiencies of around 10-15%, second-generation solar cells are much lower than first-generation solar cells. However, due to their micrometre thickness, they are preferable to first-generation solar cells and provide some flexibility in terms of design. In addition, the production of this type of solar cell requires fewer materials and therefore costs less in terms of fabrication. However, the production process still involves high vacuums and temperatures. In addition, the scarcity and the toxic nature of the materials limits the mass production of this type of solar cell.

The last type of solar cell is the third-generation solar cell, based on small molecules and polymers (Greenham 2013; Liu et al. 2013). Polymer solar cells are still in their infancy, having been first introduced in early 2000. The highest efficiency to date is 11.7% (Zhao et al. 2016). Unlike inorganic and silicon solar cells, organic solar cells (OSCs) generate electricity from the dissociation of electron-hole pairs at the junction of p-type and n-type materials. Therefore, it is of the greatest importance to find materials capable of releasing and accepting electrons effectively. Some of the advantages of OSCs are that they are flexible and light-weight and easy and cheap to produce. However, despite these advantages, OSCs are still inferior to silicon solar cells in term of long-term stability and power conversion efficiency (PCE).

Another type of solar cell in this category is DSSCs, also known as hybrid organic-inorganic solar cells (Cahen, Hodes, and Gra 2000). These solar cells employ a sensitiser with the capability of exciting electrons upon light absorption attached to the surface of an oxide semiconductor. DSSCs have been widely researched since the 1990s. As of 2017, the highest efficiency ever reported for this kind of solar cell is 13 % developed by Mathem *et al.* (Mathew et al. 2014). These solar cells are very stable and easy to produce, which makes them very strong candidates to replace silicon solar cells. This thesis is concerned with this type of solar cell.

2.3.2 Introduction to DSSCs

Since the publication of the seminal paper by O'Regan and Grätzel in 1991, DSSCs have spurred a new field of research in renewable energy, as they open up the possibility of producing cheap and easy-to-manufacture solar cells (O'Regan and Grätzel 1991). Figure

2.20 shows the typical structure of a DSSC. A transparent conducting oxide (TCO) substrate is used as the photoelectrode. The photoelectrode is usually coated with a layer of mesoporous TiO_2 or other semiconductors. The surface of the mesoporous layer is attached with a sensitising dye that can absorb a broad range of wavelengths. The pores of the TiO_2 semiconductor are usually filled with an iodide (I^-)/triiodide (I_3^-) redox couple or a hole-transporting material responsible for charge transfer. Finally, a TCO substrate coated with platinum (Pt) to catalyse the redox couple regeneration is used.

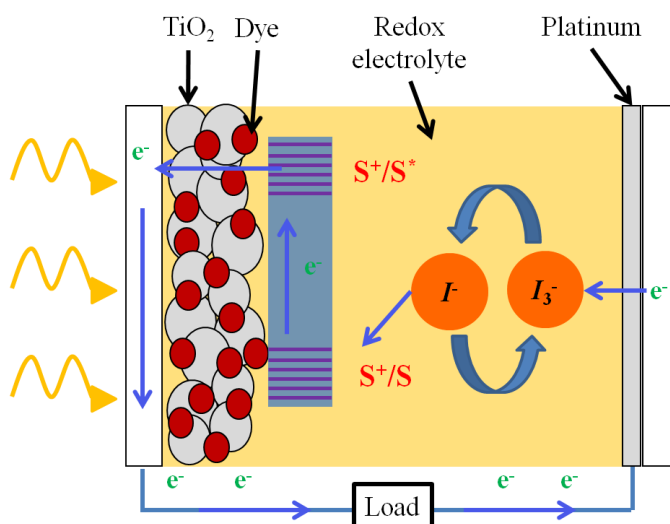


Figure 2.20 Schematic diagram of a typical DSSC (Hagfeldt et al. 2010).

2.3.3 Working principle

The operating mechanism of a DSSC is depicted in Figure 2.21. First, the sensitising dye attached to the surface of the mesoporous TiO_2 absorbs sunlight. A photon from sunlight will excite an electron from the HOMO level to the lowest LUMO level of the dye. The excited dye then transfers the electron to the conduction band of the TiO_2 semiconductor. After the injection, the electron then travels through the interconnected TiO_2 network all the way to the TCO substrate. The electron is then transferred to the counter electrode. The excitation process will leave the dye in an oxidised state. To regenerate the dye, the dye must get an electron from the redox couple that will oxidise I^- to I_3^- . I_3^- is then reduced back to I^- by accepting electrons from the counter electrode. Usually the counter electrode is coated with Pt to catalyse the regeneration of the redox couple. In an ideal system, this cycle of the reduction and oxidation process is continuous.

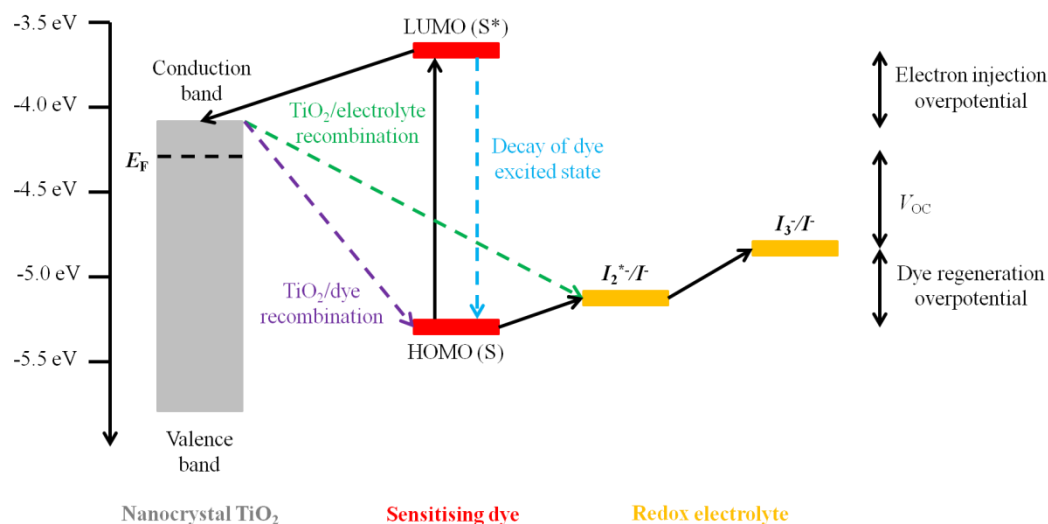


Figure 2.21 Schematic diagram showing the working principle of a working DSSC (Li and Diau 2013).

2.3.4 Electrolytes

Electrolytes are one of the major components of a DSSC (Hagfeldt et al. 2010; Wang et al. 2012). They function as charge-transfer mediators to transfer the electrons from anodes to cathodes and thus regenerate the oxidised dye. For an electrolyte to be used in a DSSC, it must show excellent chemical, thermal, optical and electrochemical stability. It should not absorb in the visible light region as this will compete with the dye absorption spectra. In addition, the electrolyte should not degrade the dye. The difference between the quasi-Fermi level of the TiO_2 and the redox potential of the electrolyte determines the maximum achievable V_{oc} of the solar cell. Therefore, a solar cell with a more positive redox potential is preferable.

i) Liquid electrolytes

Electrolytes can be divided into liquid electrolytes, solid electrolytes and quasi-solid-state electrolytes. Liquid electrolytes are the most widely used electrolytes in DSSCs. They are made by dissolving an ionic salt in an organic solvent (Yu et al. 2011). The ionic salt functions as a redox couple for the charge transfer. Currently, the I^-/I_3^- redox couple shows the best DSSC performance. Despite having a high ionic conductivity of approximately $10^{-2} \text{ S cm}^{-1}$, liquid electrolytes pose problems during the DSSC fabrication process. Due to their liquid nature, the sealing of the device is problematic, and the solvent used in the liquid electrolyte

tends to evaporate at high temperatures or over time. There is also a possibility of the liquid electrolyte leaking out of the cell. I^-/I_3^- -based liquid electrolytes have also been shown to degrade the dye. These drawbacks have limited the mass production of this type of solar device. To address these issues, several alternatives have been suggested such as replacing the volatile solvent with a non-volatile compound such as 3-methoxypropionitrile or valeronitrile. The use of ionic liquids such as imidazolium salt, has been proposed to completely remove the solvent in the system. However, due to the high viscosity, imidazolium salt has a lower ionic conductivity and ionic diffusion, which affects the solar device efficiency.

ii) Solid-state electrolytes

Liquid electrolytes are known to be unstable due to the tendency of the solvent to evaporate when exposed to air. This necessitates sealing the device completely, which means additional costs to find good sealing materials. In addition to evaporation and the sealing problem, the corrosive nature of the I^-/I_3^- electrolyte is another aspect that researchers are trying to avoid. To address the issues of short lifetime and leakage, alternative materials are being widely researched.

Solid-state-hole-transporting materials (HTMs) are promising candidates due to their better mechanical stability. In addition, the fabrication process is much simpler compared to liquid electrolytes. One of the earliest examples of a solid-state HTM is copper (I) iodide (CuI), which is a p-type inorganic semiconductors (Bandara and Yasomanee 2006; Yu et al. 2012). However, the main problem with solid HTMs/electrolytes, is the poor contact between the HTM/electrolyte and the mesoporous TiO_2 . This is also true in the case of CuI where the material is not stable due to poor interfacial contact between the CuI and TiO_2 . The formation of large CuI crystallites leads to poor pore filling and therefore low efficiency. By using triethylaminehydrothiocyanate as the crystal growth inhibitor, it is possible to increase efficiency up to 3.75 % (Kumara et al. 2002). Alternatively, solution and vapour deposition of CuI have been developed to improve the pore filling of CuI into the TiO_2 .

In 1998, Grätzel *et al.* reported the use of organic HTM, 2,2',7,7'-tetrakis(N,N'-di-p-methoxyphenylamine)-9,9'-spirobifluorene (spiro-OMeTAD) (Figure 2.22), which showed an efficiency of 0.74 % (Bach et al. 1998). Spiro-OMeTAD is a small molecule that can readily dissolve into an organic solvent. This allows the HTM to fill the voids in the mesoporous

layer. The use of spiro-OMeTAD has also been shown to increase the V_{oc} , as the redox potential is more positive than the I^-/I_3^- redox couple. Over the years, this material has been improved. Currently, the best performing device incorporating spiro-OMeTAD has an efficiency of 7.2 % (Burschka et al. 2011).

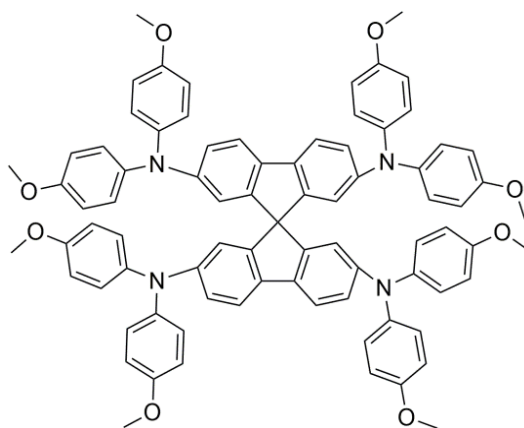


Figure 2.22 Chemical structure of 2,2',7,7'-tetrakis(N,N'-di-p-methoxyphenylamine)-9,9'-spirobifluorene (spiro-OMeTAD).

The last type of solid-state electrolyte is the solid polymer electrolyte (Matsuiro and Takaoka 1996). Made by dissolving an alkaline salt in a high molecular weight polymer host. The requirements for a good polymer host are i) good solvent for the salt, ii) the ability to dissociate the salt and iii) the capability to reduce ion pair formation. The ionic motion results from the solvation-desolvation process along the polymer chains in the amorphous phase. The most commonly used polymer is poly (ethylene oxide) due to the presence of electron donor atoms that allow the cations to migrate through a Lewis acid-base interaction. The highest efficiency ever achieved by a polyethylene oxide (PEO) polymer electrolyte is 5.23 % (Akhtar et al. 2013). The advantages of solid polymer electrolytes are that they are easy to fabricate, cheap to produce, flexible and light. However, they are still limited by their low ionic conductivity due to poor electronic contact between the electrolyte and the TiO_2 . In addition, the fact that the polymer always exists in the crystalline phase contributes to the lower ionic conductivity.

iii) Gel polymer electrolytes (GPEs)

Finally, there are the quasi-solid state electrolytes, also known as gel polymer electrolytes (GPEs) (Cao and Oskam 1995; Shibata et al. 2003). These electrolytes are somewhere between liquid electrolytes and solid electrolytes. They are made by dissolving a polymer that acts as a host in a solvent together with an inorganic salt. GPEs still maintain some degree of flowability and flexibility. The ionic conductivity of GPEs is typically between that of liquid electrolytes and solid electrolytes. They are also easy to process while maintaining this high ionic conductivity, unlike solid electrolytes. In addition, GPEs have an excellent pore filling capability vis-à-vis the porous TiO_2 layer. They also have superior thermal and long-term stability. Commonly used polymers include polyethyleneglycol (Gong, Sumathy, and Liang 2012), polyacrylonitrile (Ileperuma et al. 2011) and poly(vinylidene fluoride-hexafluoropropylene) (PVDF-HFP) (Noor et al. 2011).

The mechanism of ionic conduction within a polymer electrolyte is attributable to the intra-chain and inter-chain hopping whereby the segmental motions of the polymer chains allow the cations to move between one coordination site and another, either on one chain or between adjacent neighbouring chains. High ionic conductivity is believed to be facilitated by the inter-chain hopping. Figure 2.23a and Figure 2.23b show the motion of cation aided by polymer segmental motion. Ion clusters can also contribute to the ionic conduction through ion-ion interactions, as shown in Figure 2.23c and Figure 2.23d. However, this type of ionic conduction is limited by the concentration of ions within the polymer host.

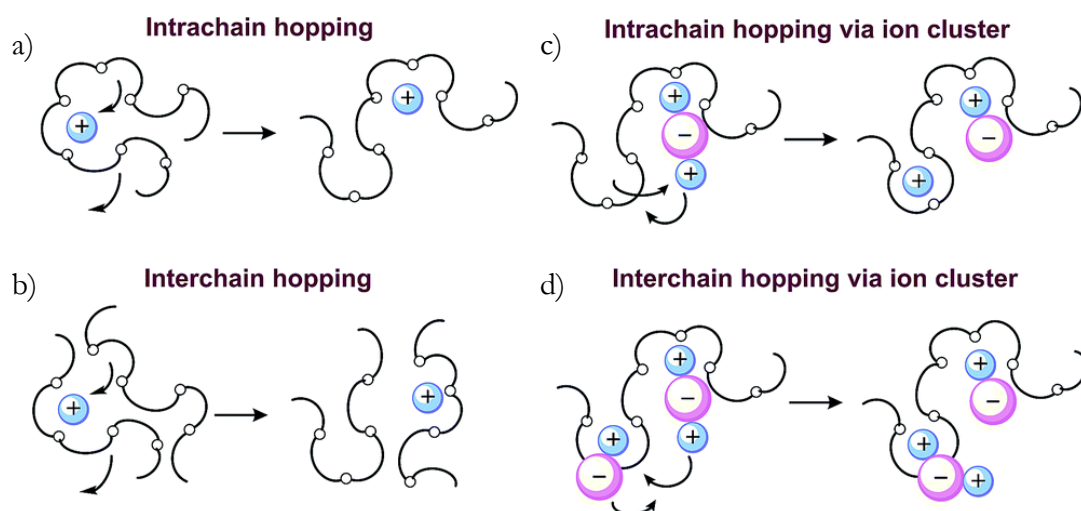


Figure 2.23 Ionic conduction mechanism of a polymer electrolyte assisted by polymer chains only and ionic cluster: a) ion hopping intra-chain and b) inter-chain; c) ion pair dissociates; d) ion pair dissociates and pairs with another unpaired ion (Xue, He, and Xie 2015).

High ionic conductivity can be achieved if the polymer host is ideally in the amorphous phase or in other words if the glass transition temperature is low enough so that at room temperature it is already in the amorphous state. High crystallinity in a polymer limits the performance of the polymer electrolyte (Stephan 2006). For example, in PEO and many PEO/salt mixtures, the crystallinity is around 70-85% at room temperature.

iv) Additives and plasticisers

For all electrolytes, especially GPEs, plasticisers are added to increase the ionic conductivity. Plasticisers have low molecular weight and high boiling points. The addition of plasticisers can increase the flowability of the polymer electrolyte. However, they can also lead to the loss of mechanical properties. The addition of plasticisers is intended to reduce the glass transition temperature and the crystallinity of the polymer to achieve a more amorphous state. Some examples of plasticisers typically used are ethylene carbonate and propylene carbonate (Subramania et al. 2013). DSSCs using this plasticiser have shown a conductivity of $1.1 \times 10^{-3} \text{ S cm}^{-1}$, V_{OC} of 0.69 V and J_{SC} of 1.7 mA cm^{-2} (Ren et al. 2001). Another example is γ -butyrolactone (GBL), which is said to help with the coordination and dissolution of ions in the polymer. The highest ionic conductivity achieved with this plasticiser is $1 \times 10^{-4} \text{ S cm}^{-1}$. The advantage of using GBL is that it not only increases the ionic conductivity but increasing the GBL content gives the polymer the characteristics of a liquid while still maintaining its mechanical properties.

Another method to improve the properties and characteristics of the electrolyte is by introducing additives. Additives such as nanoparticles of TiO_2 (Katsaros et al. 2002), SiO_2 (Zhou et al. 2009) and ZnO have been shown to increase the ionic conductivity of the GPE. Due to their large surface area, the TiO_2 nanoparticles are capable of preventing recrystallisation and thus reduce the crystallinity of the polymer. The addition of TiO_2 also enhances the dissolution of the inorganic salt. Organic molecules can also be used as an additive. Tertbutylpyridine (TBP) is always added to electrolytes as it can improve the carrier lifetime. This is done by reducing the electron recombination with the I_3^- . Boschloo *et al.* has published a paper detailing the effect of adding TBP to DSSCs (Boschloo, Häggman, and Hagfeldt 2006).

Because solid polymer electrolytes have low ionic conductivity compared to liquid electrolytes, researchers have been trying to improve the ionic conductivity by, for example, mixing polymer electrolytes with other materials, changing the parameters and revising the fabrication method. Recently, researchers have performed experiments with LCs as one of the materials to improve the performance of DSSCs (Gi-Dong 2010). It is thought that the alignment of LCs helps improve the electrical properties of solar cells.

2.3.5 Counter electrodes

Counter electrodes are responsible for collecting and transferring electrons from the external load to the electrolyte redox couple. Typically, the surface of a counter electrode is coated with a thin layer of Pt that acts as a catalyst for the oxidation of I_3^- to I^- . To date, Pt is the best material for counter electrode due to its high electrocatalytic properties and because it is stable against the corrosive nature of the I^-/I_3^- redox electrolyte. However, Pt is extremely expensive and the reserves are limited. Therefore, there is a need to replace Pt with cheaper and more abundant materials.

One alternative material is carbon. It is known that carbon is one of the most abundant materials in the earth's crust. It has also been proven that carbon is non-toxic, corrosion resistant, provides low cost of fabrication and has excellent catalytic activity in relation to the electrolyte. Many types of carbon materials are available, such as carbon black, activated carbon, carbon nanotubes, Gr and fullerene. Of these, Gr has attracted significant interest in recent years.

Gr was first extracted from graphite by Geim and Novoselov in 2004, despite the theoretical framework being put forward as early as 1947 (Raimond et al. 2004; Wallace 1947). It is an allotrope material forming a 2D structure one atom thick. Recent research has shown that Gr has a high charge carrier mobility, excellent conductivity, high transmissivity, excellent thermal conductivity and is extremely strong due to its high Young's modulus. Some of these interesting properties make it possible for Gr to be applied in DSSCs either as the photoanode or the photocathode.

2.4 Summary

In this chapter, the theory of LC materials and the related physical properties that make LC materials unique were explained. The different classes of LC materials were presented, focusing on nematic and smectic LCs because these materials are used in this thesis. In addition, we gave a brief overview of DSSCs, including the working mechanism and the different components. The challenges of each type of materials were explained in this chapter.

Chapter 3 Materials and Experimental Methods

3.1 Foreword

In this chapter, the materials, experimental apparatus and procedures designed and assembled for use in the thesis are described. The experimental setup developed and used herein is a versatile tool for examining the electro-optic and material properties of the LCs and polymer electrolytes. We are particularly interested in examining the morphology, conductivity and photovoltaic properties of these materials in detail. The chapter starts with the preparation of different LC materials, either in their pure form or in mixtures and the relevant characterisations of LC materials including thermal, electro-optical, dielectric and electrical characterisations.

3.2 Fabrication

3.2.1 LC cell fabrication

LC cells were prepared by sandwiching two indium-doped tin oxide (ITO) (Sigma Aldrich, 8-12 Ω /sq) substrates with the thickness of the cell controlled using UV curable spacer glue. The ITO substrate was cut into the desired size using a tungsten carbide pen. The substrates were placed in a polytetrafluoroethylene holder and immersed in a 4 wt% of Decon 90 cleaning solution in water. The holder was then placed in an ultra-sonic bath for 15 min to remove the contaminants from the surface of ITO substrates. The substrates were then sonicated in de-ionised water to remove residual detergent. Subsequently, the substrates were sonicated in isopropyl alcohol (IPA) (ACROS Organics, 99 %), acetone (ACROS Organics, 99 %) and IPA, with 15 min of sonication in each step. After the last step, the substrates were dried off with a nitrogen gun.

In this thesis, the effect of the alignment layer on the morphology of LCs is also explored. The alignment layer was prepared using a PI (AL-16301) solution diluted in cyclopentanone. The alignment layer solution was spin-coated on the pre-cleaned ITO substrate at a spin speed of 3000 rpm for 1 min, followed by baking at 220 °C for 30 min to evaporate the solvent. After cooling down the substrate to room temperature, the substrate was then rubbed using a rubbing machine that was built in-house. The rubbing machine consists of a rotating drum covered with a nylon cloth.

An LC cell was fabricated by putting a few droplets of spacer beads dispersed in UV-curable glue (Norland NOA68) on one substrate. The top substrate was placed on top of the first substrate and pressed gently to get a homogenous thickness. The thickness of the LC cell can be controlled using different spacer beads ranging in size from 1 μm to 42 μm . Here, we used 20 μm spacer beads. The sandwiched substrates were then placed in a UV EPROM eraser to polymerise the glue.

To confirm the thickness of the LC cell, an interference method was employed whereby the empty cell was placed under a white light. The resulting interference fringes were then detected by a spectrometer. According to Etalon theory, in the case of normal light incidence, the resulting constructive interference must satisfy the following equation (Equation 3.1):

$$2nd = m_i \lambda_i \quad (3.1)$$

where n is the refractive index in the cell ($n \approx 1$ in the case of air), d is the thickness of the cell, m_i is the number of peak in the interference spectrum and λ_i is the wavelength at which the successive peaks occur.

3.2.2 DSSC fabrication

1. Working electrode

In DSSCs, fluorine-doped tin oxide (FTO) (Sigma Aldrich, $\sim 7 \Omega/\text{sq}$) substrates are often used rather than ITO substrates. This is because FTO substrates are more thermally stable than ITO substrates. Previous studies have shown that the resistivity of FTO does not change significantly upon annealing (Sima, Grigoriu, and Antohe 2010). However, in the case of ITO substrates, the resistivity increases exponentially with increasing annealing temperatures.

Here, FTO substrates were cleaned using IPA, acetone and IPA with 15 min ultrasonication for each solvent. The substrates were then finally dried with a nitrogen gun. Next, the pre-cleaned substrates were coated with a compact layer.

The compact layer was primed by preparing two different solutions-solution A (350 μl titanium tetraisopropoxide in 2.5 ml ethanol) and solution B (35 μl 2 M HCl in 2.5 ml ethanol). The two solutions were then mixed together for 24 h using a shaker. The prepared

compact layer mixtures were then spin-coated on the pre-cleaned FTO glass substrates at 2000 r.p.m for 60 s. The spin-coated substrates were annealed using the following protocol:

100 °C for 10 min (ramping rate: 7.5 °C min⁻¹)

150 °C for 10 min (ramping rate: 7.5 °C min⁻¹)

325 °C for 30 min (ramping rate: 7.5 °C min⁻¹)

450 °C for 30 min (ramping rate: 7.5 °C min⁻¹)

The substrates were then coated with titania paste (Dyesol, 18NR-T Transparent Titania Paste) using the doctor blading method. A reinforcement ring was applied to the region coated with the compact layer. The TiO₂ paste was applied on the substrate and carefully flattened using a glass slide. Once an even thin film of the TiO₂ layer was achieved, the reinforcement ring was removed. The residual glue from the reinforcement ring and the TiO₂ was removed using a Q-tip dipped in IPA solvent. The resulting area of TiO₂ film was 0.283 cm² with a thickness of approximately 8 ± 0.3 µm. The prepared substrates were cured using the following protocol:

325 °C for 5 min (ramping rate: 7.5 °C min⁻¹)

375 °C for 5 min (ramping rate: 7.5 °C min⁻¹)

450 °C for 30 min (ramping rate: 7.5 °C min⁻¹)

The substrates were allowed to cool to 70 °C naturally and were immersed in 0.3 mM N719 dye in tert-butanol:acetonitrile (1:1 vol:vol) for 24 h. Next, the substrates were taken from the dye solution and washed with tert-butanol:acetonitrile (1:1 vol:vol) to remove the excess dye molecules that were not attached to the TiO₂.

2. Counter electrode

The counter electrodes were prepared by spin-coating Pt paste (Dyesol, PT1 Platinum Paste) onto pre-cleaned FTO substrates at 4000 r.p.m for 30 s to ensure homogenous spreading of the Pt paste. The coated substrates were then annealed using the following procedure:

325 °C for 5 min (ramping rate: 7.5 °C min⁻¹)

375 °C for 5 min (ramping rate: 7.5 °C min⁻¹)

450 °C for 30 min (ramping rate: 7.5 °C min⁻¹)

The substrates are allowed to cool to room temperature naturally.

3. Graphene counter electrode

Figure 3.1 shows the schematic diagram of the Gr transfer process. The Gr used in this work was provided by Mr. Philipp Braeuninger, a PhD student in Prof. Stephan Hofmann's group in the Department of Engineering at the University of Cambridge. The Gr was grown using the chemical vapour deposition (CVD) process. Gr on copper foil was cut into the desired size. One side of the foil was coated with polymer (4 wt. % polystyrene (Sigma Aldrich, $M_w \sim 35,000$) in toluene (Sigma Aldrich, 99.8 %)) and left to dry for 10 min. Once dry, the foil was placed in a FeCl₃ (Sigma Aldrich, 99.99 %) solution and allowed to etch for 2-4 h. During the etching process, the copper was etched from the Gr, leaving a transparent film. Once a transparent film was obtained, it was put in three water baths to remove excess copper or impurities, using glass slides. Care was taken during the transfer process from one water bath to another as the thin film is very fragile. During the last water bath, the Gr was transferred directly onto the counter electrode coated with Pt. Once transferred onto the counter electrode, the substrate was placed inside the oven at 80 °C for 30 min to remove excess water. The substrate was then placed under UV light for 30 min to degrade the polymer layer. Once the polymer was cured, the substrate was immersed in ethyl acetate (Sigma Aldrich, 99.8 %) solution to remove the polymer leaving a thin film of Gr on top.

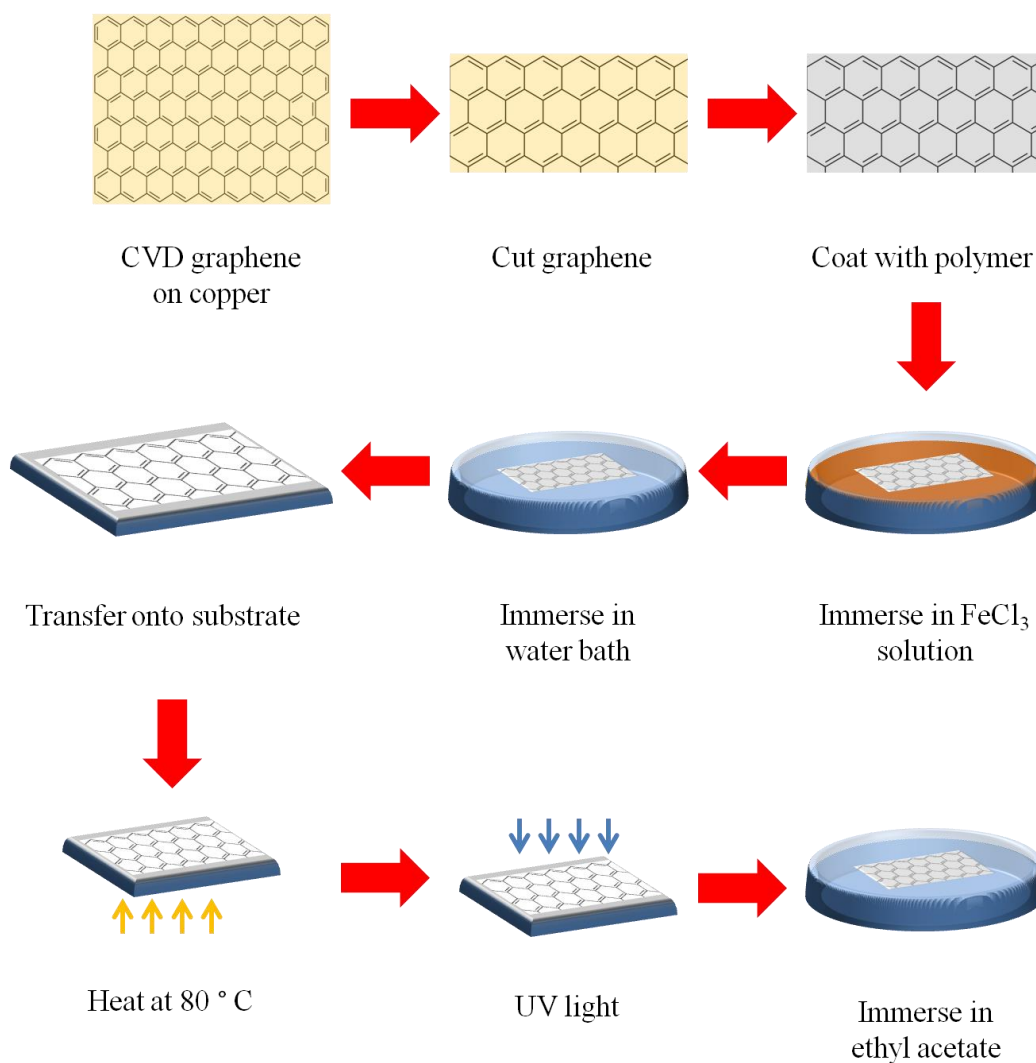


Figure 3.1 Schematic diagram of wet transfer process of Gr on a substrate.

4. Electrolyte

The liquid electrolyte consists of 0.6 M DMPH (1,2-dimethyl-3-propylimidazolium iodide, Solaronix), 0.5 M LiI (lithium iodide, Sigma Aldrich, 99.9 %), 0.05 M I_2 (iodine, Sigma Aldrich, 99.999 %) and 0.5 M TBP (4-tert-butylpyridine, Sigma Aldrich, 96 %) in acetonitrile (Sigma Aldrich, 99.8 %). The solution was stirred until all components completely dissolved. This formulation has been shown to give high efficiency DSSCs as reported by Wei *et al.* (Wei et al. 2006).

3.2.3 LC-PEs preparation

The polymer electrolyte was prepared by dissolving 10 wt% of PVDF-HFP (Sigma Aldrich, $M_w \sim 400,000$) in the liquid electrolyte at 90 °C, which was then stirred for 4 h. Different compositions (0 wt%, 5 wt%, 10 wt%, 15 wt% and 20 wt%) of 5CB (Merck) LCs were added to the polymer electrolyte and then stirred for another 3 h. The optimum concentration giving the highest solar cell efficiency was used to prepare other types of LC-PEs. The chemical structures of the LC materials used to prepare other LC-PEs are shown in Figure 3.2.

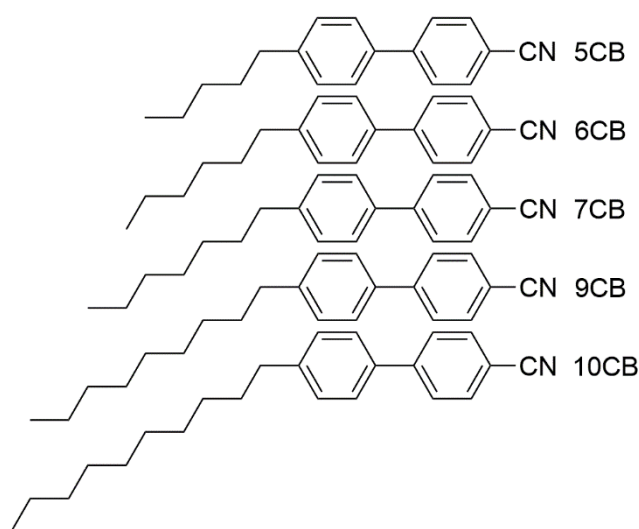


Figure 3.2 Chemical structures of the homologous cyanobiphenyl LCs used to prepare LC-PEs.

3.2.4 LC binary mixture preparation

LC mixtures of SmA (8/2 organosiloxane) and NLC (E7) (Merck) were prepared using different ratios. The binary LC mixtures were mixed together by placing them in an oven and bringing them above their isotropic temperatures for 4 h. The resulting mixtures were used for further characterisations. The structures of the materials are shown in Figure 3.3.

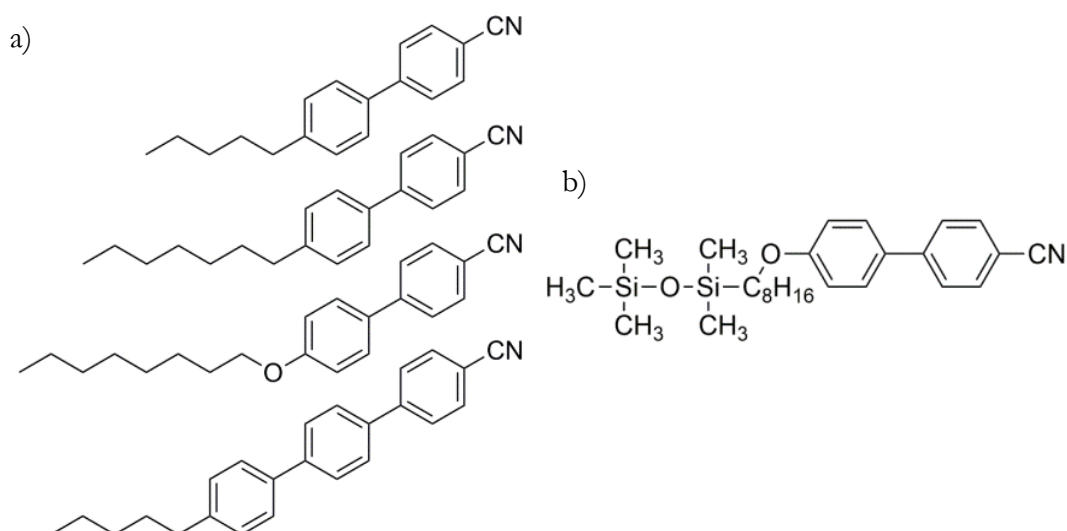


Figure 3.3 Chemical structures of a) E7 and b) 8/2 organosiloxane.

3.2.5 LC template preparation

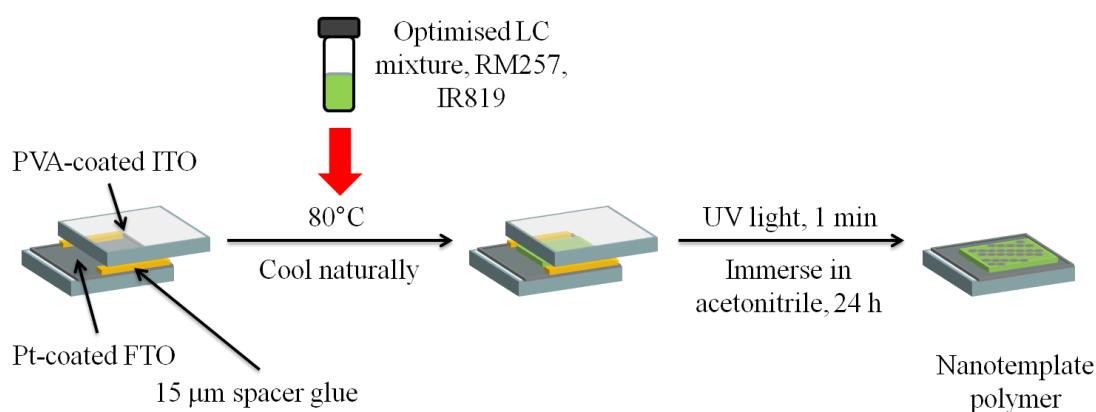


Figure 3.4 Schematic diagram of the preparation of an LC template.

Figure 3.4 shows the steps in preparing the LC template. The optimised binary LC mixture that was prepared previously was mixed with a reactive mesogen (RM 257) (Merck) and a photoinitiator (IR 819) (Merck). The mixture was heated in an oven above the isotropic temperature for 4 h. After that, the mixture was filled into a cell with a thickness of 15 μm and cured using a UV light (1 mW cm^{-2}) for 1 min. The cell was fabricated with Pt-coated FTO substrate on one side and polyvinyl alcohol (PVA)-coated glass substrate on the other side. The preparation of the Pt coated FTO substrates has been discussed previously. Figure 3.5 shows the chemical structure of the reactive mesogen and the photoinitiator.

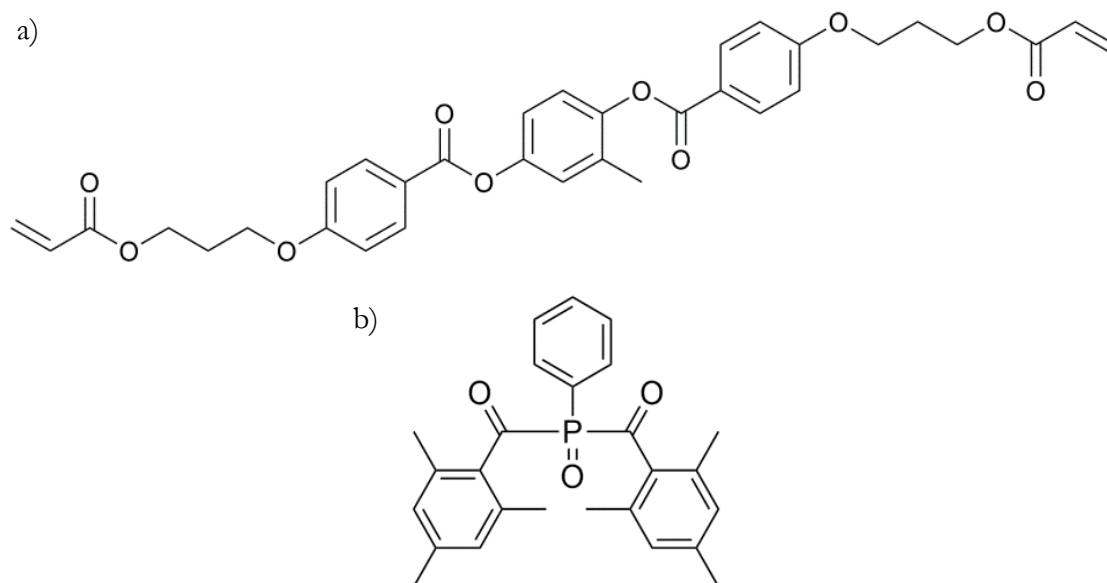


Figure 3.5 Chemical structures of a) the reactive mesogen (RM 257) and b) the photoinitiator (IR 819).

3.3 Characterisations

3.3.1 Polarising optical microscopy

As explained previously, bulk LC phases are birefringent due to their chemical structures. In investigating the different LC phases, POM is an important characterisation technique. In this experiment, an Olympus polarising optical microscope (BX60) was used. The microscope has polarisers on either side of the samples and are crossed so that no light can pass through the system and a dark view is observed through the eyepieces. Therefore, only samples that are optically anisotropic will allow light to pass through and show different colours. These two polarisers were placed beneath and above the sample stage which can be rotated. A collimated light source was irradiated from the bottom of the microscope and could be controlled by the iris diaphragm. A hot stage (THMS 600, Linkam) attached to a temperature controller (TMS 94, Linkam) was mounted on top of a rotating sample stage to allow the sample to be rotated 360° . The samples were brought to isotropic phase and slowly cooled down to their LC phase with the heating or cooling temperature was controlled at 5°C min^{-1} . Figure 3.6 shows a schematic diagram of the Olympus BX-60 polarising microscope.

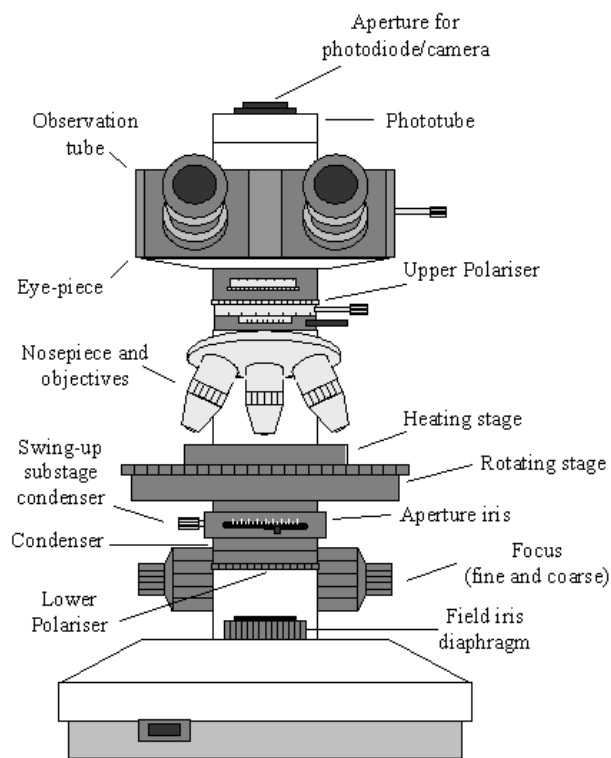


Figure 3.6 Schematic diagram of a POM.

3.3.2 Differential scanning calorimetry

Differential scanning calorimetry (DSC) is a thermal analytical method widely used in characterising materials. In LC research, DSC is an important tool to determine the transition temperature to complement POM. In DSC, a blank sample pan (reference) and a pan containing a sample are heated at the same rate, and the heat flow that keeps the temperature of both pans constant is measured. At the transition temperature, the sample will either absorb or release more energy compared to the reference while still maintaining the same temperature. Here, DSC measurements were performed using a Mettler Toledo DSC 823e. The measurements were done from 0°C to 100°C at a rate of 5°C min⁻¹. For the DSC measurement, a sample of weight 5-10 mg was placed in an aluminium sample. The transition temperatures of the LC mixtures were obtained from the DSC curve.

3.3.3 Ultraviolet-visible spectroscopy

Ultraviolet-visible (UV-vis) spectroscopy works by shining a light through a sample and measuring the absorption spectra. Different molecules with different bonding absorb light of different wavelengths. When light is absorbed by a molecule, an electron is excited from the ground state (bonding or non-bonding) to the first excited state (anti-bonding). Each

excitation requires a different amount of energy depending on how far the gap from the occupied state to the non-occupied state is. Each wavelength of light corresponds to a different energy value as can be seen from the Planck-Einstein equation (Equation 3.2) below:

$$E = \frac{hc}{\lambda} \quad (3.2)$$

where h is Planck's constant, c is the speed of light and λ is the wavelength. We can determine the type of molecule from the equation.

The absorption spectrum of the dye solution was measured in a 1 cm-wide cuvette from 350 - 700 nm. The spectrum of the solvent used to dissolve the dye was taken as the background reading which was subtracted from the spectrum of the dye solution.

3.3.4 Fourier transformed infra-red spectroscopy

Fourier transformed infra-red (FTIR) is an important tool to identify the components and composition of a material. The IR light source is first passed to the interferometer when the light signal is changed to an interferogram signal. This interferogram signal will then enter the sample upon which some of the IR light will be absorbed or transmitted and only specific frequencies of energies are absorbed by the material. The transmitted signal from the sample is then captured by a detector, which is then digitised and sent to the computer for processing. Here, the signal undergoes a Fourier transformation. In this experiment, the characterisation was performed on a silicon substrate in transmission mode from 4000 to 1400 cm^{-1} using a Frontier FT-IR/FIR spectrometer obtained from PerkinElmer. A background scan using a silicon substrate was performed to determine the percent transmittance compared with that of the sample.

3.3.5 Scanning electron microscopy

In scanning electron microscopy (SEM), a sample is bombarded with electrons and the molecules on the surface of the sample interact with these electrons depending on the acceleration voltage of the SEM. The electrons, are produced by an electron gun that is focused by condenser lenses. In this study, the ex situ characterisation of the polymer was done on a silicon wafer (SEM, Zeiss SigmaVP, 2 kV). The black and white images obtained from the micrographs are due to the difference in the electron density of the samples. For

an insulating material, the charges tend to accumulate on the surface and impede the characterisation. To reduce charge build-up on top of the sample, a thin layer of gold (10 nm<) was sputtered. This characterisation was performed with the help of Mr. Calum Williams, Mr. Girish Rughoobur and Mr. Edward Tan.

3.3.5 Atomic force microscopy

In Atomic force microscopy (AFM), a cantilever measures the force between the tip of the cantilever and the sample with a laser beam that tracks the vertical and lateral deflections of the cantilever. Here, tapping mode AFM (Model 5400 Scanning Probe Microscope, Agilent Technologies) was performed on the LC-templated samples to measure the topography and morphology. The characterisation was performed using samples prepared on Pt counter electrodes. This characterisation was performed with the help of Mr. Girish Rughoobur

3.3.6 Dielectric permittivity

Dielectric permittivity measurements were performed using a precision component analyser (Wayne-Kerr WK6440A) dielectric bridge automated using LabVIEW software. During the measurement, room temperature was maintained using a hot stage (THMS 600, Linkam) attached to a temperature controller (TMS 94, Linkam). The measurement was performed from 0 to 10 V at a voltage step of 0.1 V.

To determine the dielectric permittivity, the capacitance of the charged parallel plates of the cell must be measured. The relationship between the capacitance and the dielectric constant is given by the following equation (Equation 3.3):

$$C = \frac{\epsilon_0 \epsilon A}{d} \quad (3.3)$$

where ϵ_0 is the vacuum permittivity, ϵ is the relative permittivity of the dielectric material being measured, A is the overlap area between the top and bottom substrates and d is the thickness of the cell. The value of ϵ depends on the type of alignment (homeotropic or planar) imposed on the material. For a planar cell, the previous equation can be rewritten as Equation 3.4:

$$C_{\perp} = \frac{\epsilon_0 \epsilon_{\perp} A}{d} \quad (3.4)$$

To account for the empty cell, the capacitance of the empty cell was also measured using the following equation (Equation 3.5):

$$C_0 = \frac{\epsilon_0 A}{d} \quad (3.5)$$

From these two equations, the value of ϵ_{\perp} can now be calculated as Equation 3.6:

$$\Delta\epsilon = \epsilon_{\parallel} - \epsilon_{\perp} \quad (3.6)$$

where ϵ_{\parallel} is the dielectric permittivity measured using a homeotropic LC cell.

3.3.7 Current-voltage conductivity measurement

Current-voltage (I - V) measurements were performed using an LCR bridge component analyser (Wayne Kerr) with a bias voltage ranging from 0 - 1 V at 1 KHz. A symmetric ITO-ITO cell was used to measure the ionic conductivity of the sample where the thickness of the cell is controlled using a thermoplastic sealing film of 25 μm or 60 μm thickness. Temperature-dependent measurements were performed by placing each cell on a hot-stage and recording the ionic conductivity as a function of temperature. The temperature-dependent conductivity behaviour of most common electrolytes follows the Arrhenius relation (Çavuş and Durgun 2016) whereby a straight line can be used to plot the natural log of the rate constant (conductivity) against inverse temperature ($1/T$).

3.3.8 Linear sweep voltammetry

Linear sweep voltammetry is the most basic potential sweep voltammetry. The ionic diffusion coefficient was measured in a symmetrical Pt-Pt cell of 25 μm or 60 μm using Metrohm Autolab PGSTAT302N from 0 V to 1.5 V at a rate of 10 mV s^{-1} . At 0 V, there was no redox reaction. When positive bias was applied at the working electrode, current started to flow where I_3^- diffused to the other electrode and reduced to I^- . Increasing the applied voltage increased the current exponentially until it levelled off because the starting materials were being consumed. This is called the limiting current. In this measurement, I_3^- was the limiting material because it is bigger than I^- ; therefore, the diffusion was slower than for I^- (Zistler et al. 2006).

3.3.9 Light scattering

The light scattering effect of the LC-electrolyte samples were also investigated using a red LED diode laser (650 nm) with an elliptical beam. The sample was placed 10 cm from the laser and a beam stop was used to remove the zero-order of the output light so that the scattered light could be observed more clearly. Figure 3.7 shows the experimental setup for the light scattering experiment.

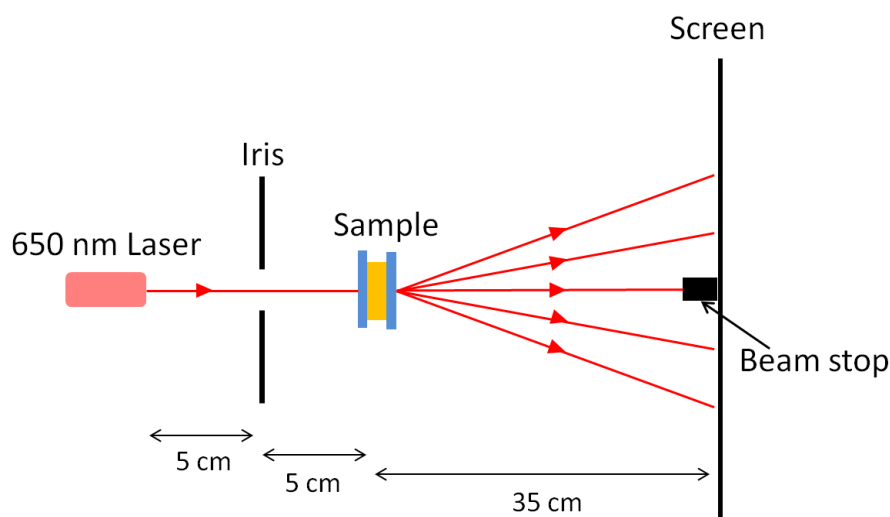


Figure 3.7 Schematic diagram of the light scattering setup.

3.3.10 Photovoltaic parameters

Each measurement was performed by irradiating the solar devices with a light source calibrated to be 100 mW cm^{-2} sunlight at AM 1.5G (1 sun) using a Xenon lamp. The calibration was performed using a silicon solar cell with a known output current at 1 sun. The intensity of the light source was set so that the current output on the silicon solar cell equal to that at 1 sun illumination. The output current was measured against the applied voltage using a Keithley 2400 SourceMeter connected to a LabVIEW program developed in-house. Figure 3.8a shows a typical $J-V$ curve for a solar cell under sunlight illumination. In the dark, a solar cell behaves like a diode, and as the light intensity is increased a current is generated. Figure 3.8b illustrates the equivalent circuit for a simple photovoltaic device. R_s is the series resistance that accounts for the internal resistance and the resistance produced at the contacts. R_s is made up of the charge-transfer resistance at the Pt counter electrode, the charge carrier transport resistance in the electrolyte and the sheet resistance of the TCO

substrates. R_{sh} is the shunt resistance that provides alternative pathways for current, effectively reducing the voltage. The R_{sh} is interpreted as the back-electron transfer, and an ideal solar cell will have a small R_s but a large R_{sh} .

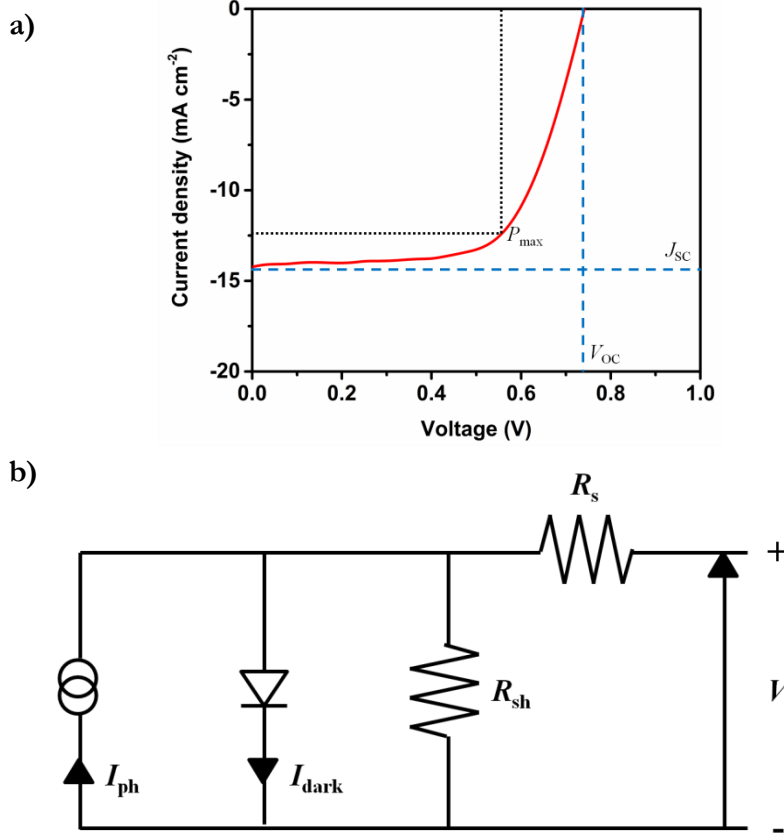


Figure 3.8 a) Typical J - V curve of a solar cell under light soaking and b) equivalent circuit for a standard solar device.

From the J - V measurement, data such as V_{oc} , J_{sc} and fill factor (FF), which are needed to calculate the efficiency (η), can be obtained. The J_{sc} is the current density at which the voltage is zero and the impedance is low. The V_{oc} value is when the device can no longer produce current. There is no current flowing between the two electrodes which is when the voltage is maximum to the external circuit. The fill factor is interpreted as the “squareness” of the J - V curve. The equation to calculate FF is as follows (Equation 3.7):

$$FF = \frac{I_{max}V_{max}}{V_{oc}J_{sc}} \quad (3.7)$$

From this data, the power conversion efficiency (η) can be calculated using the following equation (Equation 3.8):

$$\eta = \frac{V_{oc} J_{sc}^{FF}}{P_{in}} \quad (3.8)$$

3.3.11 Electrochemical impedance spectroscopy

Electrochemical impedance spectroscopy (EIS) is an important tool to investigate the underlying processes taking place in a photovoltaic device. Information such as the charge transport resistance, series resistance and shunt resistance can be obtained from this measurement. Here, the measurement was performed using a Metrohm Autolab PGSTAT302N in the frequency range of 10 mHz to 1 MHz with a 10 mV step under dark conditions. A bias voltage of -0.7 V was applied during the measurement to simulate the V_{oc} of the solar device. A typical EIS graph consists of three semicircles, each representing different processes at the electrodes and interfacial kinetics taking place. Figure 3.9 shows a typical EIS curve.

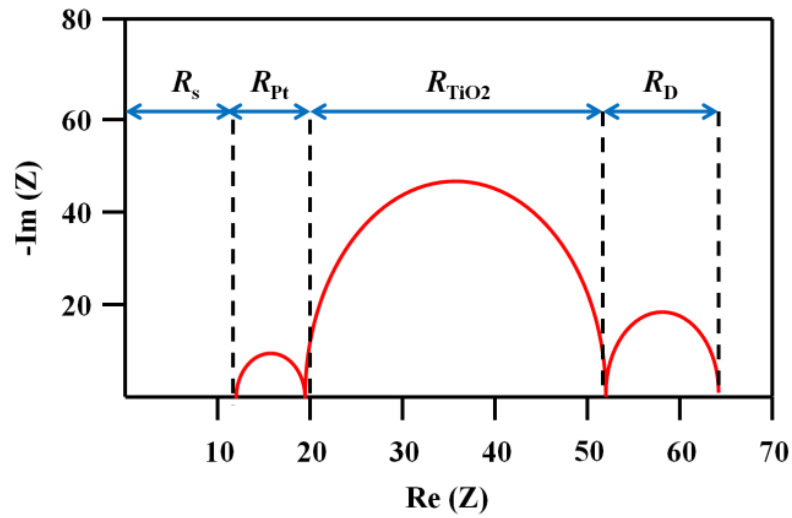


Figure 3.9 A typical EIS curve of a solar device measured at a specific point of the I - V curve (Halme et al. 2010). R_s is the sheet resistance of the FTO substrate, R_{Pt} is the charge transfer resistance at the Pt electrode, R_{TiO_2} is the charge transfer resistance at the TiO_2 /electrolyte interface and R_D is the charge diffusion resistance within the electrolyte.

The device was then supplied with a small amplitude, single frequency voltage, ($\Delta U = U_A e^{i\omega t}$) and the phase shift, θ and the resulting current, ($\Delta I = I_A e^{i(\omega t - \theta)}$), was measured. The impedance, ($Z = \left| \frac{\Delta U}{\Delta I} \right| = \left| \frac{U_A}{I_A} \right| e^{i\theta}$), is a linear system in which the current response follows the shape of the potential but shifts in phase at the same frequency. Although a change in the voltage will usually result in a nonlinear response, here the voltage was fixed to be so small (~ 10 mV) that the change can be assumed to be linear.

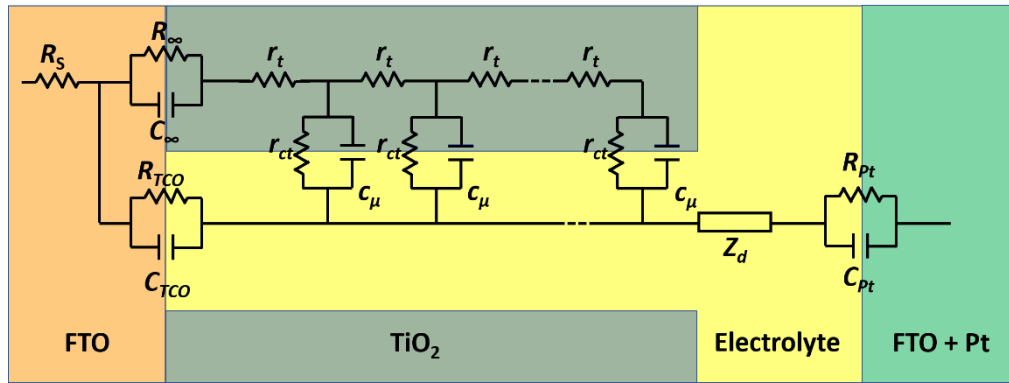


Figure 3.10 Equivalent circuit for liquid junction DSSC (Wang et al. 2006).

Under an applied bias, the electrons were injected from the TCO substrate to the conduction band of the TiO_2 (R_{TCO} and C_{TCO}) and then moved to neighbouring TiO_2 particles with a charge transfer resistance, R_t . Due to the back-recombination reaction, some of these electrons were intercepted by the electrolyte. This is characterised by R_{CT} and C_{μ} . The large R_{TCO} can be attributed to the inability of the FTO glass substrate to reduce the I_3^- into I^- . The Warburg impedance, Z_d describes the I^- diffusion within the electrolyte. The reduction of I_3^- into I^- is identified by R_{Pt} and C_{Pt} . All these parameters are described the paper by Wang *et al.* (Wang et al. 2006). Figure 3.10 shows the typical equivalent circuit to fit the impedance measurement for a liquid electrolyte DSSC.

3.4 Summary

In this chapter, the various apparatuses and procedures used in the experimental work were discussed. These methods were used to investigate the electro-optic, morphological, electrical, electrochemical and photovoltaic response of the materials.

Chapter 4 Device development

4.1 Foreword

DSSCs have attracted a lot of interest over the past few years due to their high conversion efficiency and easy and low-cost fabrication process. At present, extensive research is being carried out regarding the preparation of DSSCs. Available studies range from the development of a new oxide semiconductor for the photoanode to the development of new device architectures. The DSSC fabrication methods are wide ranging and include different mesoporous TiO_2 thicknesses, the incorporation of light scattering materials and the use of various plasticisers/additives in the electrolyte.

Here, we explored the fabrication of reproducible reference DSSCs. The chapter begins with the study of different electrolyte materials. As the focus of this research is to integrate LC materials in an electrolyte redox couple formulation, it is therefore of the utmost importance to establish the optimum electrolyte composition. Next, we determined the best method/material to be used as the spacer/sealant. After that, we determined the effect of different compact layer solutions to be used for the DSSCs. As dye immersion is also an important factor in DSSC fabrication, we explored the effect of the number of immersions. Finally, based on these experiments, we established the protocol for producing reproducible DSSCs.

4.2 Effect of different electrolytes

The effect of different electrolyte compositions has been investigated. Four different electrolytes were used in this study. The electrolytes were prepared by mixing tetrabutylammonium iodide (TBAI) (Sigma Aldrich, 98%), 4-dimethylaminopyridine (DMAP) (Sigma Aldrich, 99 %), I_2 and LiI together in acetonitrile and placing them in a shaker for 24 h until a homogenous mixture was obtained. The concentration for each electrolyte is given in Table 4.1 below.

Table 4.1 Different components of three different electrolytes.

Electrolyte	TBAI (M)	I ₂ (M)	DMAP (M)	LiI (M)
Electrolyte 1	0.6	0.06	0.5	0.1
Electrolyte 2	0.6	0.06	0.5	-
Electrolyte 3	0.6	0.06	-	-

These electrolytes used in DSSCs were prepared without fixed active areas and using adhesive tape as the sealant and spacers (90 μm). Figure 4.1 and Table 4.2 summarise the results. The best device was obtained using Electrolyte 1, showing an η of 1.01 %. This can be attributed to the high J_{sc} (2.44 mA cm^{-2}), V_{oc} (0.83 V) and FF (50.1 %). Electrolyte 3 showed the second-best result with J_{sc} (1.98 mA cm^{-2}), V_{oc} (0.79 V) and FF (35.4 %) resulting in η of 0.54 %. The worst performing device was obtained with Electrolyte 2 showing $\eta = 0.31$ % with J_{sc} (0.88 mA cm^{-2}), V_{oc} (0.78 V) and FF (40.0 %). The addition of LiI in the electrolyte clearly improved the performance of the solar devices. This can be explained by the chemical reactions occurring in the electrolyte as follows:



This shows that it is important to add LiI in the electrolyte because the redox reaction of the electrolyte involves the reduction of I_3^- into I^- , which eventually releases electrons. This led to a high J_{sc} in the case of Electrolyte 1 compared to Electrolyte 2. It was shown that Li^+ can absorb onto a TiO_2 surface and reduce the back-recombination reaction by providing electron screening. In addition, the absorption of the Li^+ up-shifted the quasi-Fermi level of the TiO_2 to a more negative value. This eventually led to an increase in V_{oc} because V_{oc} is determined from the difference between the Fermi level of the TiO_2 and the redox potential of the electrolyte.

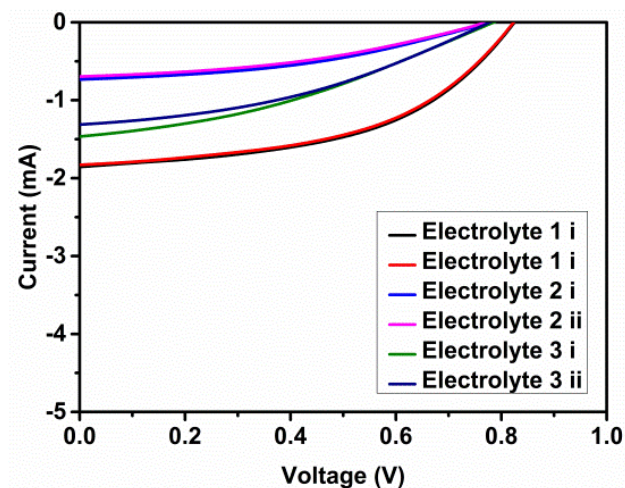


Figure 4.1 J - V curves of DSSCs using different liquid electrolytes measured under 1 sun illumination at 25 °C.

Table 4.2 Results for DSSCs using different liquid electrolytes measured under 1 sun illumination at 25 °C.

Parameters	Electrolyte 1		Electrolyte 2		Electrolyte 3	
	Cell 1	Cell 2	Cell 1	Cell 2	Cell 1	Cell 2
V_{oc} (V)	0.83	0.83	0.78	0.78	0.79	0.78
J_{sc} (mA cm ⁻²)	2.44	2.44	0.88	0.93	1.98	1.75
FF (%)	50.1	49.9	40.0	39.0	35.4	38.6
η (%)	1.03	1.00	0.31	0.28	0.54	0.53

4.3 Effect of different spacers and sealants

The leakage and evaporation of solvents are major setbacks for liquid-junction DSSCs. In this research, different spacer thicknesses and sealing techniques were investigated to find the method that works best for LC-based electrolytes. Figure 4.2 shows the J - V curves for DSSCs fabricated using different spacer thicknesses and sealing techniques. The result of each measurement is summarised in Table 4.3 First, spacer beads (38 - 42 μ m) were dispersed in acetonitrile and spin-coated onto a Pt counter electrode at a speed of 2000 r.p.m. Both the photoelectrode and counter electrode were held together using binder clips on two sides. The solar cell was then filled with liquid electrolyte. This type of DSSC showed the best performance of $V_{oc} = 0.77$ V, $J_{sc} = 11.51$ mA cm⁻² and $\eta = 4.35$ %. However, the cell was only stable for a few minutes before the solvent evaporated. Despite showing high efficiency, this type of device is not easy to replicate because the spacer beads leave scratches on the surface of the TiO₂ and Pt electrode every time the cell is sheared, especially when fixing the

two electrodes with binder clips. Next, double-sided tape was used as the spacer (90 μm). This gave device a performance of $V_{\text{OC}} = 0.71 \text{ V}$, $J_{\text{SC}} = 4.50 \text{ mA cm}^{-2}$ and $\eta = 1.89 \%$. Due to the thicker cell, the probability of back-recombination reaction was increased because there was more electrolyte to intercept the electrons in the TiO_2 . This was manifested through lower V_{OC} . In addition, the electron diffusion length was limited to a few microns. A thickness more than that of the electron diffusion length will result in an inefficient charge transport from the electrolyte into the metal oxide semiconductor. Finally, devices fabricated using UV curable glue with 20 μm showed the worst performance. It is thought that the solvent in the electrolyte reacted with the glue, leading to the low performance. In addition, due to the extra curing step required for this device, the UV light may have degraded the dye. It was observed that some of the glue seeped into the active area of the device and some of the electrolyte even seeped out of the device.

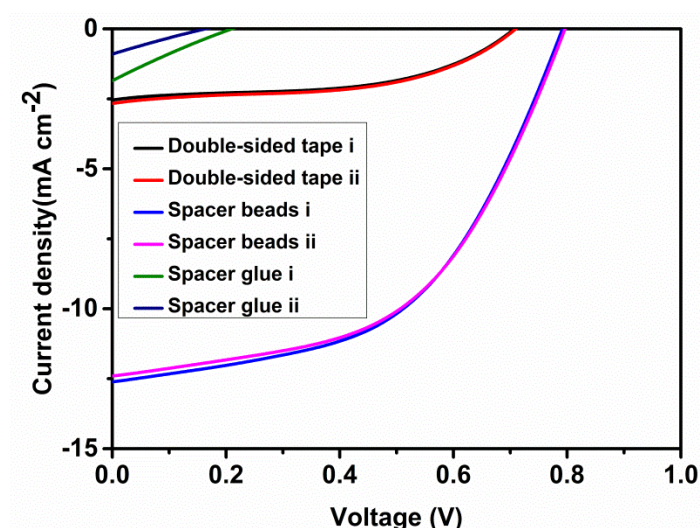


Figure 4.2 J - V curves of DSSCs using different spacers/sealants. Using the following electrolyte: 0.6 M DMPII, 0.5 M LiI, 0.05 M I_2 and 0.5 M TBP in acetonitrile.

Table 4.3 Results for DSSCs using different spacers.

Parameters	Spacer beads (40 μm)		Double-sided tape (90 μm)		Spacer glue (20 μm)	
	Cell 1	Cell 2	Cell 1	Cell 2	Cell 1	Cell 2
V_{OC} (V)	0.769	0.769	0.714	0.716	0.207	0.162
J_{SC} (mA cm^{-2})	11.51	11.49	4.98	5.25	1.22	0.594
FF (%)	49.16	49.11	53.24	51.93	23.04	23.51
η (%)	4.35	4.32	1.89	1.89	0.06	0.02

4.4 Effect of different compact layers

The use of a TiO₂ compact layer on photoanodes has been shown to reduce the series resistance and J_{sc} of solar devices by blocking the electron recombination by the electrolyte (Sangiorgi et al. 2014; H. Yu et al. 2009). This is because the compact layer has a significantly denser TiO₂ layer and the size of the particles is much smaller than in mesoporous TiO₂. This effectively reduces the contact surface area between the FTO substrate, and the electrolyte. Moreover, the high density of this layer improves the adherence of the TiO₂ compact layer and FTO substrate which facilitates the electron transfer process. This could not be obtained with the mesoporous TiO₂ because the surface contact area was limited by the porous nature of the layer.

Next, we investigated the effect of different compact layer formulations. The compact layer was prepared using two different solutions, solution A and solution B. The two solutions (50:50 vol%) were then mixed together for 24 h using a shaker. The different compositions of the compact layer solution are given in Table 4.4. The prepared compact layer mixtures were then spin-coated on clean FTO glass substrates at 2000 r.p.m for 60 s. The spin-coated substrates were annealed using the following protocol:

100 °C for 10 min (ramping rate: 7.5 °C min⁻¹)

150 °C for 10 min (ramping rate: 7.5 °C min⁻¹)

325 °C for 30 min (ramping rate: 7.5 °C min⁻¹)

450 °C for 30 min (ramping rate: 7.5 °C min⁻¹)

The substrates were then allowed to cool to room temperature naturally.

Table 4.4 Different compositions of compact layer mixtures.

Compact layer	Solution A	Solution B
Compact layer 1 (HCl)	2.5 ml EtOH + 35 µl 2 M HCl	2.5 EtOH + 350 µl TTIP
Compact layer 2 (Excess HCl)	2.5 ml EtOH + 2-3 ml 2 M HCl	2.5 EtOH + 350 µl TTIP
Compact layer 3 (IPA)	2.5 ml IPA + 35 µl 2 M HCl	2.5 IPA + 350 µl TTIP

Compact layers 1 and 2 resulted in very uniform thin films after annealing. Both samples showed thicknesses of approximately 100 nm when measured using a Dektak profilometer. However, in the case of Compact layer 3, the surface of the substrate appeared to be powdery even after annealing. It is thought that the IPA induced agglomeration of the TiO_2 particles in the solution because there was an excess of IPA. The film obtained appeared to be uneven, and the thickness obtained was 200 nm, which is thicker compared to the other two samples. Compact layer 1 showed the best performance with $V_{\text{OC}} = 0.75$ V, $J_{\text{SC}} = 8.50$ mA cm^{-2} and $\eta = 3.80$ %. The next best performance was obtained with Compact layer 2, with $V_{\text{OC}} = 0.71$ V, $J_{\text{SC}} = 10.04$ mA cm^{-2} and $\eta = 3.67$ %. The higher J_{SC} in the case of Compact layer 2 can be attributed to the better TiO_2 film formation. It has been shown that the TiO_2 compact layer is formed at a low pH environment. The addition of excess HCl reduced the pH of the solution, which improved the hydrolysis of the TTIP. Consequently, a better quality of TiO_2 was obtained. In the case of Compact layer 3, the low photovoltaic parameters ($V_{\text{OC}} = 0.77$ V, $J_{\text{SC}} = 6.52$ mA cm^{-2} and $\eta = 3.40$ %) obtained with this type of device were due to the poor quality of the TiO_2 compact layer film. The higher V_{OC} can be attributed to the better blocking effect of the back-recombination reaction due to the thicker TiO_2 layer. However, due to the un-even film surface and the agglomeration of TiO_2 particles on the surface of the substrate, the interfacial contact between the compact layer and the mesoporous layer suffered a mismatch, resulting in inefficient electron transport from the mesoporous layer to the compact layer. This is evident from the low J_{SC} .

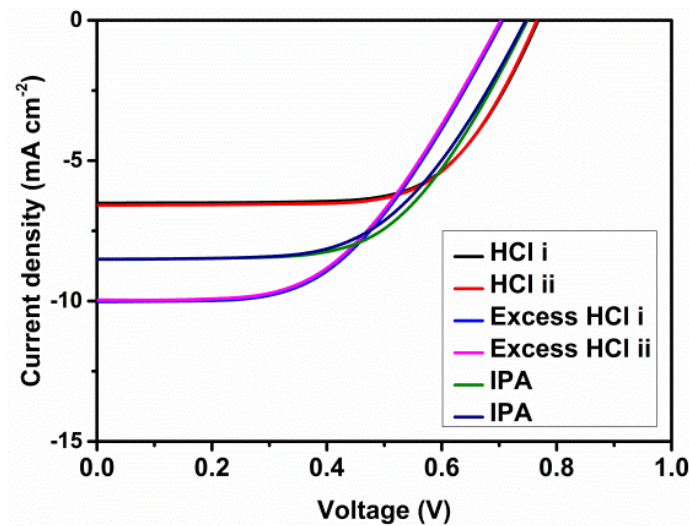


Figure 4.3 J - V curves of DSSCs using different compact layers.

Table 4.5 Results for DSSCs using different compact layers.

Parameters	<u>Compact layer 1</u>		<u>Compact layer 2</u>		<u>Compact layer 3</u>	
	Cell 1	Cell 2	Cell 1	Cell 2	Cell 1	Cell 2
V_{oc} (V)	0.75	0.74	0.71	0.70	0.77	0.77
J_{sc} (mA cm ⁻²)	8.50	8.51	10.04	9.95	6.52	6.58
FF (%)	60.0	57.7	51.6	51.7	67.4	67.6
η (%)	3.80	3.67	3.67	3.62	3.40	3.40

4.6 Effect of dye immersion

When the sensitising dye absorbs photons, electrons are excited from the dye into the conduction band of the TiO₂. The rate of this excitation depends on several factors, such as the type of solvent, dye-loading time, concentration and choice of dye. It has been established in many works that the optimum dye-loading time for N719 dye is 24 h at a concentration of 0.3 mM in acetonitrile:t-BuOH (Dell'Orto et al. 2012). In this study, we investigated the effect of the dye concentration after the first immersion of TiO₂ substrates. It is important to track how the concentration changes after the immersion of the photoanodes because the dye coverage depends on the concentration of the dye solution which significantly affects the efficiency of the solar device. Figure 4.4 shows the UV-Vis absorption of the N719 dye. As can be seen from the spectra, after the first immersion, the spectra showed less absorption, which corresponds to the reduced concentration of the solution. From this, the amount of N719 dye needed to be added to the solution after the first immersion can be calculated using the Beer-Lambert Law (Equation 4.1):

$$A = \epsilon lc \quad (4.1)$$

where A is the absorbance of the solution at a particular wavelength, ϵ is the molar attenuation coefficient, l is the length of the cuvette used in the measurement and c is the concentration of the solution. ϵ shows how strongly the material absorbs light at a given wavelength per molar concentration and since the material, in this case N719, is used throughout the measurement, ϵ will remain the same even after immersion of TiO₂ substrates.

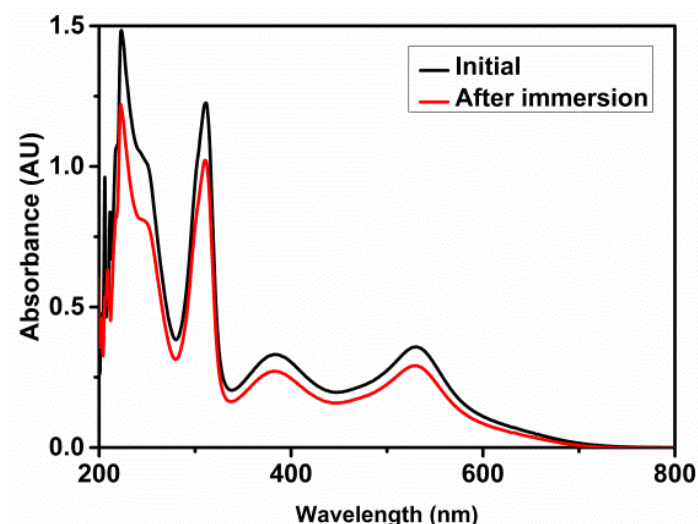


Figure 4.4 UV-Vis plot of N719 dye solution before (black line) and after immersion (red line).

4.7 Optimised device structure

Considering the studies discussed above, we established a protocol for fabricating DSSCs that is repeatable. This involves the use of an optimised compact layer (350 μl titanium tetraisopropoxide, 35 μl 2 M HCl in 5 ml anhydrous ethanol), liquid electrolyte (0.6 M DMPII, 0.5 M LiI, 0.05 M I_2 and 0.5 M TBP in acetonitrile), hot-melt sealing films (25 μm or 60 μm) and a mask with an area of 0.283 cm^2 to prepare the TiO_2 . This resulted in devices having an average efficiency of 5.50 %. Figure 4.5 shows the J - V curve for the optimised DSSC structure and the inset shows the DSSC.

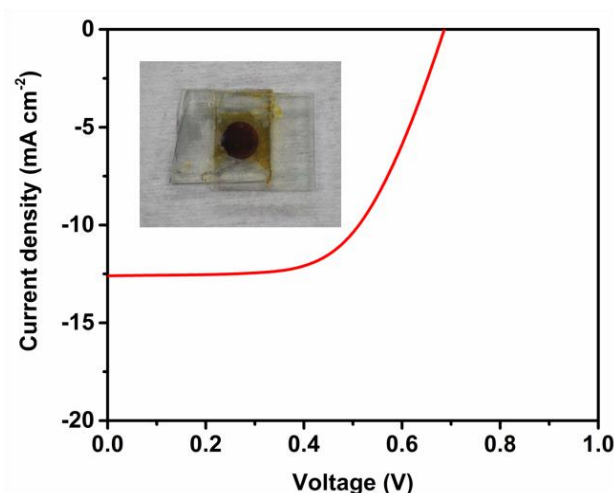


Figure 4.5 J - V curve of the optimised DSSC under light soaking measured at 25 °C under 1 sun illumination. The inset shows the DSSC with a circle-shaped active area (0.28 cm²).

4.7 Summary

In summary, we established an optimised DSSC fabrication method that gives reproducible results with efficiencies in the range of 5.00 % to 5.50 % for a reference liquid electrolyte. Earlier in this chapter, we explored the effect of different electrolytes and found that the use of LiI salts was very important in producing high-efficiency devices. Li⁺ was found to reduce the recombination reaction by passivating the surface of the TiO₂ and at the same time negatively shifting the conduction band of the oxide semiconductor, which led to increased V_{oc} . The increase in J_{sc} was due to the improved electron transport in the semiconductor after the Li⁺ ions adsorbed on the surface of the TiO₂ and provided electron screening for the electrons in the TiO₂. The use of spacer beads has shown that high-efficiency DSSCs can be achieved due to a more uniform thickness leading to more uniform charge transfer. Thicker cells increase the probability of recombination reaction between the electrolyte and the TiO₂, which led to the lower efficiency. The use of a smoother compact layer was found to give the best efficiency because the interfacial contact between the mesoporous layer and the compact layer allowed for an excellent charge transport mechanism by reducing the recombination loss between the FTO substrates and redox electrolytes. The investigation of the number of immersion times showed that the concentration of the dye should be adjusted every time it is used to coat the TiO₂. Finally, in the last section, we established a suitable protocol to fabricate DSSCs with reproducible results that will be used throughout this thesis.

Chapter 5 Crystal-polymer composite electrolytes

5.1 Foreword

This chapter explores the fabrication and characterisation of liquid crystal-polymer composites (LC-PEs) and their possible application in DSSCs. The principle benefits of these composite electrolytes are the light scattering effect, the electric field dependence and their ability to act as a thermal switch due to their temperature-dependent phase transition as a function of composition. These properties are of particular interest in the field of optoelectronics where an increase in the light scattering effect can help improve optical scattering. In particular, the increase of light scattering at elevated temperatures is useful for DSSCs because the efficiency of DSSCs degrades at elevated temperatures. Therefore, the improvement gained through light scattering may be a useful strategy to mitigate the decrease in efficiency at these temperatures.

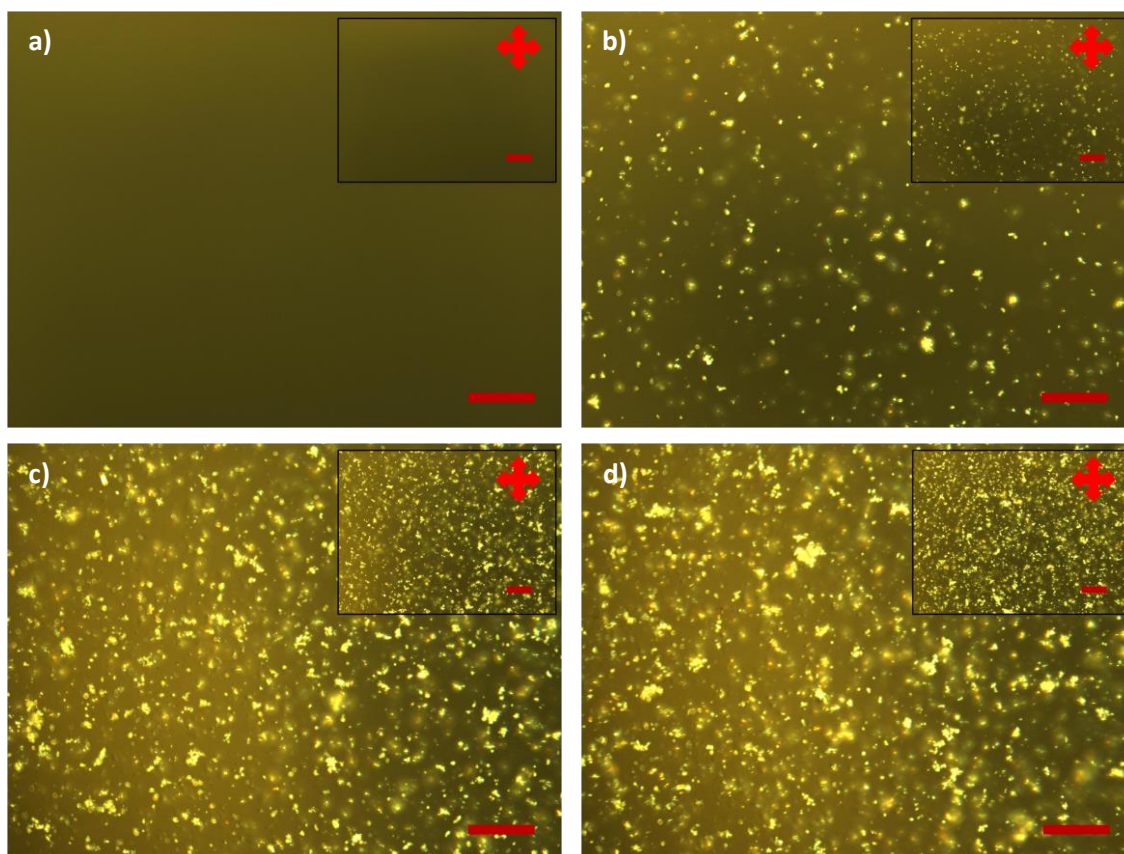
Here, we first study the morphology of the LC-PEs using POM and investigate the relationship in the phase transition temperature and material composition using DSC. This is followed by the investigation of electrical and electrochemical properties using a Wayne-Kerr parametric analyser and the EIS technique. The effect of light scattering is also explored for the LC-PEs. Finally, we focus on the applicability of these LC-PEs in DSSCs and relate the photovoltaic properties to the morphology and the electrical properties. This chapter is divided into three sections. The first section explores the variation of LC content in the LC-PE composition, the second section studies the effect of different LC alkyl chain lengths and the last section explores LC materials having different dielectric anisotropies.

5.2 Different variations of LC content

5.2.1 Polarising optical microscopy

Figure 5.1 shows the POM images of the pure polymer electrolyte and LC-PEs. Only a dark image was seen for the pure polymer electrolyte, which is indicative of the amorphous and optically isotropic nature of the polymer electrolyte. Upon doping the polymer electrolyte with 5 % 5CB, the aggregation of DMP11 ionic liquid was observed. The inset images were taken at 35 °C, which was above the transition temperature of 5CB. Even at this elevated temperature, there were no changes observed in the POM images. This means that the 5CB

dissolves in acetonitrile and that these aggregations were of DMPII ionic liquids and not the LCs. Despite the fact that the LCs were in the isotropic phase, the addition of LC materials increased the birefringence of the polymer system and allowed this aggregation to be observed. Because the chemical structure of the DMPII ionic liquid is similar to that of 5CB, the effect of optical anisotropy was strengthened when paired with 5CB molecules. This can be attributed to the attractive ion-dipole forces between the ions in the DMPII ionic liquid and the neutral 5CB molecules having dipoles (Fang et al. 2016; Soberats et al. 2015). The addition of a higher content of 5CB led to an even distribution of the aggregates throughout the polymer matrix. It can be seen that at higher 5CB concentrations, the presence of smaller DMPII clusters became more prominent. This can be attributed to the solvating effect of 5CB in which the cyano group (which is a polar group) was able to orientate the ionic liquid molecules. The interaction between the dipole molecule and the ionic molecule is further proven in Chapter 7.



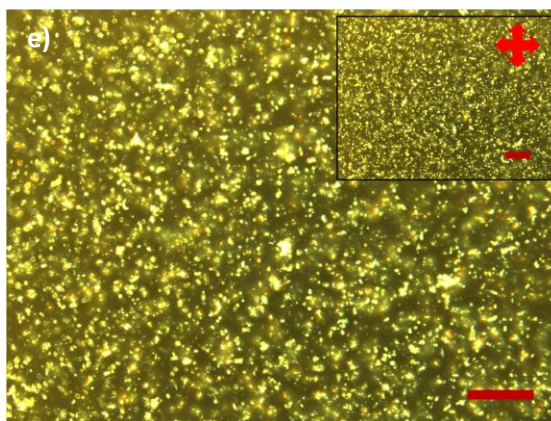


Figure 5.1 POM images of a) pure polymer electrolyte and LC-PEs with b) 5 %, c) 10 %, d) 15 % and e) 20 % of 5CB. The inset pictures are images taken at 35 °C. The solid bars equal 100 μm .

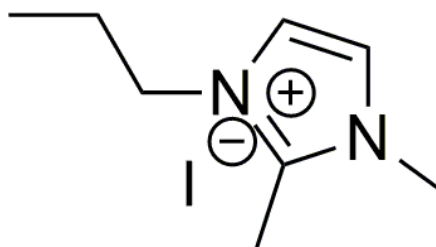


Figure 5.2 Chemical structure of the DMPHII ionic liquid.

5.2.2 Differential scanning calorimetry

Figure 5.3 shows a DSC thermogram of the pure polymer electrolyte and LC-PEs as a function of different LC concentrations. The curves showed a similar trend throughout all samples where no peaks that can be associated with the phase transition temperature of 5CB were observed. This reinforces the argument that the LCs were in the isotropic phase, as was observed using POM. The dip in the DSC curve in the region around 70 °C is attributed to the boiling point of the acetonitrile solvent.

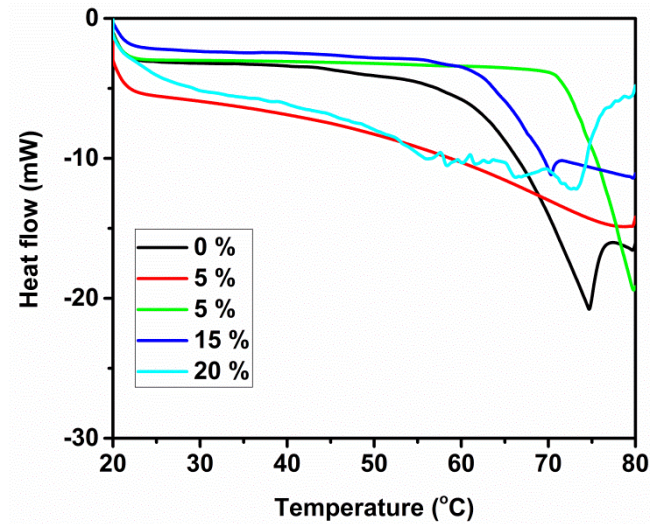


Figure 5.3 DSC curves of pure polymer electrolyte and 5CB-doped polymer electrolytes.

5.2.3 Current-voltage measurements

Table 5.1 summarises the ionic diffusion constant and the ionic conductivity for the different LC-PEs. The ionic diffusion constant was obtained using the current density limited method and a steady-state voltammogram. The diffusion coefficient can be calculated using the following Equation 5.1:

$$J_{lim} = \frac{2nFD_{I_3^-}c_{I_3^-}}{l} \quad (5.1)$$

where n is the electron number per molecule, F is the Faraday constant, $D_{I_3^-}$ is the diffusion coefficient of the limiting compound, and $c_{I_3^-}$ is the concentration of the limiting compound (Zistler et al. 2006). As can be seen from Table 5.1, the ionic diffusion increases with the increase of LC components despite LCs being quite viscous. However, as seen from the POM images, the addition of LCs to the polymer systems resulted in them being isotropic: therefore, the effect of viscosity can be neglected. The increase in the ionic diffusion reached the maximum value with 15% 5CB, after which the diffusion decreased. The initial increase can be attributed to the improved dissolution of the ionic salts. LC molecules such as 5CB are polar, and as the cyano group has an electron pair they are attracted to the positive Li^+ . Figure 5.4 shows the linear sweep voltammogram of the different LC-PEs.

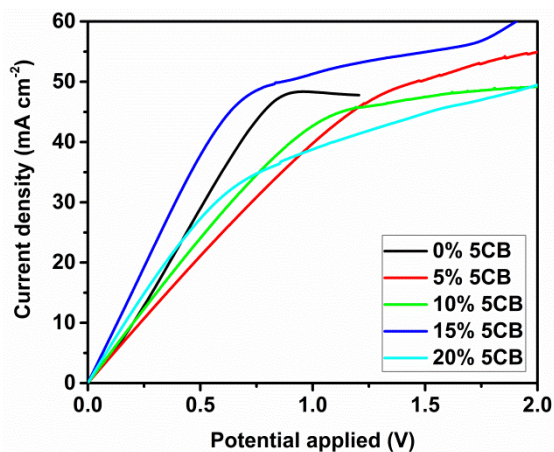


Figure 5.4 Steady-state voltammogram of different polymer electrolyte compositions. The scanning rate was 10 mV s^{-1} .

The current-voltage measurement was performed for the LC-PEs to measure the ionic conductivity. The conductivity of the LC-polymer electrolyte composite was obtained using the equation $\sigma = \frac{l}{R_b A}$, where l is the thickness of the cell, R_b is the resistance and A is the overlap area of the cell. The ionic conductivity of the pure polymer electrolyte was significantly lower than that of the LC-PEs. The highest conductivity obtained was with 15% 5CB showing $3.21 \times 10^{-3} \text{ S m}^{-1}$, which was more than 13 % of that of the pure polymer electrolyte. As evidenced from the POM studies, the addition of LCs resulted in the dispersion of the ionic liquid. At 5% LCs, the ionic liquid was characterised by the non-uniform aggregates. These aggregates were too big to allow efficient ionic conduction and at the same time slowed down the ionic diffusion. Above 10%, these aggregates were broken down into smaller aggregates that led to improved ionic diffusion and conductivity. However, at 20% 5CB, the ionic conductivity decreased significantly because this composition contains a higher proportion of LC molecules that were intrinsically insulating, thus reducing the overall ionic conductivity.

Table 5.1 Ionic diffusion and conductivity data for LC-PEs.

5 CB (%)	Ionic diffusion ($\text{m}^2 \text{ s}^{-1}$)	Ionic conductivity (S m^{-1})
0	1.45×10^{-6}	3.07×10^{-3}
5	1.50×10^{-6}	3.17×10^{-3}
10	1.39×10^{-6}	3.23×10^{-3}
15	1.50×10^{-6}	3.48×10^{-3}
20	1.04×10^{-6}	3.21×10^{-3}

In an electrolyte system, the conductivity increases with increasing temperature. Therefore, temperature-dependent conductivity measurements were performed for all the samples. Figure 5.5 shows the conductivity curves as a function of temperature. It is known that for a liquid electrolyte, an increase in the temperature leads to a linear increase in the conductivity. It is a well-known phenomenon; when an ionic conduction mechanism involves intermolecular ion hopping, the ionic conductivity shows a linear increase with temperature which is predicted by the Arrhenius equation (Equation 5.2) below:

$$\sigma = A \exp(-E_a/kT) \quad (5.2)$$

where A is a constant, T is the temperature in Kelvin and E_a is the activation energy. However, the relationship is non-linear as would be expected based on the Arrhenius equation. The curvature of the curves suggests that the conductivity of the polymer system obeys the Vogel-Tammann-Fulcher (VTF) equation (Diederichsen, Buss, and McCloskey 2017; Seki et al. 2005). According to the VTF equation, the ionic conduction mechanism in a polymer electrolyte is governed by the movement of the polymer chains. This can be explained by the use of the solvent and the polymer in the electrolyte where the ionic conduction is affected by the mobility and the free volume of the solvent/polymer (Gu et al. 2000; Miyamoto and Shibayama 1973). In addition, the segmental motion of the polymer also governs the ionic conductivity of the polymer electrolyte (Dam et al. 2014). Therefore, the plot is best described by the VTF equation (Equation 5.3) below:

$$\sigma(T) = AT^{-1/2} \exp[-E_a(T - T_0)] \quad (5.3)$$

where $\sigma(T)$ is the specific conductivity. A is a pre-exponential factor proportional to $T^{1/2}$, E_a is the activation energy related to the critical free volume for ion transport and T_0 is the reference temperature at which the ionic mobility vanishes, usually related to the glass transition temperature, T_g , of the polymer matrix (Ryu et al. 2005). As predicted by the above equation, the plot is non-linear and the ionic conduction is governed by the free volume of the polymer.

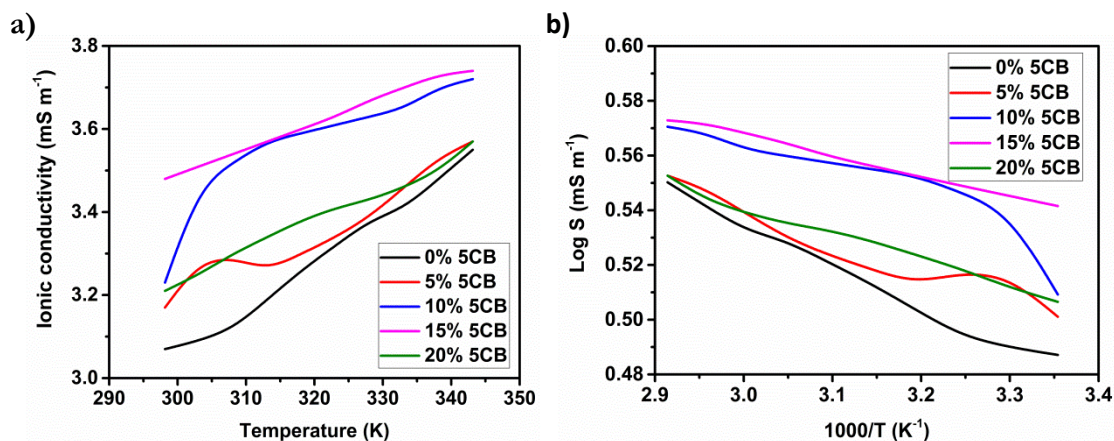


Figure 5.5 Plot of a) ionic conductivity and b) VTF as a function of temperature for LC-PEs.

5.2.4 Light scattering effect

To investigate the scattering effect of the LC-PEs, a red LED laser was incident onto a 60 μm thick ITO-ITO cell capillary-filled with the pure polymer electrolyte and LC-PEs. A beam stop was used to remove the saturated light, thus preventing it from being projected into the far-field. Figure 5.6 shows the scattering output for the pure polymer electrolytes and LC-PEs. It can be clearly seen that the output is different for polymer electrolytes doped with LCs. It can be qualitatively inferred from this experiment that the presence of LCs scatters the laser light more than just the sample without LC-doping. This corroborated the initial hypothesis that the LC-PEs act as a scattering layer due to increased refractive index disorder, which further improves the efficiency of the solar devices using these LC-PEs. This effect has been discussed by Hwang *et. al*/who show a higher efficiency with the use of a light scattering layer (Hwang et al. 2014). Instead of being allowed to pass through the device, the light was scattered within the electrolyte, which increased the probability of interacting with the dye molecules. This increase in the optical path length resulted in higher efficiency within the devices employing the LC-PEs.

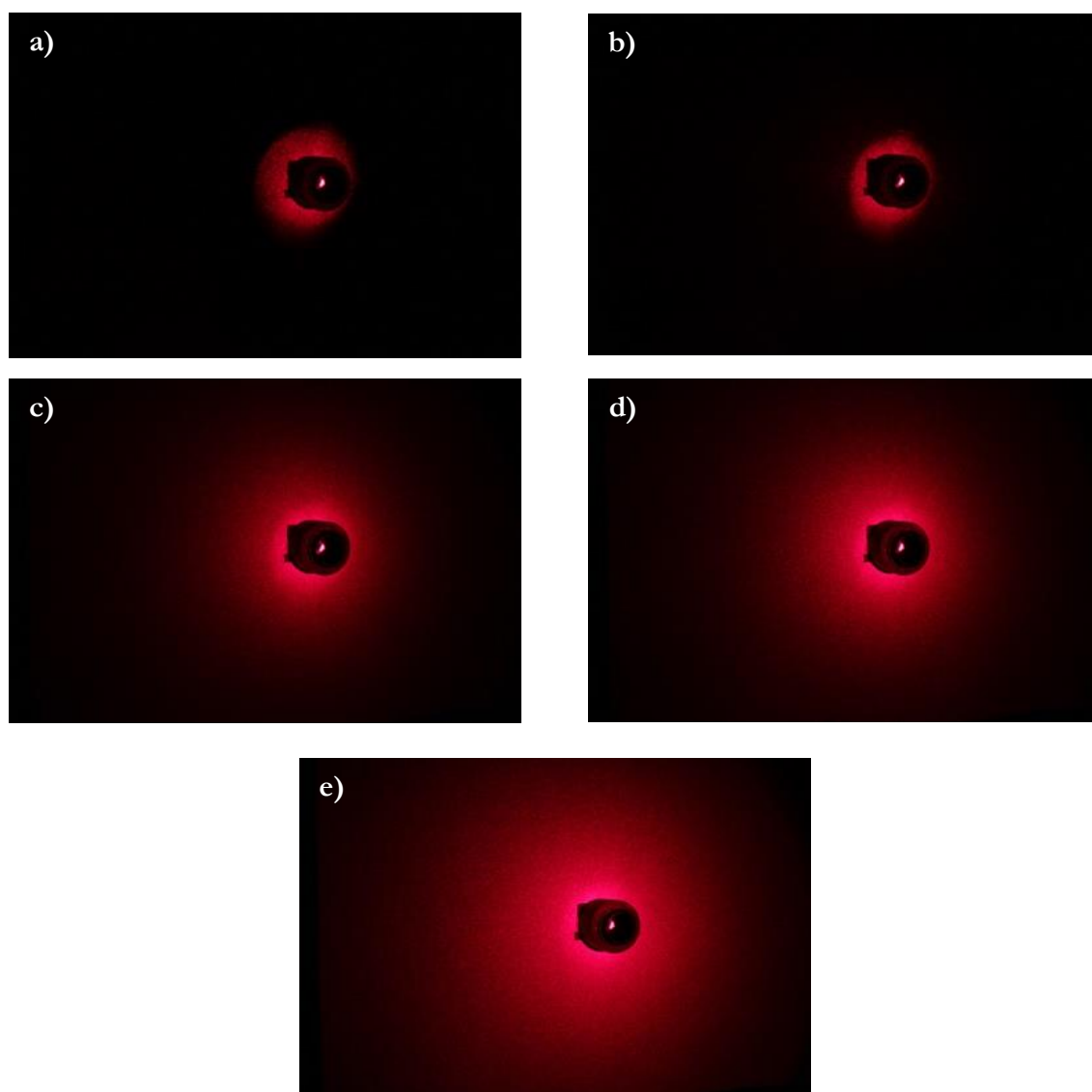


Figure 5.6 Scattering image projected in the far-field with different polymer electrolytes characterised at 25 °C in 25 μm ITO-ITO cell: a) 0 % 5CB, b) 5 % 5CB, c) 10% 5CB, d) 15% 5CB and e) 20% 5CB.

5.2.5 Photovoltaic properties

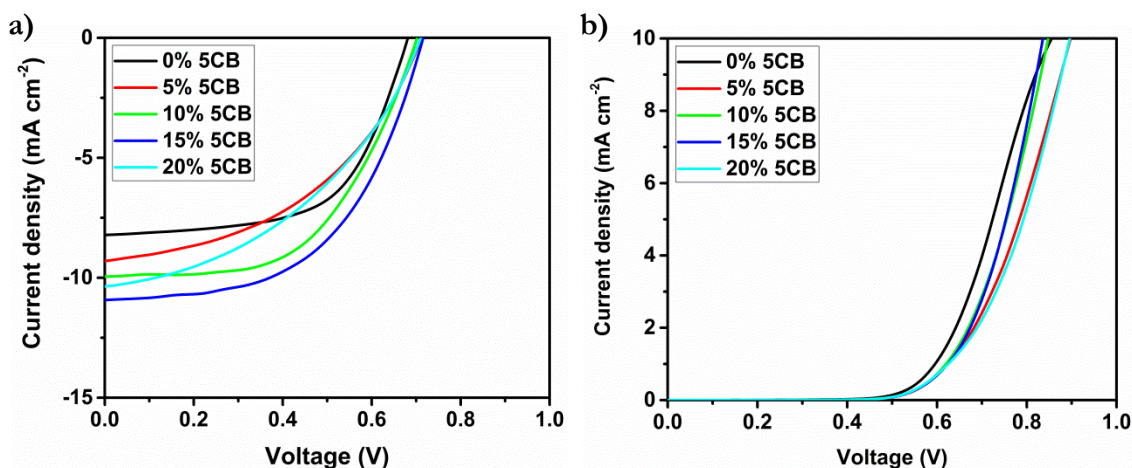


Figure 5.7 a) Light and b) dark J - V curves of DSSCs fabricated using pure polymer electrolyte and LC-PEs measured at 25 °C.

Figure 5.7 shows J - V curves of a DSSC fabricated using a pure polymer electrolyte and LC-PEs. For the pure gel polymer electrolyte, a J_{SC} of 8.71 mA cm^{-2} , a V_{OC} of 0.70 V and an efficiency of 2.83% was observed. The addition of LCs gave a maximum J_{SC} of 9.84 mA cm^{-2} and V_{OC} of 0.70 V which led to the highest power conversion efficiency, η , of 3.63% with $15\% \text{ 5CB}$. It was found that in all cases of 5CB addition, an increase in the J_{SC} and therefore an improvement was observed in η . The negligible difference in the V_{OC} can be attributed to the fabrication quality of the devices and not the material properties. The higher efficiency of DSSCs employing LC-PEs is the main contribution of the higher ionic conductivity. Gardiner *et al.* showed that the ionic conductivity for a SmA LC within a LC cell was different when measured perpendicular or parallel to the LC cell (Gardiner and Coles 2006). It is expected that the electronic/ionic conduction to be more efficient due to the ability of the LC molecules to assemble into a long-range orientational order. However, it could not be concluded the LC orientation on the ionic conductivity led to a more ordered ionic conduction since in this case the LC was in the isotropic phase. It can be hypothesised that the increase in the current came from the fact that there is additional Lewis acid-base interaction within the electrolyte through the addition of LC molecules.

The dark J - V curves provide qualitative information about the back-recombination reaction between the electrons in the TiO_2 and the electrolyte. It can be seen from Figure 5.7b that the onset of the dark current for a polymer electrolyte was several mV lower than the LC-PEs. This means that the recombination reaction is larger in the case of a pure polymer

electrolyte than for LC-PEs. This is to be expected since in the case of LC-PEs, the addition of LCs reduces the ratio of the polymer electrolyte. It has also been reported that LC molecules can adsorb onto the TiO₂ surface through the lone pair in the cyano group, thus reducing the probability of the electron in the semiconductor from being intercepted by the redox electrolyte (Koh et al. 2013). Table 5.2 summarises the photovoltaic performance of the devices.

Table 5.2 Photovoltaic performance of the DSSCs fabricated with different 5CB compositions measured at 25 °C under 1 sun illumination.

5CB (%)	J_{sc} (mA cm ⁻²)	V_{oc} (V)	FF (%)	η (%)
0	8.71	0.70	47.15	2.83
5	7.40	0.69	48.49	2.33
10	8.09	0.69	51.05	2.80
15	9.84	0.70	52.96	3.63
20	8.92	0.69	45.30	2.45

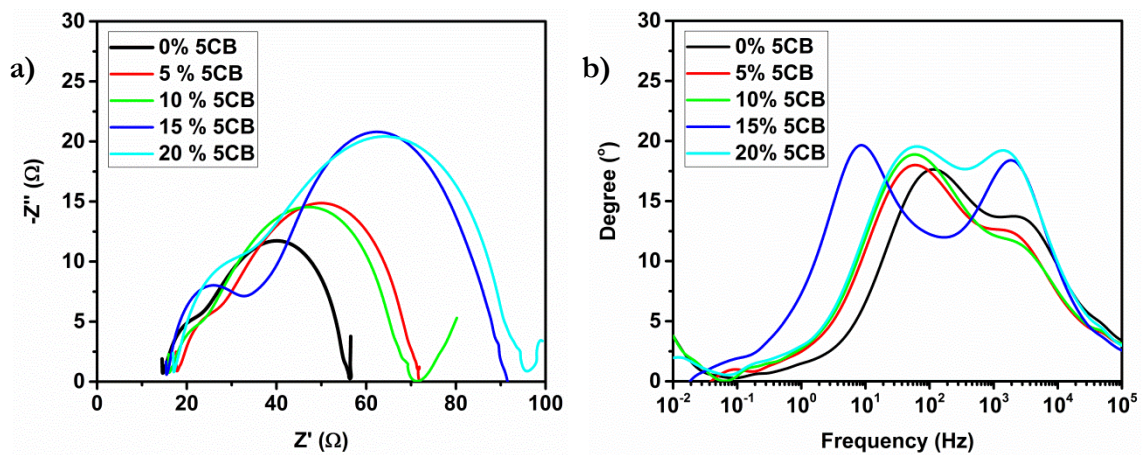
Usually, a light scattering layer is used in fabricating a DSSC to improve the efficiency by increasing the light absorption (Yang et al. 2011; Zhang et al. 2012). This light scattering layer is usually prepared from TiO₂ with different particle sizes. In this work, the employed LC-PEs are believed to have additional light scattering effects due to the birefringent LC materials that cause Mie scattering which is a well-known characteristic of PDLCs (Mie 1908). Due to their birefringence, the LCs bend and scatter the light pathway within the polymer. This allows the light to have an increased travelling distance. The photon therefore has an improved chance of exciting the dye and thus increases the electron excitation rate. The light scattering effect of the LC-PEs is supported by the POM result and light scattering experiments.

5.2.6 Impedance spectroscopy

EIS measurements were performed to investigate the charge transport mechanism in the devices (Que et al. 2016; Yang et al. 2016; Zhang et al. 2015). There are two different ways to represent impedance spectra: Nyquist and Bode plot. In the Nyquist plot, the impedance is plotted against a complex plane. In this case, the change of individual charge transfer as a function of frequency is not obvious. In addition, the small impedances are swamped by the large impedances. Whereas, in the case of Bode plot, the impedance and phase are plotted as a function of frequency. Figure 5.8 shows the a) Nyquist plot and b) Bode plot of the

devices measured under dark conditions at an applied bias of -0.7 V. The series resistance is a major parasitic resistance that significantly affects the performance of a solar cell. The series resistance originated from the different charge transfer process at the Pt electrode, the charge carrier transport in the electrolyte and the sheet resistance of the FTO substrate. Usually, the EIS data will show three semicircles; each are attributed to different processes and are fitted using the following equivalent circuit (Figure 5.8c) (Ahmed et al. 2011; Xu et al. 2016). However, in some cases, two of the three semicircles might combine to form only one semicircle as has been obtained in this work. This is due to the high resistance within the device. R_s is the Ohmic series resistance which comes from the sheet resistance of the substrates, resistivity of the electrolyte and the electrical contact between the substrate and the crocodile clip.

In this study, the R_s for all the devices are similar as they use the same FTO substrates and electrical wiring of the cell. R_{Pt} , which is related to the charge transport resistance at the Pt surface, was observed to increase with the increase of LC concentration. This is to be expected because higher LC contents means more LC molecules that can gather near the surface of the Pt electrode and reduce the surface area for catalytic reaction of the redox electrolyte. R_{CT} relates to the TiO_2 /electrolyte interfacial charge transfer resistance in the cell. A positive trend was seen in the R_{CT} , where increasing the LC concentration increased the R_{CT} ; this can be attributed to the passivating effect of the cyano group on the surface of TiO_2 .



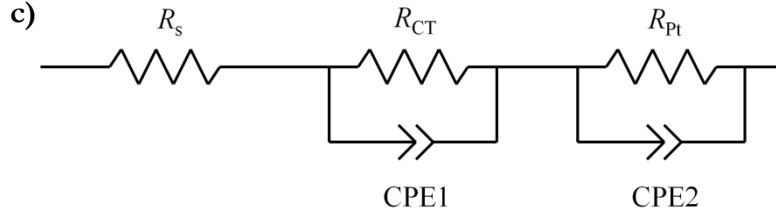


Figure 5.8 a) Nyquist plot and b) Bode plot of the DSSCs employing LC-PEs measured at 25 °C in dark conditions. c) The equivalent circuit of the DSSC to determine the resistances.

The electron lifetime can be calculated from the Bode plot using the following equation (Equation 5.4):

$$\tau_e = \frac{1}{2\pi f_{max}} \quad (5.4)$$

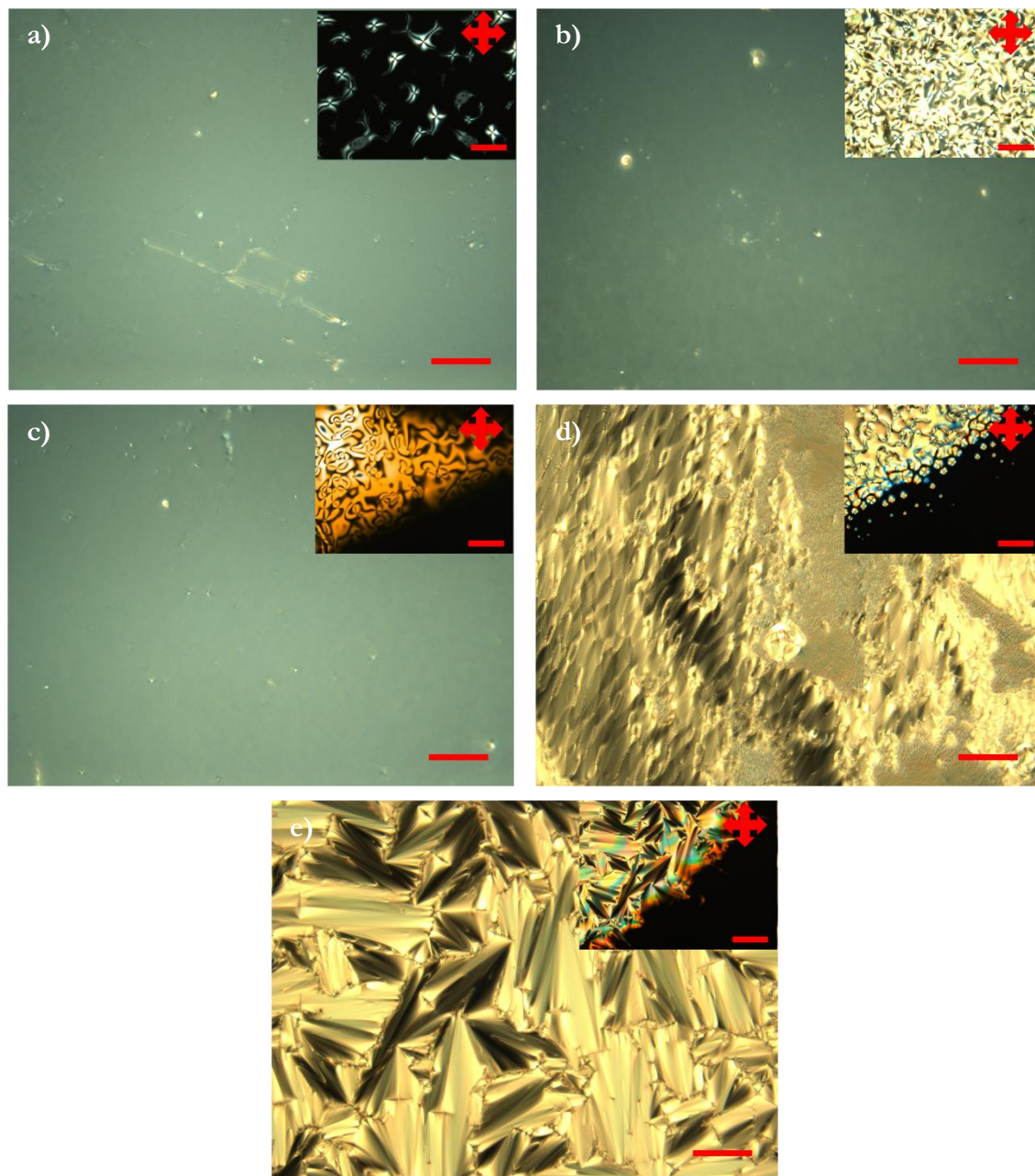
The addition of LCs clearly increased the electron life-time, as shown in Table 5.2, with the pure polymer electrolyte showing the shortest τ_e of 1.4 ms. This shows that τ_e in the case of LC-PEs was prolonged. This points to the fact that the back reaction between the TiO_2 and the electrolyte was suppressed by the presence of the LCs in the polymer electrolyte, which is thought to have adsorbed on the surface of the TiO_2 . This reduced the parasitic recombination loss by the electrolyte.

Table 5.3 Summary of charge resistance at interfaces and electron lifetime of DSSCs employing different LC-PEs measured at 25 °C in dark conditions.

5CB (%)	R_s (Ω)	R_{Pt} (Ω)	R_{CT} (Ω)	τ_e (ms)
0	14.6	8.7	33.1	1.4
5	17.8	9.5	44.4	2.7
10	16.0	7.3	48.1	2.8
15	15.5	17.4	58.5	17.5
20	17.1	18.2	60.6	2.6

5.3 LCs with different alkyl chain lengths

5.3.1 Polarising optical microscopy



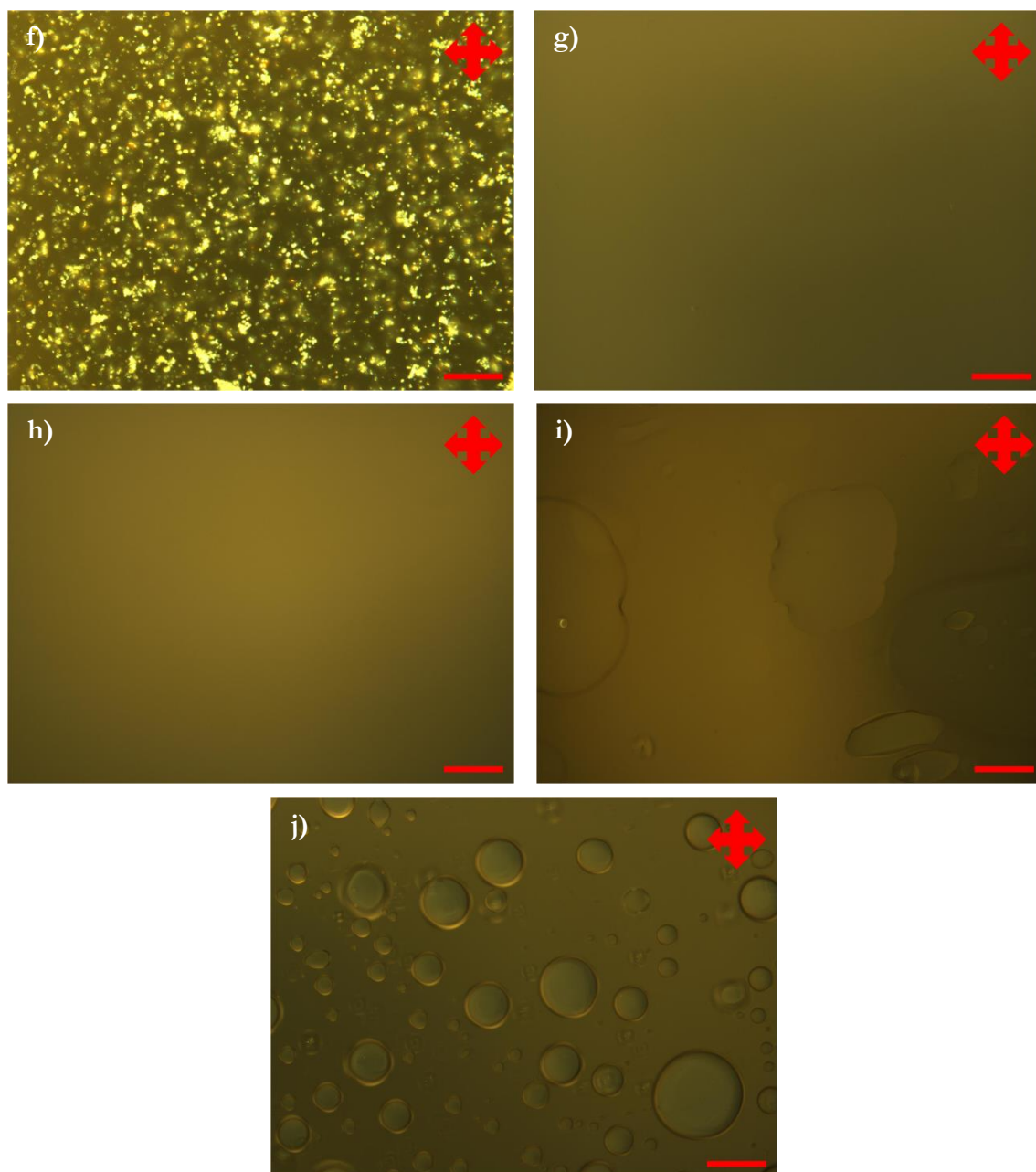


Figure 5.9 Optical micrographs of pure LC materials: a) 5CB, b) 6CB, c) 7CB d) 9CB and e) 10CB at 25 °C under crossed polarisers. The insets show the images near the isotropic temperature. The optical micrographs for the corresponding LC-PEs for 15 wt% f) 5CB, g) 6CB, h) 7CB i) 9CB and j) 10CB. Scale bar is 200 μm (inset is 100 μm).

Figure 5.9(a-e) shows the optical textures of the pure LC materials, and the corresponding textures in LC-PE composites are shown in Figure 5.9(f-j). The characterisations were performed in capillary filled 25 μm ITO-ITO cells. In an ITO-ITO cell without alignment layers, pure 5CB (Figure 5.9a), 6CB (Figure 5.9b) and 7CB (Figure 5.9c) showed the same texture, which was homeotropic. Upon heating near to their isotropic temperatures, the

change in the morphology can be seen where the Schlieren texture, which is typical for nematic LCs, can be observed in the inset pictures. 9CB is known for its multiple intermediate phases, namely the nematic and SmA phases. 9CB and 10CB show a focal conic texture (SmA phase) in their LC phases, shown in Figures 5.9d and 5.9e, respectively. The inset pictures show the materials in the nematic phase. However, due to the narrow temperature range of the nematic phase in 10CB, only the SmA phase was observed.

The LC-PE composites of 5CB showed bright clusters thought to be the DMPII ionic liquid dispersed throughout the polymer system. DMPII has a similar chemical structure to 5CB, as shown in Figure 5.2. The addition of 5CB strengthens the optical anisotropy behaviour of DMPII and allows it to be observed under the POM. The polymer electrolyte is characterised using POM by dark regions, which is indicative of the amorphous and optically isotropic nature of the polymer. In the case of 6CB (Figure 5.9g) and 7CB (Figure 5.9h), the bright clusters can no longer be seen. The difference in the alkyl chain of DMPII and 6CB suppressed the optical anisotropy of the system where the DMPII molecules are thought to have induced disorder in the LC system on a bulk level. The addition of LCs with longer alkyl chain lengths effectively increased the solubility of DMPII in acetonitrile. There are also reports on the use of LC materials as solvents which explains why the solute, in this case DMPII molecules, tends to align according to the solvent molecules due to the dispersion force interactions (Dunmur and Toriyama 1995; Yim and Gilson 1971). The addition of longer alkyl chain LCs in the case of 9CB and 10CB changed the morphology of the polymer electrolytes as the LC-PEs now contained droplets within the polymer matrix. However, these droplets were optically isotropic (Figures 5.9i and j). Although no LC phase can be seen here, it is indicative that the polymer electrolyte contains LC material. The formation of droplets can be related to the LC phase of the pure material. Both 9CB and 10CB showed a SmA phase. However, only the LC-PE with 10CB showed uniform droplet structures due to the more ordered nature of 10CB as can be seen from the broad temperature range of the SmA phase.

5.3.2 Differential scanning calorimetry

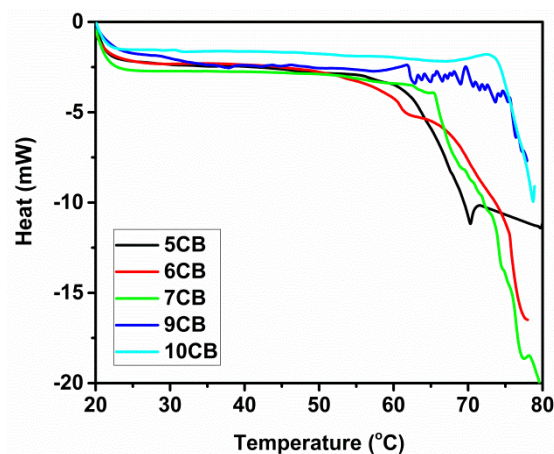


Figure 5.10 DSC curves of LC-PEs with LC content of 15 wt% at a scanning rate of 5 °C min⁻¹.

To quantify the phase transition temperatures of the LCs, DSC measurements were performed for the LC-PE composites. Figure 5.10 shows the measured DSC curves. Based on the DSC curves, it is noted that the transition temperatures of the pure LCs could not be observed in the composite electrolytes. This showed that the LC materials were completely dissolved in the polymer electrolyte and were in the isotropic phase. For the 5CB, 6CB and 7CB samples, the onset of the dip started to appear at around 60 °C. However, in the case of 9CB and 10CB, the appearance of the dip occurred above 75 °C, which is close to the boiling point of acetonitrile (80 °C). It can be speculated that the longer alkyl chains acted as a trap and slowed down the rate of evaporation of the solvent. Table 5.4 shows the summary of the transition temperatures of pure LC materials. Table 5.3 shows that the cyanobiphenyl LCs showed an odd-even effect in the transition temperature, something that has been reported elsewhere (Karat and Madhusudana 1976). According to the odd-even effect, LCs with an even number of alkyl chains show higher transition temperatures than LCs with an odd number of alkyl chains. It has been proposed that this effect is due to alternating polarisabilities of the molecule backbone and the tendency of the molecule to form a gauche conformation. However, it could not be concluded that the odd-even effect was replicated in the LC-PEs because the LCs were in the isotropic phase.

Table 5.3 Transition temperatures of the different alkyl-cyanobiphenyl LCs as provided by BDH Chemicals.

Name	K \rightarrow N or K \rightarrow SmA (°C)	SmA \rightarrow N (°C)	N \rightarrow I or SmA \rightarrow I (°C)
5CB	24	-	35.3
6CB	14.5	-	29
7CB	30	-	42.8
9CB	42	48	49.5
10CB	44 (SmA)	-	50.5

5.3.3 Current-voltage measurement

The effect of the LC alkyl chain length on ionic conductivity and ionic diffusion is studied in the following section. The ionic conductivity measurement was performed using a Wayne-Kerr component analyser. The ionic conductivity of the LC-PE composites was calculated using a simple linear resistor model, $\sigma = \frac{l}{RA}$, where l is the thickness of the cell, R is the measured resistance of the material and A is the active area of the cell. Figure 5.11a shows the ionic conductivity graph, and Figure 5.11b summarises the ionic conductivity as a function of different alkyl chains. Table 5.4 summarises the ionic conductivity and the corresponding ionic diffusion constants. As the alkyl chain length was increased from 5CB to 10CB, a decrease in the ionic conductivity was observed. This was to be expected because the longer the alkyl chain, the more insulating is the material. It is hypothesised that the long alkyl chains might become intertwined with adjacent chains, and instead of providing a pathway for ionic conduction, these intertwined chains trap and hinder the movement of the free ions. This effectively reduces the mobility of ions in polymer electrolyte systems and leads to low ionic conductivity. In addition to this, shorter alkyl chain lengths mean lower viscosity of the LC material. It has been shown that higher viscosity materials show lower ionic conductivity. This is also applicable in this case, where increasing the alkyl chain length of the LCs decreased the ionic conductivity of the LC-PEs. This has been explained by Leonas *et al.*, who found that ionic liquid with shorter alkyl chains show higher conductivity due to the lower viscosities and thus facilitate ion mobility (Leones et al. 2014; Leones et al. 2015).

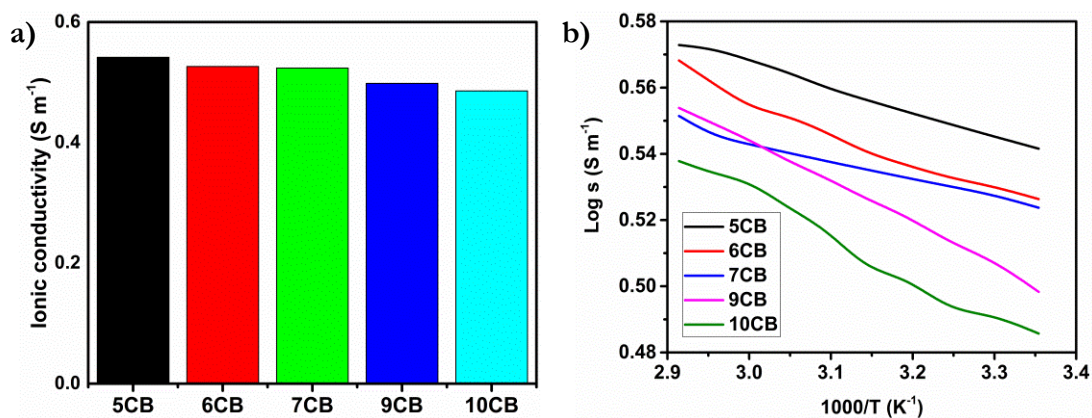


Figure 5.11 Plot of a) ionic conductivity across different LC materials measured at 25 °C at 1 kHz in an ITO-ITO cell (25 μm) and b) ionic conductivity as a function of temperature.

Figure 5.11a shows the measured ionic conductivity as a function of temperature. The plot is non-linear which means it obeys the VTF equation. This is to be expected because they are polymer systems, and polymeric materials have been shown to facilitate ionic conductivity.

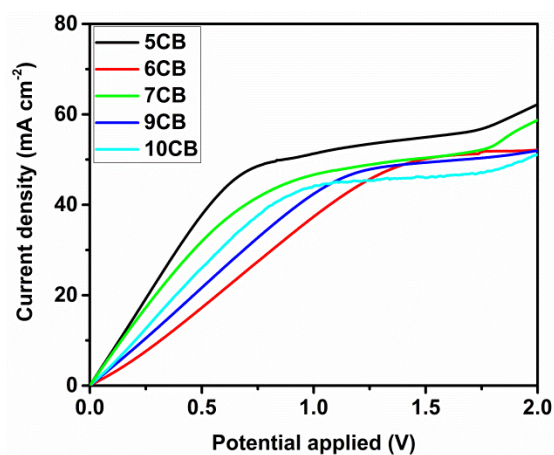


Figure 5.12 Linear sweep voltammetry of LC-PEs measured at 25 °C in a symmetric Pt-coated FTO-FTO cell (60 μm).

The general trend that can be seen from the linear sweep voltammogram (Figure 5.12) is that increasing the length of the alkyl chain decreases the ionic diffusion. This can be related to the morphology of the LC-PEs where higher alkyl chain length LCs resulted in the formation of micron-sized droplets. It is thought that the aggregation of the LCs forming these droplets hindered the movement of the ions and at the same time trapped the ions within the aggregation. Unlike the phase transition temperature, there was no direct co-relationship between the alkyl chain length and ionic conductivity/diffusion.

Table 5.4 Summary of the ionic conductivity for different LC-PEs with LC content of 15 wt%. The measurement was performed at 25 °C in a 60 μm ITO-ITO cell.

Sample	Ionic diffusion ($\text{m}^2 \text{s}^{-1}$)	Ionic conductivity (mS m^{-1})
5CB	1.50×10^{-6}	3.48
6CB	1.53×10^{-6}	3.36
7CB	1.36×10^{-6}	3.34
9CB	1.44×10^{-6}	3.15
10CB	1.37×10^{-6}	3.06

5.3.4 Photovoltaic properties

Subsequently, the LC-PE composites were used to fabricate DSSCs. The J - V curves and a summary of the solar cells' parameters are shown in Figure 5.13 and Table 5.6, respectively. It can be seen that there is a clear trend in that the use of LCs with longer alkyl chains leads to a decrease in the power conversion efficiencies with the increase in the chain length. The highest efficiency was recorded with the 5CB LC-PE composite where $V_{\text{OC}} = 0.70 \text{ V}$, $J_{\text{SC}} = 9.84 \text{ mA cm}^{-2}$ and $FF = 53.0 \%$, corresponding to η of 3.63 %. The lowest efficiency was obtained with the 10CB sample with $V_{\text{OC}} = 0.65 \text{ V}$, $J_{\text{SC}} = 6.38 \text{ mA cm}^{-2}$ and $FF = 50.7 \%$, corresponding to η of 2.06 %.

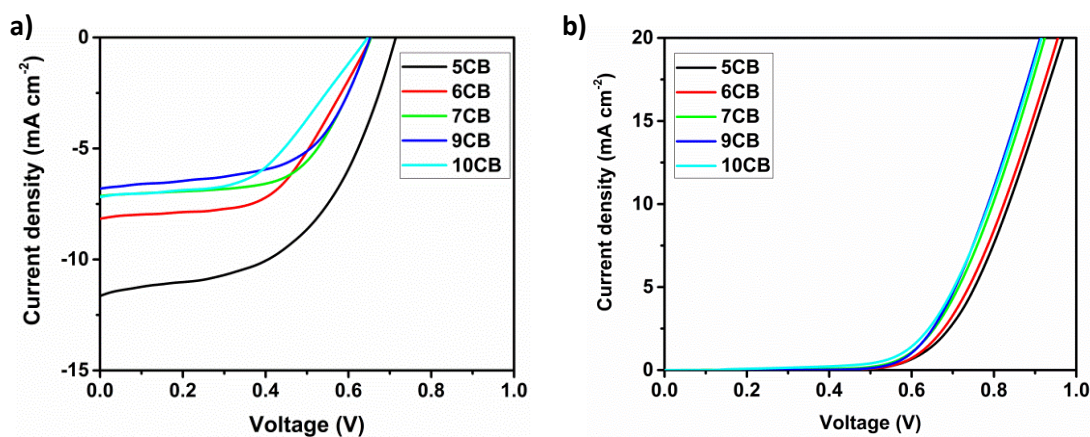


Figure 5.13 a) Dark and b) light J - V curves of DSSCs using polymer electrolytes with different alkyl chain lengths measured at 25 °C under 1 sun illumination.

It can be seen from the table that the J_{SC} decreased with the increase in the chain length which corresponds well with the ionic conductivity data. As noted in the previous section, a longer alkyl chain resulted in the molecules being more insulating. This long alkyl chain is thought to trap the mobile ions in the system. The addition of the cyanobiphenyl groups to

DSSCs has been shown to increase the V_{oc} . However, in this case, the V_{oc} dropped from 0.70 V to 0.65 V when the alkyl chain length was increased. It is interesting to note that V_{oc} remains constant with the increase in alkyl chain length, indicating the limited effect of the alkyl chain length on the V_{oc} . In addition, the increase in the alkyl chain length led to the increase in the viscosity of the LC samples.

As the alkyl chain length was increased, the longer LC molecules tended to retain their original LC phases within the polymer electrolytes as has been shown in the transition temperature of the LC materials within the polymer electrolyte composites also increased. An increase in the structural order, such as in the case of the SmA LC-PE composites, increased the glass transition temperature (T_g), which is not ideal for a polymer electrolyte system. A low T_g is important to achieve high ionic conductivity at room temperature. Above T_g , the polymer has lower crystallinity and a higher fraction of the polymeric regions are in an amorphous state, thus allowing for greater ionic movement within the electrolyte system.

Table 5.5 Photovoltaic performance of DSSCs based on LC-PEs measured under 1 sun illumination at 25 °C.

Device	J_{sc} (mA cm ⁻²)	V_{oc} (V)	FF (%)	η (%)
5CB	9.84	0.70	53.0	3.63
6CB	8.06	0.66	53.7	2.84
7CB	7.75	0.64	53.9	2.61
9CB	6.68	0.66	58.4	2.57
10CB	6.38	0.65	50.7	2.06

The dark J - V characteristics of the LC-PE composite solar cells are shown in Figure 5.13b. Under dark conditions, electron injection from the dye molecule is prohibited and the current diffusion is limited to the electrons travelling from the TiO₂ conduction band into the electrolyte (Penny et al. 2004). As can be seen from the figure, the onset of the dark current increases with the decrease in alkyl chain length. This shows that the electron recombination reaction is better suppressed with shorter alkyl chain lengths. It is expected that the shorter alkyl chain length molecules fill the spaces on the surface of the TiO₂ between the dye molecules and thus lower the possibility of the electrons in the TiO₂ being intercepted by the electrolyte. The longer alkyl chain molecules become entangled with the alkyl chain of the sensitizer and will not be able to passivate the surface of the oxide semiconductor. The higher V_{oc} in the case of 5CB can be attributed to the 5CB molecules being adsorbed on the surface

of the TiO_2 ; this up-shifted the conduction band edge of TiO_2 . The adsorption of the cyano group in the LC materials onto the TiO_2 surface due to the presence of an electron pair has been reported by Koh *et al.* (Koh et al. 2013). Figure 5.14 shows an illustration of a proposed adsorption mechanism for LC materials.

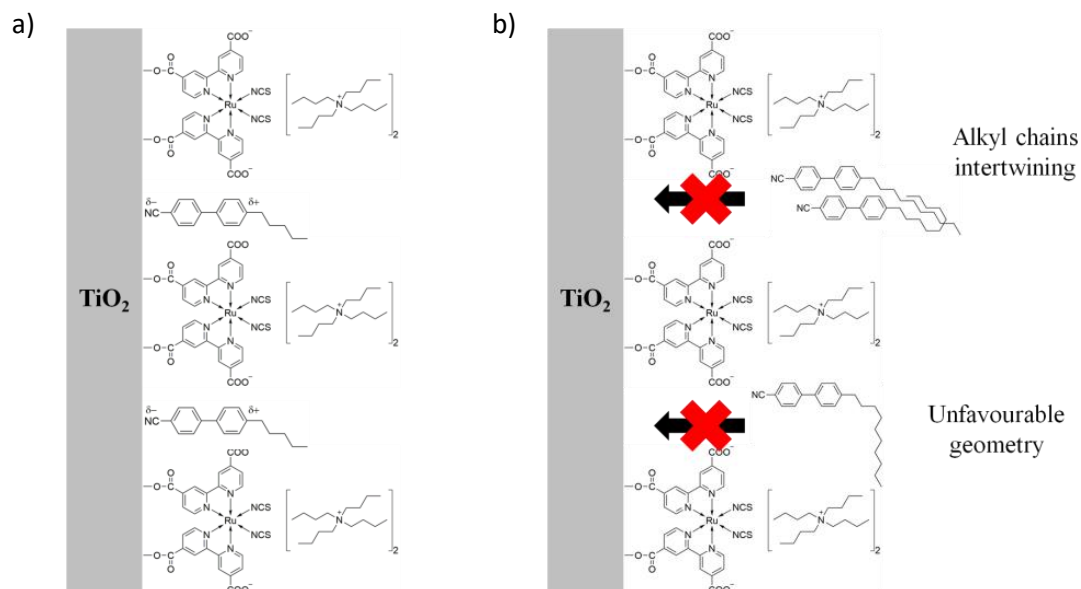


Figure 5.14 Schematic diagram of LC adsorption onto TiO_2 in a) 5CB and b) 10CB.

5.3.5 Electrochemical impedance spectroscopy

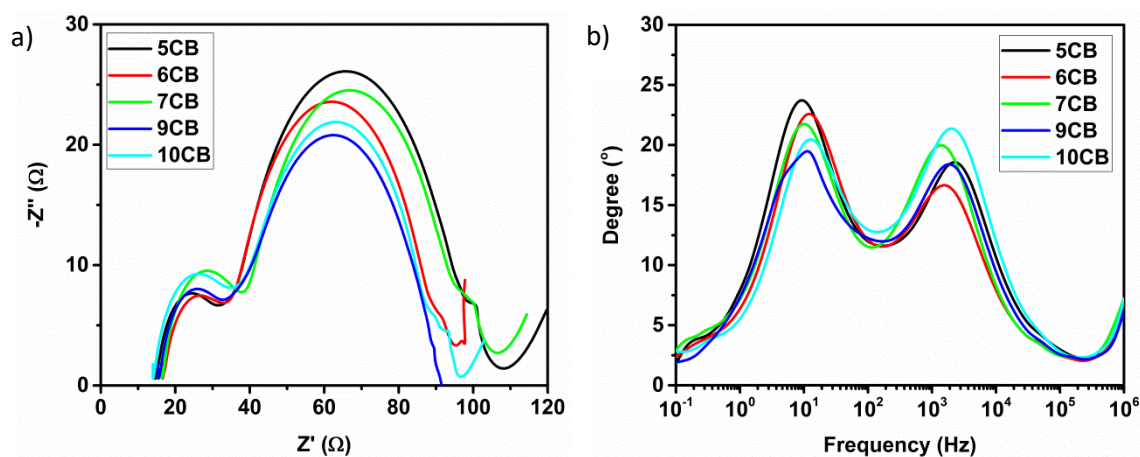


Figure 5.15 Impedance spectra of the DSSCs employing the LC-PEs. a) Nyquist plot and b) Bode plot measured in dark conditions at -0.70 V; applied voltage measured at 25°C .

As can be seen from the Nyquist plot (Figure 5.15a), the starting point for the semicircles were almost equal for all the samples. This was to be expected as the same FTO substrate and electrical wiring was used for all devices. R_{Pt} is higher in the case of shorter alkyl chain

length LCs because these LCs tend to dissolve completely in the polymer electrolyte and are distributed near the surface of the Pt electrode, which could potentially reduce the catalytic reaction of the electrolyte. However, longer alkyl chain LCs tend to form droplets that are less likely to be evenly dispersed throughout the polymer electrolyte. R_{CT} was observed to be smaller in the case of shorter alkyl chain LCs, which points to the passivation of the TiO_2 surface by the cyano group. This agrees with the observation of the dark current that showed the recombination reaction is less in the case of lower alkyl chain LCs.

It was also observed that the R_{Pt} and R_{CT} for longer alkyl chain LCs were lower than those of 5CB. This can be related back to the POM study where for shorter alkyl chain LCs, the molecules dissolved completely in the polymer electrolyte and hence were homogeneously distributed within the polymer system. These molecules are also thought to be distributed near the surface of the Pt counter electrode. This effectively decreased the probability of I_3^- to be reduced into I^- and thus the increased charge transfer resistance. However, longer alkyl chain LCs tended to form agglomerates from the intertwining of adjacent alkyl chains, as evidenced by the POM images.

From the Bode plot, τ_e of each device can be calculated using Equation 5.2. An increase in the alkyl chain length caused the peak of the medium frequency to shift to the right, which means that the electron transport process becomes slower. The result for the electron lifetime is as summarised in Table 5.7. The high electron lifetime (17.5 ms) in the case of the 5CB sample can be attributed to the reduced surface charge recombination in the device. 5CB was able to suppress the recombination reaction without sacrificing the electron injection process and in doing so improved the electron collection efficiency, which resulted in higher photocurrents. The fact that the longer alkyl chain could not penetrate deeply into the mesoporous TiO_2 means that there is a higher probability of the electrons in the TiO_2 being intercepted by the electrolyte. In addition, due to the slow ionic diffusion of the I_3^- , instead of diffusing towards the Pt electrode and being reduced to I^- , the I_3^- molecules spent more time near the surface of the TiO_2 , contributing to higher electron recombination rates.

Table 5.6 Summary of the charge resistances and electron lifetime for different LC-PEs measured at 25 °C in dark conditions.

Sample	R_s (Ω)	R_{pt} (Ω)	R_{CT} (Ω)	τ_e (ms)
5CB	14.66	20.95	77.11	17.5
6CB	16.53	17.31	62.27	13.2
7CB	16.37	21.42	69.05	15.9
9CB	15.48	16.66	59.06	11.6
10CB	14.01	16.85	61.57	12.4

5.4 Effect of dielectric permittivity

5.4.1 Dielectric permittivities

Dielectric permittivity measurements of the different samples were also performed to study the effect of varying the dielectric permittivity of the LC mixture on the photovoltaic properties. Dielectric permittivity can be obtained by subtracting the dielectric anisotropy value of the perpendicular components of the dielectric material from the parallel components of the dielectric material. A negative dielectric LC material can be synthesised by introducing a polar group in the lateral position of the LC molecule instead of at the end (Reiffenrath et al. 1989). A high dielectric permittivity usually means that a small magnitude of \mathbf{E} is able to orientate the LC molecules.

Figure 5.13 shows the relative dielectric permittivity as a function of applied voltage for different LC materials. For pure E7, a high dielectric anisotropy of approximately 11.4 was determined from the data. This value is comparable to that obtained from other research (Costa, Altafim, and Mammana 2001). The dielectric anisotropy value (-2.24) of MLC6160 was determined using a switching curve for the case of a homeotropic cell (Figure 5.13b). As can be seen from the curves of the planar and homeotropic cells, the binary MLC6610-E7 (10:90 vol:vol) mixture showed a flat line, which means that the dielectric anisotropy was close to zero.

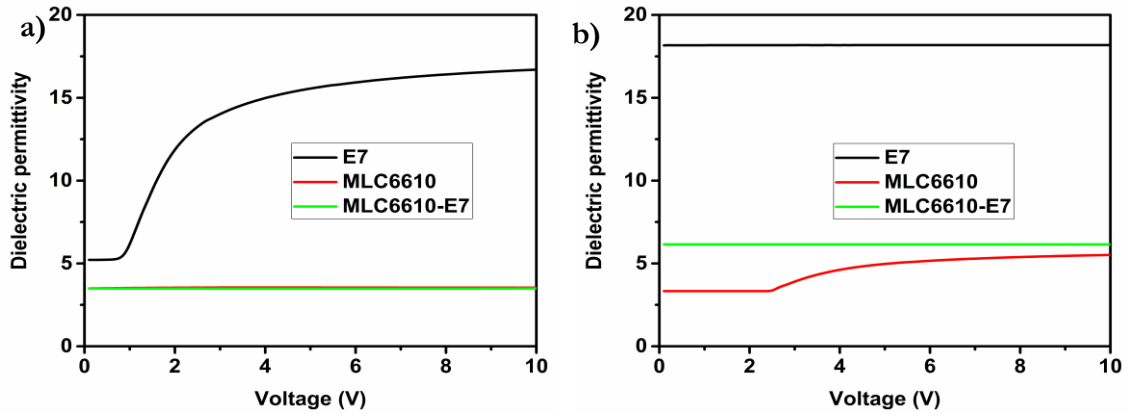
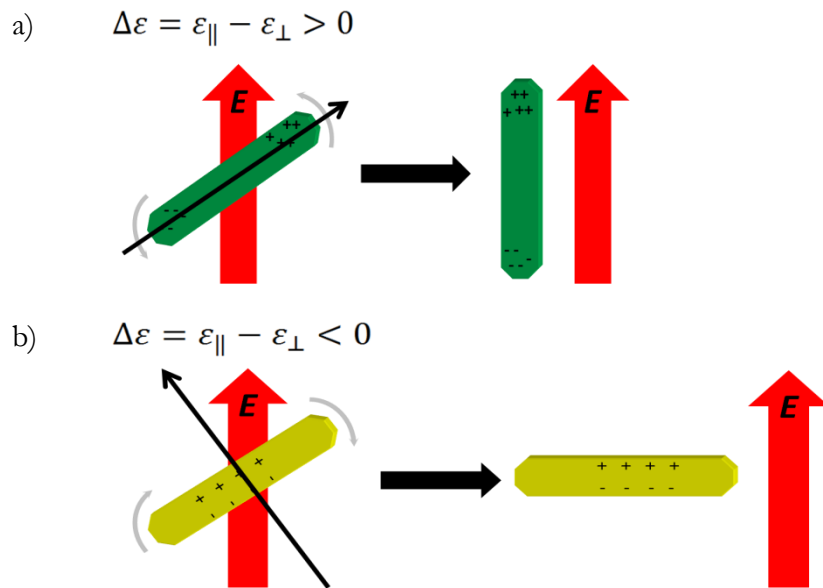


Figure 5.16 Dielectric permittivity of the different samples in a) a planar cell and b) a homeotropic cell measured at 25 °C at 1 kHz.

Figure 5.17 shows a schematic diagram of LC materials with different dielectric permittivities. For an LC material with a positive dielectric permittivity, the molecules tend to align parallel to the direction of \mathbf{E} (Figure 5.17a). Due to the presence of the polar group in the lateral position, the induced polarisation aligns the director perpendicular to \mathbf{E} (Figure 5.17b). However, in the binary LC mixture, there was no change in the dielectric permittivity in both planar and homeotropic cell (Figure 5.17c). The molecules are expected to orientate in a way such that the direction will be the average of all molecules. It might be that the LC mixture require more than 10 V to switch the direction of the molecules. It has been shown that in the case of a mixture, the orientation of the molecules will be the average orientation of all the components in the system.



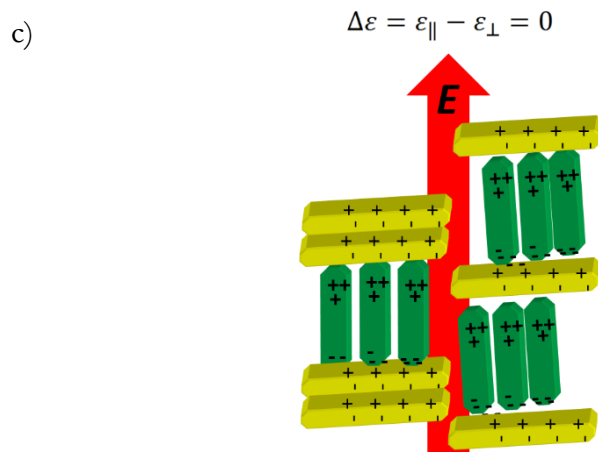


Figure 5.17 Schematic representation of a) positive dielectric permittivity LC, b) negative dielectric permittivity LC and c) nearly-zero dielectric permittivity LC under \mathbf{E} .

5.4.2 Polarising optical microscopy

The morphology of the LC-PEs was observed using POM. Figure 5.18a shows an optical micrograph of the polymer electrolyte with E7. Only dark regions can be seen in this picture, which is indicative of the amorphous nature of the polymer. Even at a higher temperature (35.0 °C), no changes were observed (assuming the changes would occur at the isotropic temperature of the LC). One reason for this is the solvency of E7 LC in acetonitrile, which reduces the effect of the long-range order of the LC molecules. Instead of behaving like a LC, the molecules behave like an isotropic liquid. Figure 5.18b) shows the POM image of the MLC6610-E7 LC mixture. Similar to the E7-only LC-PE, only dark image could be observed. This is to be expected since the E7 component makes the large portion of the mixture and thus E7 will have a major effect on the LC-PE. However, in the case of MLC6610-only polymer electrolyte, formation of microdroplets dispersed throughout the polymer, as can be seen in Figure 5.18c). This shows that acetonitrile is an orthogonal solvent for MLC6610. These micro-droplets are uniform in size (5 - 10 μm) and show a radial configuration where the director of the LCs is along the perimeter of the droplets and a point defect is in the middle of the droplets. When the temperature was increased (32.5 °C), these droplets started to disappear. Only those of larger sizes remained up to 40.0 °C (inset of Figure 5.18c).

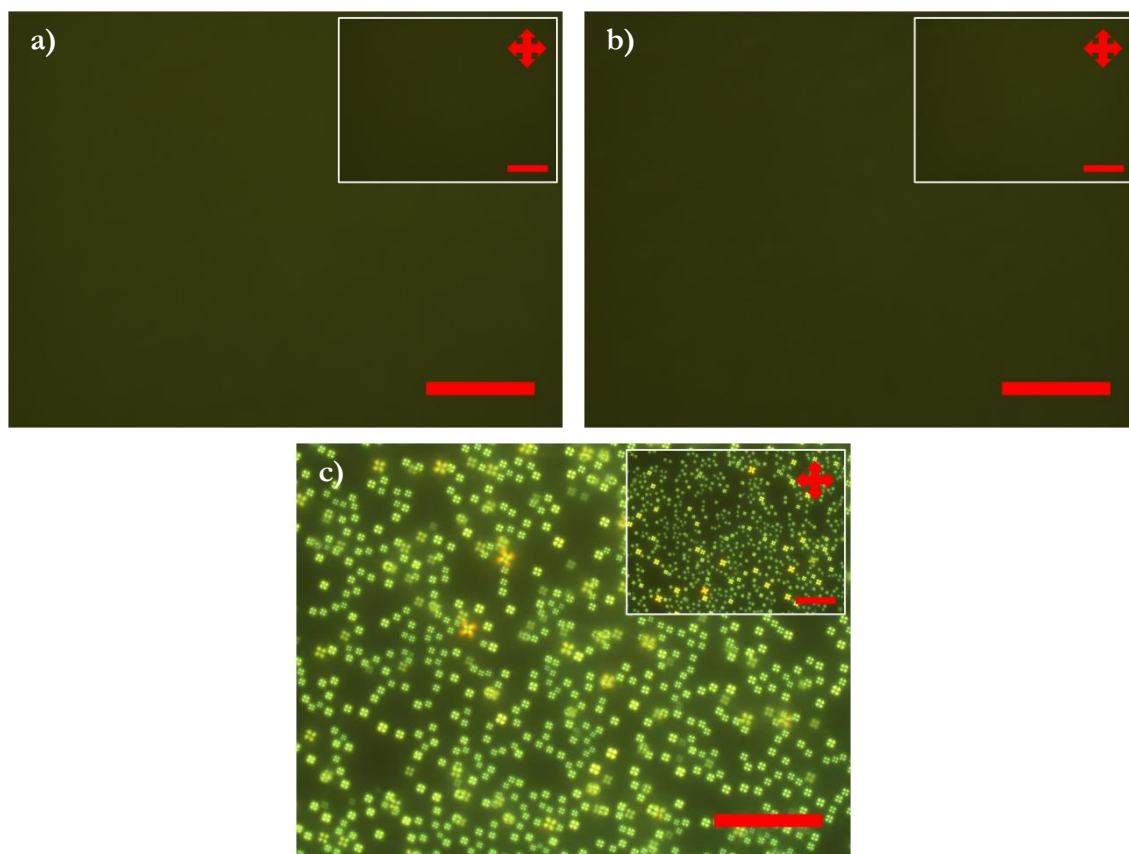


Figure 5.18 POM micrographs of capillary filled LC-PEs in a 9 μm ITO cell configuration recorded under crossed polarisers observed at 25 °C. Texture of polymer electrolyte with a) E7, b) MLC6610-E7 binary mixture and c) ML6610. The inset images are at 40 °C. The scale bar is 50 μm .

5.4.3 Current-voltage measurement

I - V measurements were performed to measure the ionic conductivity, particularly, to probe the effect of different dielectric permittivities on the ionic conductivities of the LC-PEs. Figure 5.19 shows a) a conductivity plot and b) an Arrhenius plot for the different polymer electrolytes.

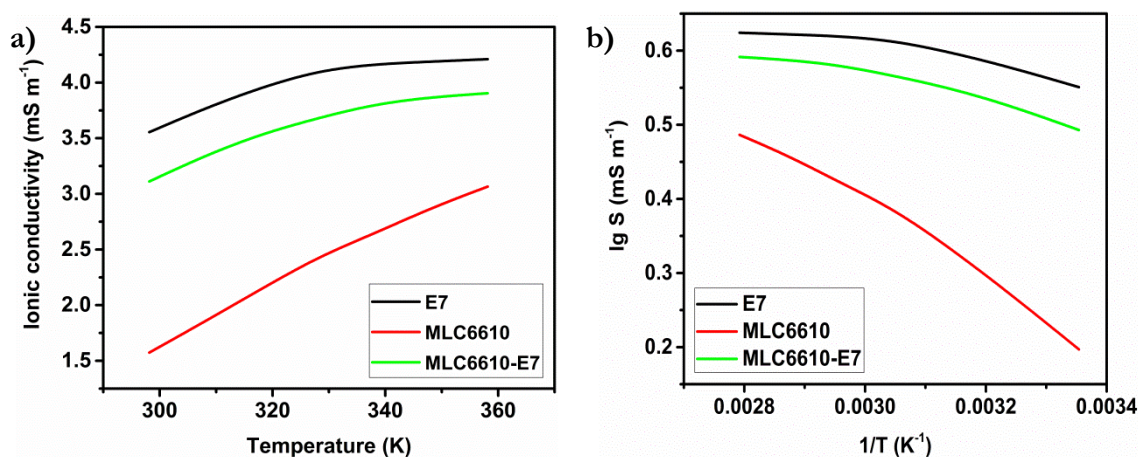


Figure 5.19 a) Ionic conductivity as a function of temperature measured at 25 °C at 1 kHz and b) Arrhenius plot of the ionic conductivity in a 25 μm ITO-ITO cell.

The highest ionic conductivity was achieved with a polymer electrolyte employing E7 ($3.55 \times 10^{-3} \text{ S m}^{-1}$), followed by MLC6610-E7 ($3.11 \times 10^{-3} \text{ S m}^{-1}$). The lowest ionic conductivity obtained with a polymer employing MLC6610 ($1.57 \times 10^{-3} \text{ S m}^{-1}$). Figure 4a shows the ionic conductivity of the polymer electrolytes as a function of temperature. The increase in the ionic conductivity with increased temperature is a well-observed phenomenon for polymer electrolytes. However, the obtained Arrhenius plot shows a different characteristic whereby the plot is not linear with respect to the temperature but shows a curve. This can be explained using the VTF equation (Equation 5.4) where the curvature of the plot is due to the segmental motion of the polymer which improves the inter- and intra- hopping of the ions instead of just intermolecular ion hopping in the case of liquid electrolyte. The higher ionic conductivity of the E7 sample can be explained by the dissolving nature of the molecules, which improved the flow of the ionic components and reduced the glass transition temperature of the polymer matrix. Similar to the case of n-alkyl cyanobiphenyl LCs, the presence of cyano groups in the E7 liquid crystal mixture contributed to a more efficient ionic dissociation through Lewis acid-base interaction. The lower ionic conductivity of the MLC6610-E7 mixture and the pure MLC6610 can be attributed to the non-dissolving nature of LCs in acetonitrile which hindered the movement of free ions within the polymer system.

It has been reported that higher dielectric permittivity leads to higher ionic conductivity (Schroder, Haberler, and Steinhäuser 2008; Shim and Kim 2008). As discussed earlier, a higher dielectric permittivity material allows the orientation of charge particles to be easily polarised. This in turn helps to localise the ions and leads to higher ionic conductivity.

However, with the addition of MLC6610, the ionic conductivity showed a lower value. This can be related to the way the molecules aligned themselves within the system. Because the LC formed droplets within the polymer the mobile ions were hindered by the LC molecules instead of allowing the ions to move from one electrode to the other. The voltage applied is not high enough to displace the ions. In addition, the presence of the LCs in isotropic phase in the polymer is expected to help reduce the viscosity of the polymer electrolyte, thus allowing greater ionic mobility. It is also postulated that the switching effect of the LC molecules due to internal E also aids the dissociation of the ionic salts and therefore helps to increase ionic conductivity. A similar observation was made by Osman *et. al.* (Osman, Ibrahim, and Arof 2001).

5.4.4 Photovoltaic properties

Subsequently, DSSCs were fabricated using the three different polymer electrolytes, and were tested under AM 1.5 conditions. The $J-V$ curves and a summary of the efficiencies of the DSSCs prepared with the different LCs are shown in Figure 5.20a and Table 2, respectively. The highest efficiency was obtained with the DSSC employing E7 (4.00 %), followed by the DSSC employing MLC6610-E7 (3.71 %) and the DSSC employing MLC6610 (3.08 %). Although the J_{sc} was comparable for all three cases, a marked difference can be seen in the V_{oc} and FF . The V_{oc} is related to the difference between the quasi-Fermi level of TiO_2 and the redox potential of the polymer electrolyte. As explained in the POM studies, E7 LC dissolves in acetonitrile, whereas MLC6610-due to the orthogonal nature of the solvent-remains as microdroplets throughout the polymer. The presence of the cyano-group in the LC molecules allows them to adsorb onto a TiO_2 surface through the lone pair (Koh et al. 2013). It is hypothesised that, the conduction band of the semiconductor is up-shifted in the case of E7, increasing the difference between the Fermi level and the redox potential and thus increasing the V_{oc} . Another reason for this high V_{oc} in the case of E7 is the lower energy needed to separate the positively and negatively-charged particles due to the high dielectric permittivity provided by the LC material (Chen et al. 2014). The high solar conversion efficiency of E7 and MLC6610 also contributes to the high ionic conductivity as shown previously. It can also be hypothesised that the MLC6610, due to its tendency to form droplets, decreases the catalytic sites of the I^-/I_3^- redox couple on the Pt electrode which leads to lower efficiency.

Table 5.7 Photovoltaic performance of DSSCs based on the three different polymer electrolytes measured at 25 °C under 1 sun illumination.

Device	J_{sc} (mA cm ⁻²)	V_{oc} (V)	FF (%)	η (%)
E7	8.99	0.73	61.27	4.00
MLC6610-E7	8.77	0.68	62.10	3.71
MLC6610	9.00	0.67	51.21	3.08

Figure 5.20b shows the dark J - V characteristics of the different types of solar devices. The onset of the dark current gives information on the electron recombination reaction at the TiO₂ surface. The onset for MLC6610 is several mV lower than that of MLC6610-E7, and E7 shows that the recombination reaction is larger in MLC6610. This suggests that the addition of E7 reduces the number of electrons in the TiO₂ being intercepted by the polymer electrolyte. This corroborates the previous hypothesis that the E7 molecules adsorb onto the TiO₂ surface.

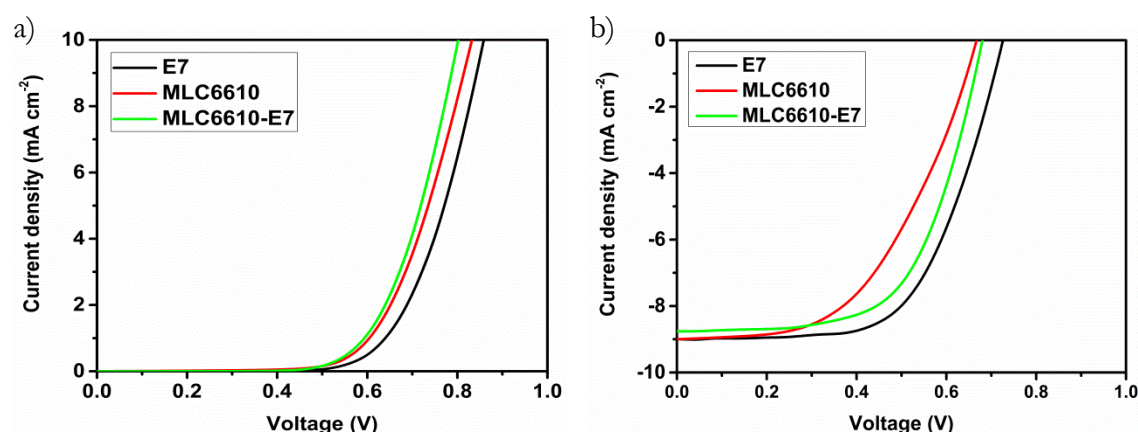


Figure 5.20 J - V curves of the photovoltaic devices fabricated with LC-PEs under a) dark conditions and b) 1 sun illumination at 25 °C.

5.4.5 Electrochemical impedance spectroscopy

Figure 5.21 shows the a) Nyquist plot and b) the Bode plot of the devices measured under dark conditions at an applied bias of -0.70 V. Three semicircles can be seen in the Nyquist plot for a typical liquid electrolyte DSSC. However, in this experiment the semicircles overlap each other, pointing toward the high charge transfer resistance in the device. The interception of the plot on the x -axis at high frequencies can be attributed to the sheet resistance of the counter electrode, R_s . It can be seen that R_s is similar across all devices because the FTO

substrates have similar sheet resistance. E7 showed the lowest R_{Pt} , followed by MLC6610 and MLC6610-E7. In the case of E7, the LC molecules are evenly dispersed throughout the polymer electrolyte, the Pt surface are free to transfer electron from the FTO substrate to reduce I_3^- . In the case of MLC6610-only LC-PE, the LC formed microdroplets, it is hypothesised that the droplets also covered the Pt surface which means that the catalytic reaction surface is reduced and thus higher resistance was observed. Regarding the MLC6610-E7 mixture, because there are MLC6610 molecules within the polymer electrolyte system, the insolvency nature of the molecules also affected the polymer electrolyte as we have seen in the case of MLC6610-only LC-PE. This is evident from the higher R_{Pt} when compared with E7-only LC-PE.

Table 5.8 Summary of EIS parameters for DSSCs incorporating LCs with different dielectric anisotropies measured at 25 °C in dark condition.

Device	R_s (Ω)	R_{Pt} (Ω)	R_{CT} (Ω)	τ_e (ms)
E7	18.5	11.4	42.6	11.9
MLC6610	17.3	19.1	43.1	6.9
MLC6610-E7	17.9	23.0	62.5	14.9

The electron lifetime can be calculated from the Bode plot using Equation 5.2. The electron lifetime is related to the back reaction between the injected electron from the dye and the recombination reaction with the electrolyte instead of being transported into the system. E7 and the MLC6610-E7 mixture showed higher τ_e compared to MLC6610. As a result of the formation of LC droplets within the polymer system, MLC6610 molecules were not adsorbed on the TiO_2 and thus a higher recombination loss was expected. For the MLC6610-E7 mixture, however, some of the E7 molecules were still available to passivate the oxide semiconductor surface.

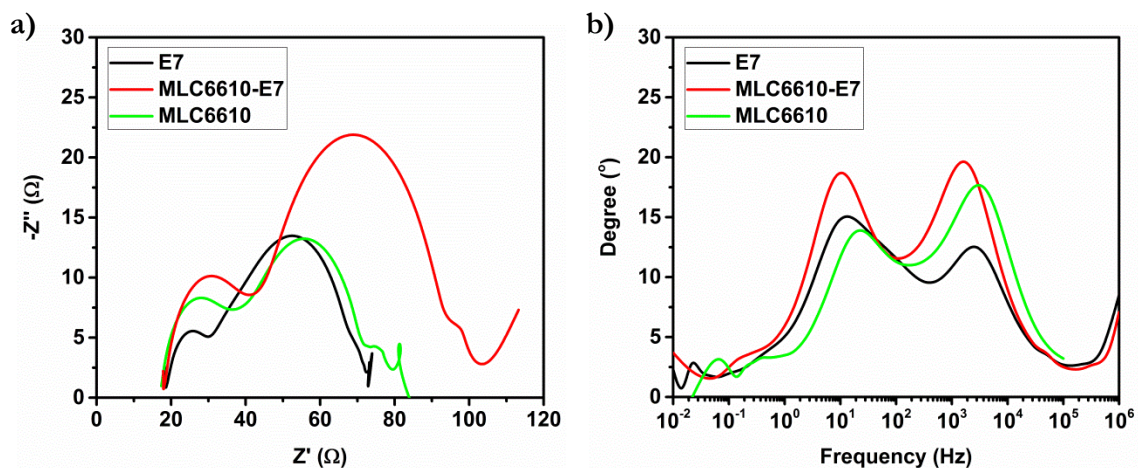


Figure 5.21 Nyquist plot and b) Bode plot of the photovoltaic devices fabricated with LC-PEs measured at 25 °C in dark conditions.

5.5 Summary

In this chapter, different types of LC-PEs were prepared and characterised. In the first section, we showed that conductivity can be increased by changing the doping concentration of 5CB in the polymer electrolyte. These LC-PEs showed better performance than for a pure polymer electrolyte with increased J_{sc} . This is thought to be because the LC improved the dissociation contributed by the cyano group. In addition, due to the birefringence of the LCs, they scattered light passing through the sample, allowing the light to spend more time within the device instead of being passed through the cell. This has been corroborated by the light scattering experiment. From the impedance spectroscopy, we can also conclude that the charge recombination was suppressed in the LC-PEs by reducing the contact between the TiO_2 and the I^-/I_3^- redox couple.

LC-PEs with varying LC alkyl chain lengths were also prepared and characterised. Using POM and DSC studies, it was found that the LCs in the LC-PEs exist in an isotropic phase at room temperature, which means that the LCs dissolved readily in acetonitrile. Interestingly, in the case of 9CB and 10CB, which exhibits the SmA phase, isotropic droplets in the polymer electrolyte were observed. This strongly suggests that the morphology is strongly affected by the chemical structure of the LCs. Electrical and electrochemical characterisations were also performed for the LC-PEs where the ionic conductivity was inversely proportional to the alkyl chain length. This is because longer alkyl chains are intertwined between neighbouring chains and trap mobile ions. Longer alkyl chains have also

been observed to increase the total viscosity of the polymer system and have been established to reduce ionic conductivity with increasing viscosity. When these LC-PEs are incorporated into DSSCs, it has generally been observed that increasing the alkyl chain length reduces the photovoltaic parameters. The highest obtained efficiency was obtained with 5CB where $\eta = 3.36\%$ and showed a decreasing trend with longer alkyl chains. The lowest performing device was obtained with the 10CB sample with $\eta = 2.06\%$. The decrease in the performance, particularly the J_{sc} and V_{oc} , can be explained by the decrease in the measured ionic conductivity of the LC-PEs with increasing LC alkyl chain length and the dynamics of the LC molecules in the polymer electrolyte system inside DSSCs. The results of the EIS measurements corroborate our hypothesis that in the case of longer alkyl chain LCs, the resulting geometry is unfavourable for adsorption onto TiO_2 and at the same time hinders the movement of ionic species within the polymer electrolyte. This is evidenced by the measured low electron lifetime for longer alkyl chain systems. Another issue to note is that the charge transfer resistances are not the only governing parameters for DSSCs. The efficiency of DSSCs also depend on, for example, the ionic conductivity of the electrolyte, light scattering within the device and the absorption spectrum of the dye.

Finally, LC-PEs were fabricated with LCs having different dielectric anisotropies ranging from positive, zero and negative value. The highest power conversion efficiency was realised with E7 where an efficiency of 4.00% was achieved. This is followed by the device employing the binary MLC6610-E7 mixture with 3.71% efficiency. The lowest efficiency of 3.08% was obtained with MLC6610. The solvency nature of E7 in acetonitrile is thought to be the reason for the high efficiency value. E7 helped to improve ionic conduction provided switching of the molecules by the \mathbf{E} due to their high $\Delta\epsilon$. The switching of the molecules from one orientation to another can also lead to the dissociation of the ionic salts which can increase the ionic conductivity. The tendency of the MLC6610 forming LC droplets led to lower ionic conductivity as this hinder the movement of the charged particles.

Chapter 6 Liquid crystalline templates

6.1 Foreword

In Chapter 4, the addition of positive $\Delta\epsilon$ LC material with short alkyl chains was found to be beneficial for the performance of the DSSCs. The addition of LC into the polymer electrolyte was found to increase the ionic conductivity and thus the efficiency of the solar devices. This was also due to the improved light scattering effect and the passivation of the TiO_2 surface. The use of material having large $\Delta\epsilon$ allowed it to be switched, thus improving the ion solvation in the polymer electrolyte. LC materials with shorter alkyl chains have also been demonstrated to improve the ionic conductivity of the LC-PEs rather than hindering the ionic movement due to the intertwining of the alkyl chains. However, DSC and POM studies showed that the LCs were in the isotropic phase.

As noted previously, one of the interesting aspects of LC materials is their ability to self-assemble. This is achieved through internal weak interactions within the molecules to create complex structures. The typical methods to control these weak interactions are the use of a variety of different molecular compounds able to form phase-segregated structures. The self-assembly of LCs is achieved naturally, either due to hydrogen bonding or π - π stacking of the molecules (Kato 2002; Pouzet et al. 2009). These add functionality to the original material. In addition to self-assembly, LC materials also respond to the application of external electric or magnetic fields due to the presence of a polar group (Blinov and Chigrinov 1994). A polar group causes the polarisation of molecules, which allows alignment of the molecules in response to the applied field. In addition, the morphology of LCs can also be controlled using a thin alignment layer (Berreman 1973). A thin layer of polymer that has been rubbed in one direction is employed where the LC molecules align in the grooves produced by the rubbing action. By taking full advantage of this effect, it is possible to control the structure of LCs to suit particular applications. These characteristics allows researchers to manipulate the LC mesophase for use in a wide range of applications including displays, lasers and solar cells (Coles and Morris 2010; Fergason 1973; Zheng et al. 2011).

In organic electronics, controlling the morphology and structure of organic compounds is essential in realising high-efficiency devices such as organic field effect transistors and organic solar cells (Park et al. 2007). The idea in controlling the morphology is to improve

the interfacial area between the electron donor and acceptor for efficient exciton dissociations, as in the case of organic solar cells. Some of the methods employed to control the morphology and molecular packing include thermal and solvent annealing and choice of the solvents and additives (Chen et al. 2014; Liao et al. 2013; Shi et al. 2015; Yi et al. 2014). Cho et al. showed the transition of the morphology of the polyelectrolyte from nano-porous to micro-porous after applying E (Cho et al. 2013).

Smectic LCs are interesting materials that have higher-order parameters compared to nematic LCs. In an application such as a template, this means that the smectic LCs can exert greater influence over the morphology of the materials to be synthesised. The synthesised materials are expected to replicate the structure of the smectic LCs, which are in range of a few nanometres. In this study, we began by preparing different mixtures of NLCs and SmAs to find the optimum ratio to obtain a highly ordered polygonal structure. The addition of a reactive mesogen and a photoinitiator to the optimised mixture did not alter the structure. In fact, upon UV polymerisation and subsequently upon removing the LC components, it was found that the polymerised reactive mesogen conformed to the structure of the initial LC mixture. The morphology of these LC-templated materials was related to their electrical and electrochemical properties. Potential application of these templated materials through the fabrication and characterisation of DSSCs. As an extension of the idea of self-assembled LC-templated material, we used applied E and a PI alignment layer to control the structure of the LC mixture and compared it with the self-assembled template. This work will allow a better understanding of the interaction between LCs and external conditions.

6.2 Highly ordered polymer template using an optimised NLC:SmA binary mixture

6.2.1 Preparation of optimised NLC:SmA binary mixture

Binary mixtures of 8/2 organosiloxane and E7 were prepared with varying weight percent (wt.%). Figure 6.1a shows the DSC curves of binary LC mixtures of a nematic (N) E7 and an 8/2 organosiloxane LC. The transition temperature for pure E7 from N to isotropic (I) is 58.3 °C. The 8/2 organosiloxane showed a SmA phase within the temperature range of 43.6 °C to 62.9 °C and is crystalline (Cr) at room temperature in its native form. The addition of 20 wt.% of 8/2 to E7 increased the SmA to an I transition temperature up to 64.3 °C, which is the highest obtained transition temperature for pure materials and binary mixtures.

A further increase in the E7 composition, however, resulted in a comparatively lower transition temperature. The lowest transition temperature was displayed by the 8/2:E7 20:80 mixture at 50.6 °C. From the DSC study, it is evident that the mixtures were homogenous. If this was not the case (in other words, the mixtures were phase separated), it would be expected that the transition temperature of the pure materials could be seen instead of just one transition. To obtain a clear picture of the different LC phases of the LC mixtures, a phase diagram was plotted (Figure 6.1b). The measurement of the transition temperature was limited by the DSC equipment, and measurement below 0 °C could not be obtained. The addition of 8/2 organosiloxane to E7 changed the mesophase drastically where only the smectic phase could be achieved. The mesophase is thought to be dependent on the larger size of the LC component and in this case, the phase of the binary mixture was induced by the 8/2 organosiloxane where the size of the molecule was several times larger than E7. The effect of the LC length on the mesophase of a binary LC mixture has been studied previously (Kapernaum et al. 2012). Not only was the transition temperature the highest for 8/2:E7 20:80 mixture, but it also had a wider SmA temperature range compared to the pure 8/2 organosiloxane and other binary mixtures.

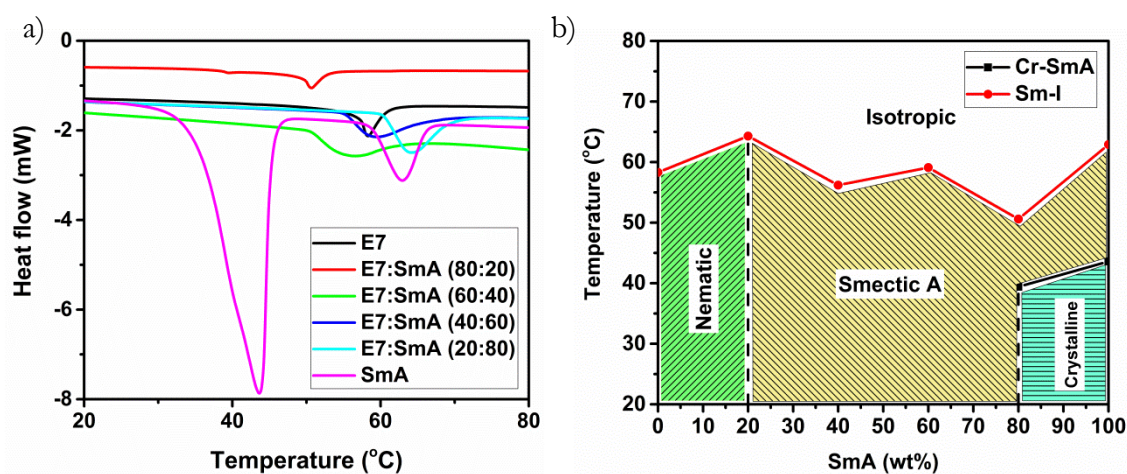
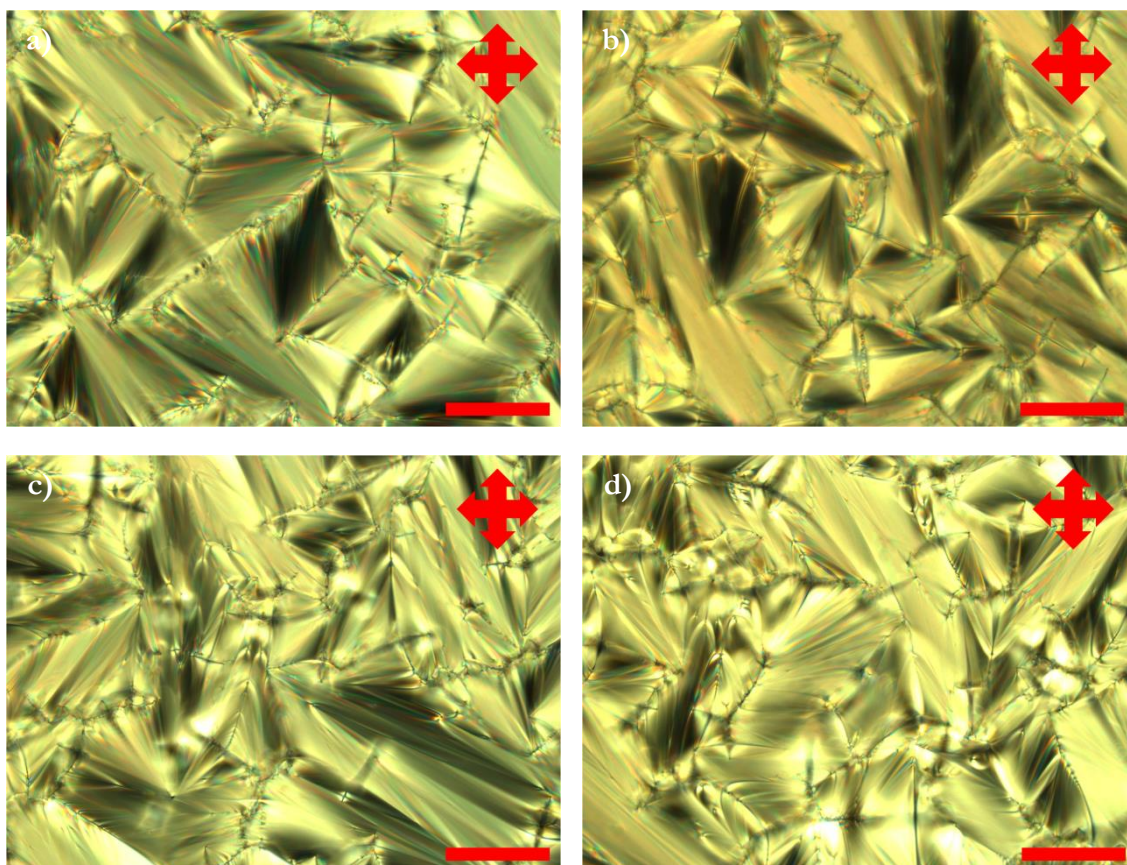


Figure 6.1 a) DSC curves under heating at 5 °C min⁻¹ and b) phase diagram of pure LC materials and binary LC mixtures at different 8/2:E7 ratios.

Figure 6.2 shows the morphology of the LC materials either in pure form or in mixtures in their LC phase. The SmA phase is characterised by a fan-shaped structure made up of focal conics (Figure 6.2a). This is formed from the lamellae structure where the smectic layers are parallel to the substrate's plane. However, E7 showed a Schlieren texture which is typical for NLCs (Figure 6.2f). A polygonal structure could be seen in the 8/2:E7 20:80 mixture (Figure

6.2e). This is a result of the disinclination of the lamellae perpendicular to the plane of the glass substrates, which induced the focal ellipses lying in the plane. The tip of the focal section affixed to the opposite substrates. This type of texture can only be seen in the 8/2:E7 20:80 mixture. Beyond the 20 wt.% concentration of 8/2 organosiloxane, all the mixtures showed the typical SmA texture (Figures 6.2d-f). It was found that the optimum ratio of 8/2 organosiloxane to E7 was 20:80, as this mixture gave a micro-structure that was aligned out-of plane instead of lying on the plane of the substrate and thus a higher degree of order. This result is supported by the DSC thermogram where 8/2:E7 20:80 showed the highest transition temperature among the other mixtures. Therefore, this mixture was chosen as the template for the electrolyte to be used in DSSC fabrication. Figure 6.2g shows the corresponding schematic diagram of the polygonal structure of the 8/2:E7 20:80 mixture.



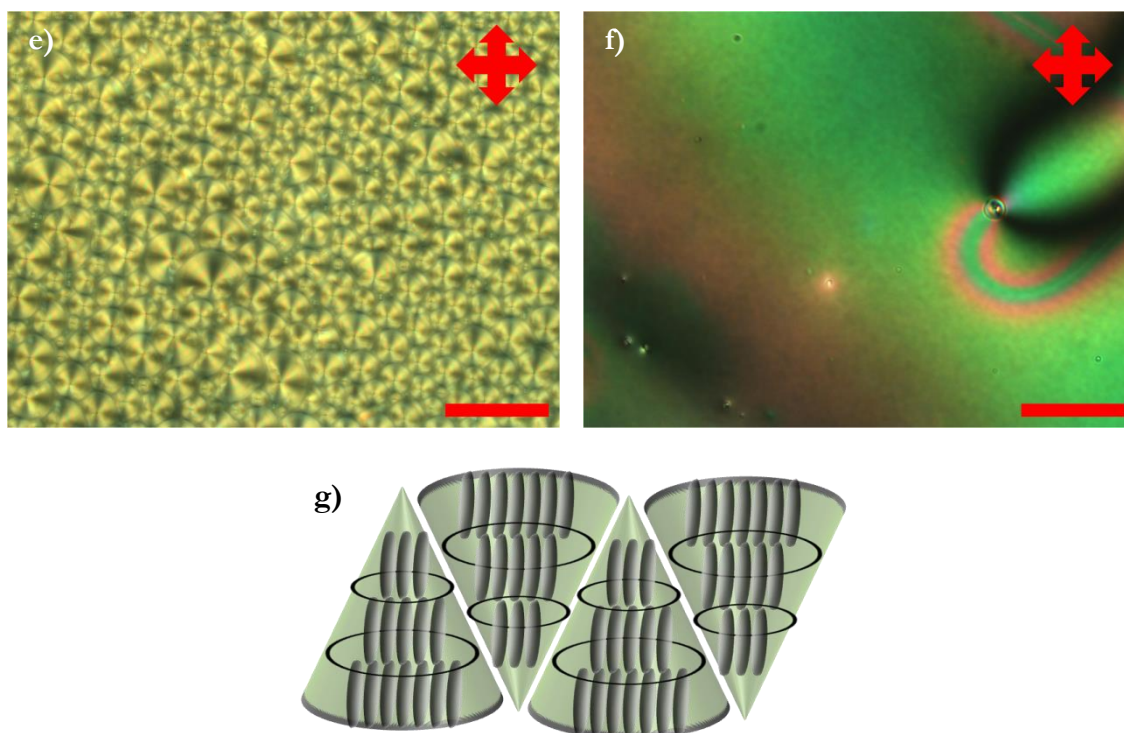


Figure 6.2 POM micrographs of the LC mixture at different 8/2:E7 ratios under crossed polarisers observed at 25 °C. All pictures were taken at the LC phase after cooling down from isotropic phase (80 °C) at a rate of 5 °C min⁻¹. a) 100:0, b) 80:20, c) 60:40, d) 40:60, e) 20: 80 and f) 0:100. g) Schematic diagram of the polygonal structure formed by the binary LC mixture (side view). The scale bar is 50 μm.

6.2.2 Preparation of LC template

To form stabilised micro-structures, a polymerisation step is required. This was achieved through the addition of LC monomer RM 257 to the original binary mixtures. No change in the texture of the mixture was observed after the addition of RM 257 and IR 819, showing the stability of the polygonal structure. The morphology of the mixture before polymerisation (Figure 6.3a) and after polymerisation (Figure 6.3b) changed slightly in that the polygonal structures were not as homogenous in size as before, indicating that the addition of RM 257 and IR819 disrupted the order of the polygonal structure. The reactive mesogen was successfully templated using the binary mixture, as seen from Figure 6.3a and Figure 6.3b, instead of showing the spherulite structure of RM 257 (Figure 6.3e). The LC component was then removed using acetone to leave polymerised micro-channels (Figure 6.3c). After removal of the LC constituents, the textures showed hollow inter-connected channels (Figure 6.3d). This shows that the reactive mesogen was templated using the binary

LC mixture. It is postulated that the I^- -based liquid electrolyte ions travelled through these micro-channels. Filling the cell with the liquid electrolyte (Figure 6.3d) preserved the same structure, which means that the template is stable with regards to acetonitrile. This smectic-templated polymer electrolyte (Sm-PE) gives out a yellow colour that derives from the iodine in the electrolyte.

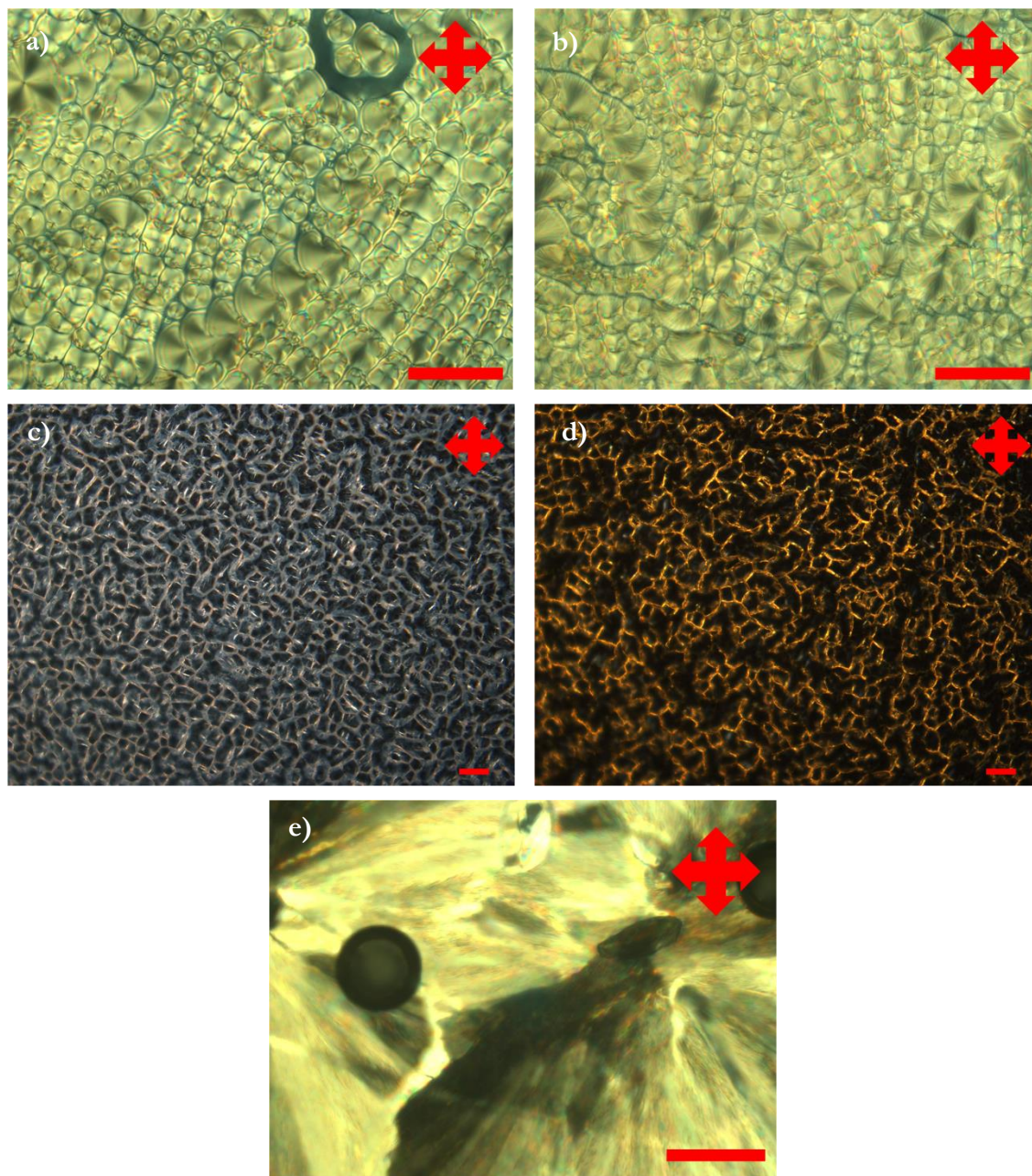


Figure 6.3 POM micrographs of the SmA:E7 mixture with RM 257 and IR 819 under crossed polarisers at 25 °C. The cell is filled in the isotropic state and is allowed to cool down naturally before characterisation. a) Before polymerisation, b) after polymerisation, c) after the

removal of LCs, d) after infiltration with liquid electrolyte and e) pure RM 257. The scale bar is 50 μm .

6.2.3 Fourier-transform infrared spectroscopy

FTIR spectroscopy was performed for different materials to study the interaction between different molecules and the changes after UV polymerisation. The absorption corresponding to the nitrile group was approximately 2200 cm^{-1} , which was present in E7, 8/2 organosiloxane and the binary LC mixtures. Figure 6 shows the FTIR curves for the different pure materials and mixtures. It can be clearly seen that this peak has disappeared after the removal of the LC components, showing that acetone removed the LCs and left only polymerised RM 257. The peak at 1700 cm^{-1} originates shows the C=O stretching coming from RM 257. This peak still existed even after immersing the sample in acetone which proves that acetone only removed the LCs. Figure 6.4 shows the FTIR spectra for the LC material, the mixture before/after UV polymerisation and after immersion in acetone.

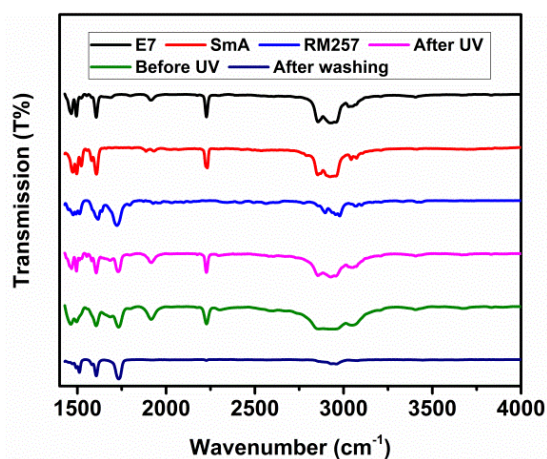


Figure 6.4 FTIR spectra of the different components of the pure E7, 8/2 organosiloxane, RM 257, the binary mixtures before and after UV curing and after the removal of the LC components characterised at 25 °C.

6.2.4 Morphology and structure characterisation

SEM micrographs allow for a more precise view of the polymerised mixture after removal of the LC components (Figure 6.5a). As can be seen from the micrograph, the formation of micro-sized pores could be observed throughout the sample. These hollow structures are postulated to be provide ordered pathways for mobile ions to move and at the same time have the ability to trap liquid electrolyte, thus extending the lifetime of the polymer electrolyte by suppressing evaporation of the solvent. The width of the polymer fibres was estimated to

be around 50 nm. The polymer had a thread-like structure where two or more polymer fibres intertwined. It was also found that the surface roughness was considerably high. This was to be expected as the UV polymerisation of the sample was done on a cell. The process of removing the top and bottom substrate might have led to the uneven surface, despite the use of PVA as the sacrificial layer. Another characteristic to note is the formation of a bigger thread-like structure formed by different single fibres. These intertwined thread-like structures formed boundaries resulting in the configuration of the micron-sized pores, as seen on the POM image. An AFM study was also performed on the same sample. The AFM micrograph (Figure 6.5b) corresponds well with the SEM image on which the formation of helical structures could be seen. The width of the polymer is also estimated to be approximately 50 nm which is in good agreement with the SEM image. In addition, it can be seen that the surface of the template is not smooth, but in fact displays surface variations of approximately 1 μm .

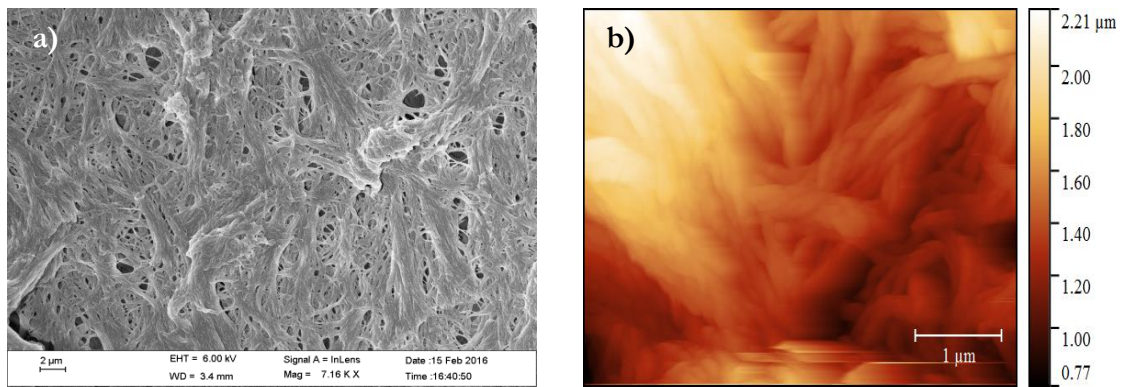


Figure 6.5 a) SEM image of LC-templated polymer with a thin layer of chromium/gold sputtered onto the sample to reduce the charge build-up during characterisation. b) AFM image of the LC-templated polymer prepared on a silicon substrate.

6.2.5 Current-voltage measurements

The ionic diffusion constant of the mobile ions in the template electrolyte was measured using a standard current density-limited method using a steady-state voltammogram. The diffusion coefficient can be calculated using Equation 5.1. From the measurement, it was calculated that the $D_{I_3^-}$ of liquid electrolyte is $2.59 \times 10^{-6} \text{ cm}^2 \text{ s}^{-1}$, and the Sm-PE showed $D_{I_3^-}$ of $4.53 \times 10^{-6} \text{ cm}^2 \text{ s}^{-1}$. The increased $D_{I_3^-}$ in the case of Sm-PE can be related to the improved motion of the ions in the highly ordered micro-structure that provided a more efficient pathway for the movement of the mobile ions instead of moving randomly. The presence of

a polymer network can also be thought of as barrier for the mobile ions to recombine with each other to form a tightly bound compound that effectively reduce the ion diffusion. Figure 6.6 shows the steady-state voltammetry measurement for different electrolytes.

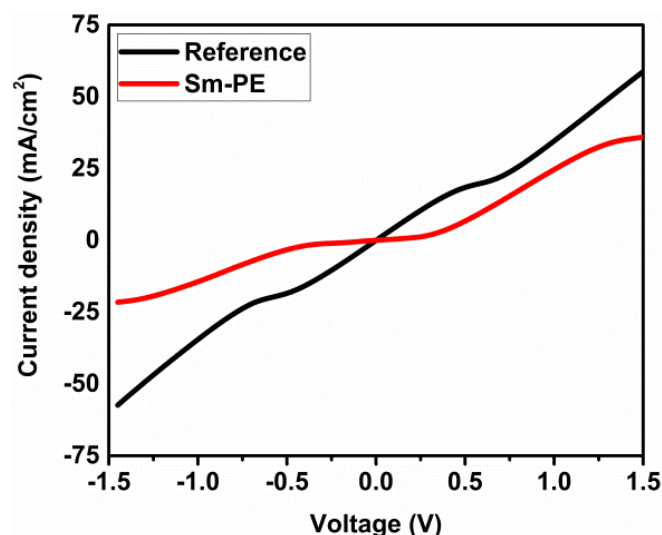


Figure 6.6 Steady-state voltammetry curve of the reference electrolyte and Sm-PE measured at 25 °C in a symmetrical ITO-ITO cell (25 μm).

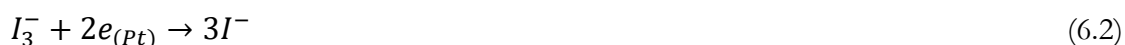
Current-voltage measurements were performed to measure the ionic conductivity in a 25 μm ITO-ITO cell. The measurements were performed at room temperature. The ionic conductivity of the templated Sm-PE was higher than that of the reference electrolyte by almost 2-fold, showing $1.47 \times 10^{-3} \text{ S m}^{-1}$. It has been shown that the ionic conduction mechanism in polyethylene oxide is via the coordination process of lithium ions induced by the segmental motion of the polymer backbone. The ions, either individually or in clusters, move along the same chain or a different chain via a hopping mechanism due to the formation and breaking of the Li-O bonds present in the polymer (Xue, He, and Xie 2015). This clearly strengthens the assumption that the channels help to increase the ionic conduction through a more ordered ionic hopping process as the polymer itself is an insulator rather than through electronic conduction. A similar observation was made by Majewski *et al.*, who measured higher ionic conductivity in the case of an LC polymer electrolyte structure prepared perpendicular to the two electrodes (Majewski et al. 2010). Since the ion transport mechanism in the polymer electrolyte involves the percolation of the mobile ions between boundary zones, a mesoporous insulating network will force the particles to touch or come close to each other so their space-charge zones overlap (Maekawa

et al. 2004). This enhances the space-charge effect and thus the ionic conductivity. Table 6.1 summarises the ionic conductivity and ionic diffusion for different electrolytes.

Table 6.9 Ionic conductivity data for the reference liquid electrolyte and the electrolyte prepared using reactive mesogen measured at 25 °C at 1 kHz in a 25 µm ITO-ITO cell.

Sample	Ionic diffusion (cm ² s ⁻¹)	Ionic conductivity (S m ⁻¹)
Liquid electrolyte	2.59 x 10 ⁻⁶	7.70 x 10 ⁻⁴
Sm-PE	4.53 x 10 ⁻⁶	1.47 x 10 ⁻³

The function of the reactive mesogen here is to act as the polymer matrix that will help to contain and aid the conduction of the liquid electrolyte. RM 257 is a known insulator and has an extremely low conductivity compared to the liquid electrolyte. The application of RM 257 has long been limited to display technology. In this case, RM 257 was used to prepare the polymer matrix, and the binary LC mixture acted as the template for the polymerisation process. The polymer itself was not involved in the electrochemical reaction of the liquid electrolyte. It is reasonable to assume that the ionic conduction occurring in the Sm-PE was the same as any other polymer electrolyte in which the segmental motion of the polymer backbones together with inter- and intra-chain ionic hopping. The redox reaction in this case remained the same as that of a standard electrolyte used.



6.2.6 Light scattering

Light propagation in a solar cell is an important factor that can affect the efficiency of solar devices, and increasing the effective propagation length of light in a solar cell serves to increase device efficiency by enhancing the optical absorption by the active medium (Franklin and Wang 2002). A light scattering experiment was performed on the two samples to investigate how light scattering varies with and without the Sm template. Figure 6.7 shows the light scattering profile of cells containing liquid electrolyte and Sm-PE electrolyte. As seen from the pictures, the light profile for the cell before filling with liquid electrolyte (Figure 6.7a) and after filling with liquid electrolyte (Figure 6.7b) is similar, implying that there was no significant increase in light scattering upon filling the optically isotropic liquid electrolyte.

However, a significant increase in scattering could be seen for the un-filled cell employing the smectic-templated polymer due to the incorporation of a birefringent porous medium inside the beam path (Figure 6.7c). On filling a liquid electrolyte into the templated polymer, the beam spread and scattering was reduced (Figure 6.7d). This is due to better refractive index matching between the liquid electrolyte and the polymer template. A previous study explored refractive index matching to control the amount of light scattering by changing the surrounding media through the incorporation of additives (Franklin and Wang 2002). Increasing the light scattering within the solar cell effectively increased the probability of the light exciting the dye molecules and hence increased the J_{sc} .

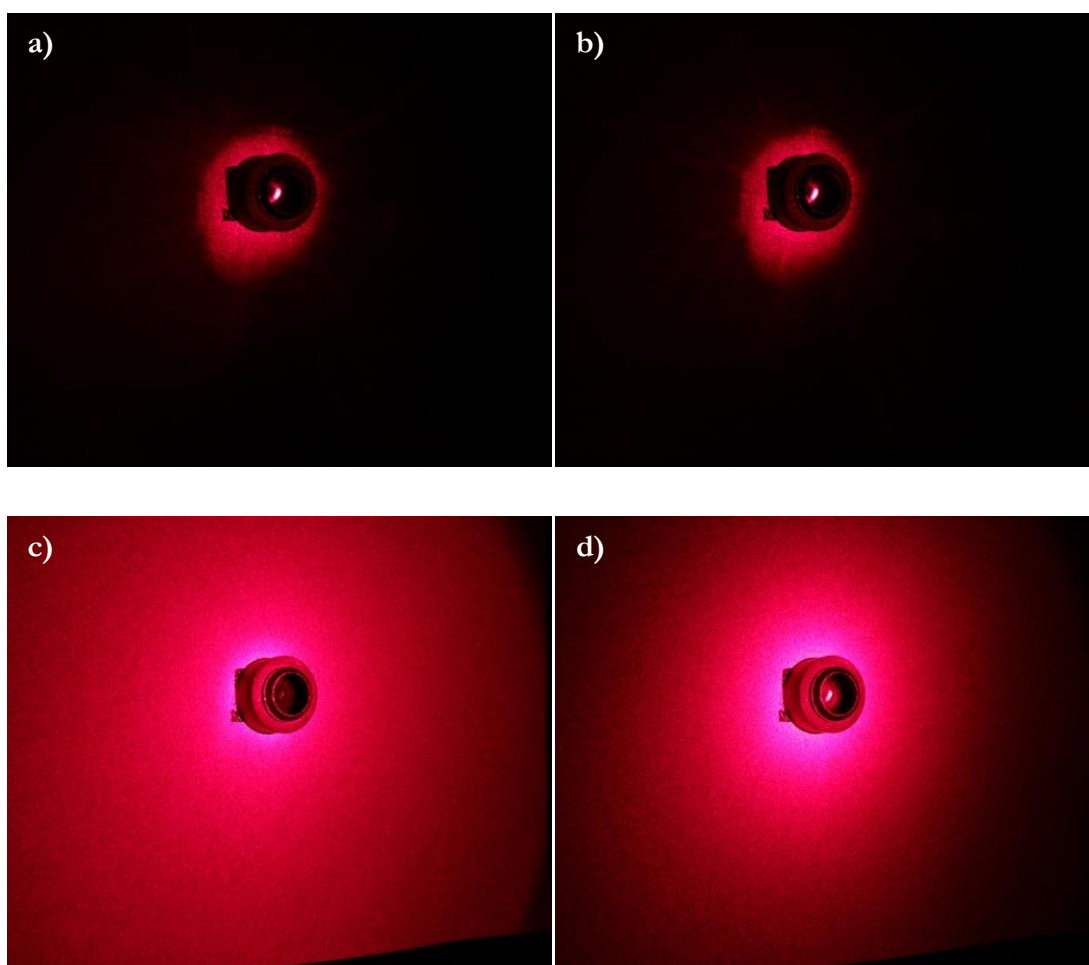


Figure 6.7 Light scattering profile of a) an empty cell, b) a cell filled with liquid electrolyte, c) an empty cell containing smectic-templated polymer and d) a cell containing Sm-PE characterised at 25 °C. The ITO-ITO cells were fabricated using 25 μm spacer film.

6.2.7 Photovoltaic properties

Subsequently, DSSCs were fabricated using the stabilised micro-channel electrolyte and were tested under AM 1.5 conditions. The J - V curves and a summary of the efficiencies of the solar cells are shown in Figure 6.8 and Table 6.2, respectively. For comparison, we compared the Sm-PE with a standard liquid electrolyte in the DSSCs. The liquid electrolyte showed a $V_{OC} = 0.688$ V, a $J_{SC} = 12.00$ mA cm⁻² and an $FF = 0.67$, corresponding to an efficiency, η , of 5.51 %. The device polymerised on the counter electrode side exhibited a $V_{OC} = 0.705$ V, a $J_{SC} = 13.25$ mA cm⁻² and an $FF = 0.63$, corresponding to η of 5.94 %.

An improvement in J_{SC} of 11 % was achieved for the Sm-PE, which can be attributed to more ordered ionic conduction pathways that enhance the ionic transport within the polymer. This is evident from the ionic conductivity data where the Sm-PE showed higher ionic conductivity. This might seem counterintuitive, as the polymer covered the surface of the Pt and thus reduced the area of catalytic reaction of Pt and I_3^- yet still gave a high photocurrent. In the case of the polymer electrolyte, the J_{SC} was lowered due to the movement of mobile ions hindered by the polymer network, but this was not the case in the polymer template electrolyte (Komiya et al. 2004). This proves that ionic conduction is aided by these nanopores in the case of the LC-templated electrolyte. The DSSC fabricated with Sm-PE also showed an increase in the V_{OC} . The reduction in the FF is attributed to the increase in the series resistance within the device.

Table 6.210 Photovoltaic performance of DSSCs based on the reference liquid electrolyte and the smectic-templated polymer electrolyte measured at 25 °C under 1 sun illumination.

Device	J_{SC} (mA cm ⁻²)	V_{OC} (V)	FF (%)	η (%)
Reference	12.00	0.69	67	5.51
Sm-PE	13.25	0.71	63	5.94

Figure 6.8a shows the dark J - V characteristics of the two different types of solar devices. The dark current gives information on the kinetics of the reaction of the electrons from mesoporous TiO₂ with I_3^- in the electrolyte. The liquid electrolyte showed an onset of dark current, which is a few mV lower than that of Sm-PE. This shows that the liquid electrolyte had a larger recombination than Sm-PE. The curve also showed an increase in the photocurrent with the increase in the voltage, suggesting the suppression of the recombination reaction with the use of the Sm-PE.

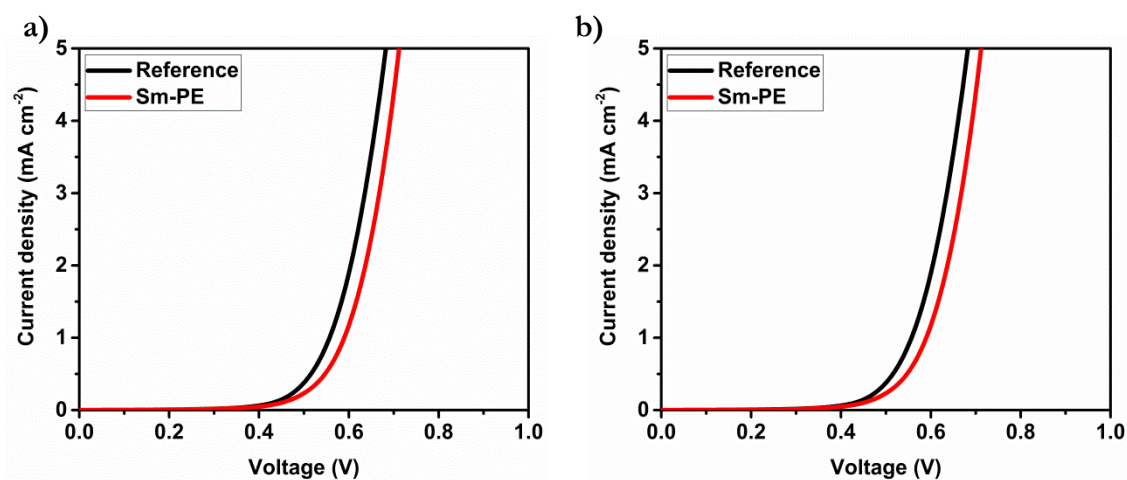


Figure 6.8 J - V curves of DSSC with reference liquid electrolyte and Sm-PE electrolyte a) in the dark conditions and b) under 1 sun illumination at 25 °C.

6.2.8 Electrochemical impedance spectroscopy

From the Nyquist plot, R_s , which is the contribution of the sheet resistance of the FTO substrate and the electrical wiring of the cell, is similar between the two devices which is to be expected. R_{Pt} is the charge transfer at the surface of the Pt electrode with the electrolyte. This is because the template, which is an insulator, was polymerised directly onto the Pt electrode and thus increased the charge resistance. The charge recombination resistance at the TiO_2 /dye/electrolyte interface is given by the R_{CT} , which can be determined from the diameter of the second semicircle. The R_{CT} is lower in the case of the reference DSSC compared to Sm-PE, which means that the electrons are more likely to be intercepted by the electrolyte. However, in the case of Sm-PE, due to the trapping effect of the electrolyte by the template, the electrons in the TiO_2 are less likely to recombine with the electrolyte. This agrees with the observation from the dark J - V curve.

Table 6.311 Summary of EIS parameters for liquid electrolyte and Sm-PE DSSCs measured in dark conditions at 25 °C.

Device	R_s (Ω)	R_{Pt} (Ω)	R_{CT} (Ω)	τ_e (ms)
Reference	18.29	2.38	42.74	11.43
Sm-PE	15.32	12.79	63.63	14.33

The electron lifetime can be calculated from the Bode plot using Equation 5.2. The electron lifetime is related to the back reaction between the injected electron from the dye and the

recombination reaction with the electrolyte instead of being transported into the system. In this experiment, the Sm-PE showed an improved electron lifetime compared to the reference liquid electrolyte DSSC, which suggests that the back reaction was impeded by the insulating polymer template. The channels can be thought as a barrier that prevents the injected electron in the TiO_2 from being intercepted by the mobile ions in the redox electrolyte.

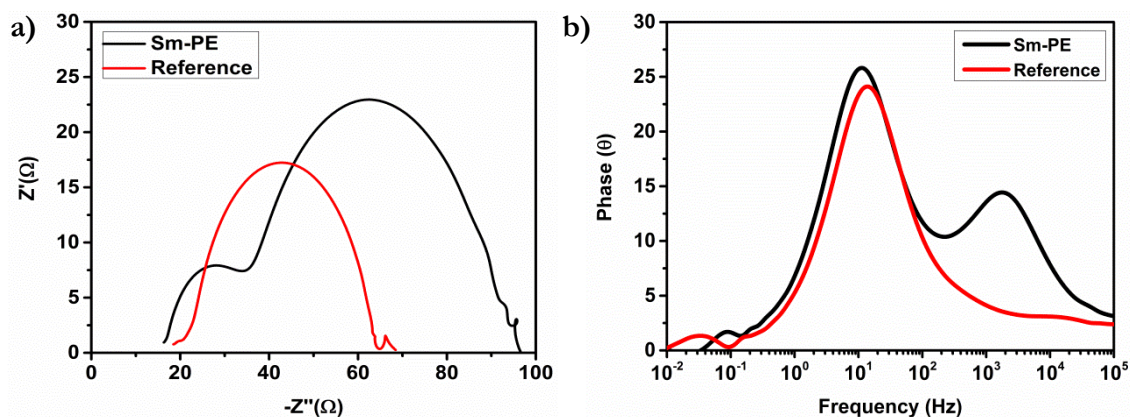


Figure 6.9 a) Nyquist and b) Bode plot of DSSCs measured in dark conditions at -0.7 V applied bias measured at 25 °C.

6.3 Control of LC template alignment

6.3.3 Preparation of LC template through the application of E

Figure 6.10 shows the POM and SEM of the E aligned sample. The binary LC mixture showed a marked difference after applying an electric field which shows that the LC materials were switched. The realignment of the directors of the LC molecules changed the optical transmission which is characterised by the opaque texture. The molecules are thought to be aligned parallel to the E and thus allow light to pass through. However, this is not the case here. Applying E induced an overall planar alignment of the LC molecules, which is clearly evident from the POM images. After applying E , the morphology changed drastically to show a dark image, which means that the molecules realigned into a planar orientation with respect to the plane of the substrate (Figure 6.10a). This can be attributed to the more stable SmA LC 8/2 organosiloxane which could not be switched by the applied E ; only the more fluid-like nematic 5CB molecules were aligned by the applied E . Once the sample was switched, the structure remained in that state indefinitely after the removal of the field. The sample was subsequently polymerised under UV light. The resulting texture was the same as before the polymerisation (Figure 6.10b). Immersing the polymerised sample in acetone

removed the LC components, resulting in the formation of nanopores (Figure 6.10c). Figure 6.10d shows the SEM image of the LC template after the removal of the LC content. Figure 6.10e corresponds to the AFM image of the sample. The side view schematic diagram of the template upon applying E is shown in Figure 6.10f. It is thought that the focal conic structures formed layers with the reactive mesogens situated in between these layers.

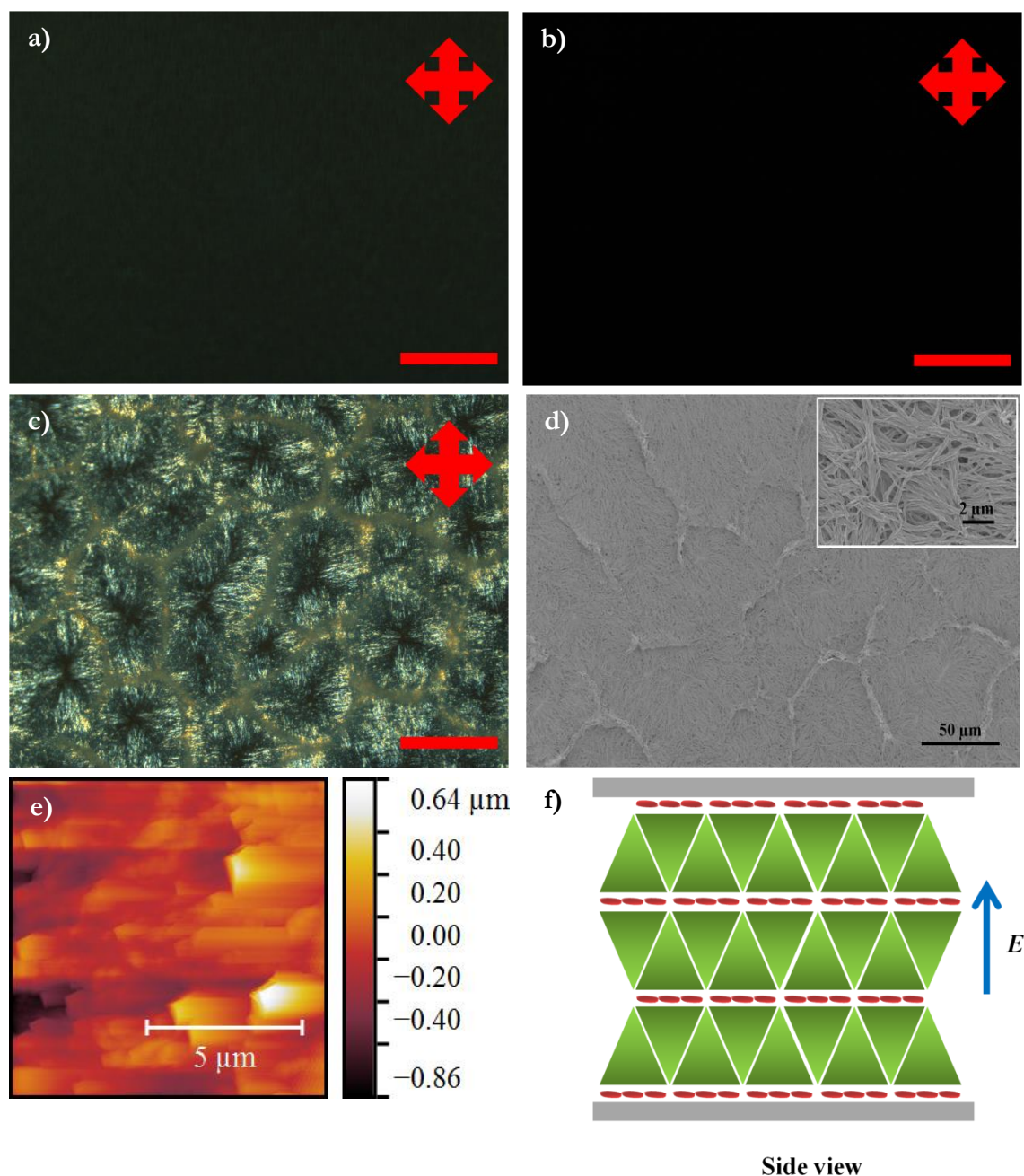
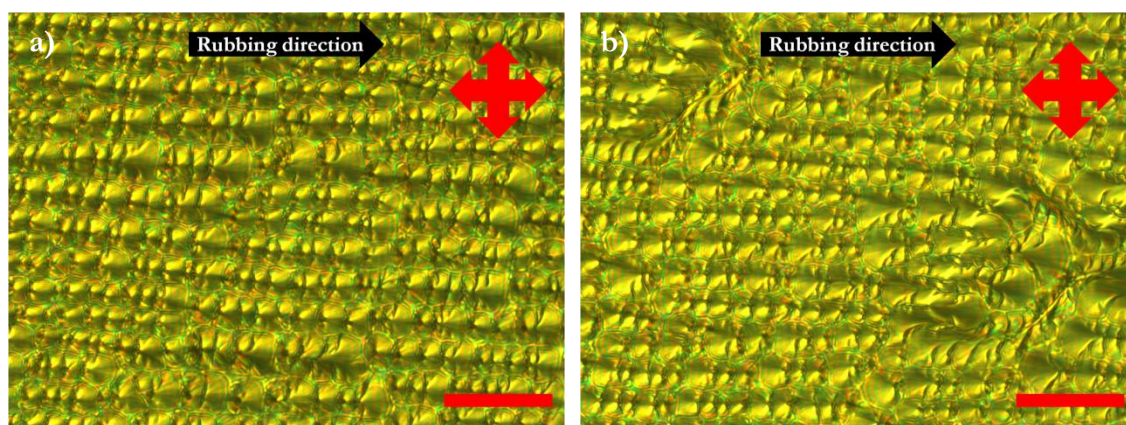


Figure 6.10 POM images of reactive mesogen mixtures after applying E , a) before polymerisation, b) after polymerisation and c) after removal of LC components with acetone.

d) SEM image and e) AFM image of the template. f) Schematic diagram of the mixture after applying *E*. The scale bar is 50 μm using X60 magnification.

6.3.4 Preparation of LC template using PI alignment layer

Next, an alignment layer was used on one side of the cell. The alignment layer was prepared by spin-coating a PI layer and was rubbed using a rubbing machine. This process led to the formation of micro-grooves where the LCs aligned according to the direction of the grooves. After filling with the binary mixture, a different morphology could be observed where the polygonal structures arranged themselves in the direction of the PI alignment layers instead of randomly, as in the case of the self-assembled sample (Figure 6.11a). The size of these polygonal structures was also found to be similar. This can be explained by the micro-grooves prepared by the rubbing machine that are thought to have the same width. Even after UV polymerisation of the sample, no visual change was observed (Figure 6.13b). After the removal of the LC components, the morphology of the sample changed significantly where the polygonal structures could no longer be observed (Figure 6.11c). However, the alignment of the polymer materials could still be observed. Unlike the self-assembled sample, their pores are extremely small, which means that the polymer is closely packed and dense. A similar morphology was observed using SEM where the polymers are lying parallel to the substrate and are aligned in one direction (Figure 6.11d). The inset picture shows the fibrous aggregates. Figure 6.11e) shows the schematic diagram of the morphology. Figure 6.11e) shows the AFM image of the template after the removal of the LC components. Figure 6.11f) shows the top view schematic diagram of the mixture when aligned using the PI alignment layer. In this case, it is hypothesised that the polygonal structures of SmA LCs arranged themselves in the rubbing direction, with the reactive mesogens aligned in between the polygonal structures and parallel to the rubbing direction.



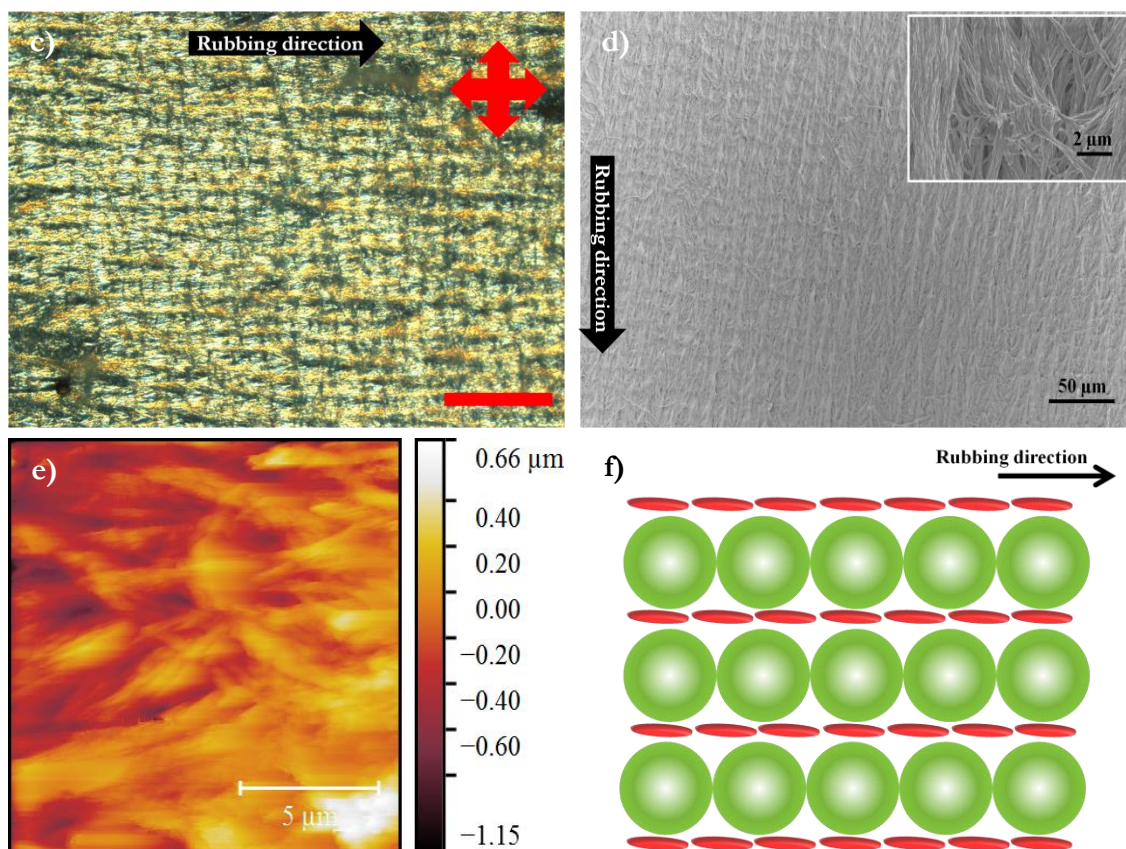


Figure 6.11 POM images of reactive mesogen mixtures with a PI alignment layer a) before polymerisation, b) after polymerisation and c) after the removal of LC components with acetone. d) SEM image and e) AFM image of the template. f) Schematic diagram of the mixture with a PI alignment layer. The scale bar is 50 m using X60 magnification. The black arrow shows the rubbing direction.

6.3.5 Current-voltage measurement

The effect of the different structure on ionic conductivity was determined using current-voltage measurement. The measurement was performed at room temperature. The resistivity of the electrolyte was taken as the inverse value of the slope in the linear region of the curve. From the I - V measurement, it was found that the ionic conductivity is higher in the case of the **E** aligned sample ($1.78 \times 10^{-3} \text{ S m}^{-1}$) compared to the PI aligned sample ($1.49 \times 10^{-3} \text{ S m}^{-1}$). The highly ordered sample induced better ionic conduction within the nano-pores by having more conduction channels. The ionic diffusion of the sample was also investigated using steady state voltammetry. The ionic diffusion experiments also corroborated the ionic conductivity data where the **E** aligned sample ($3.54 \times 10^{-7} \text{ cm}^2 \text{ s}^{-1}$) has higher ionic diffusion compared to the PI aligned sample ($3.23 \times 10^{-7} \text{ cm}^2 \text{ s}^{-1}$). A similar result was also observed by

Golodnitsky *et al.*, who showed that an improvement in ionic conductivity was obtained when a magnetic field was applied to polyethylene oxide polymer electrolyte (Golodnitsky et al. 2004). The result is also strengthened by the ionic diffusion data. Table 6.13 summarises the ionic diffusion and conductivity for the two different electrolytes.

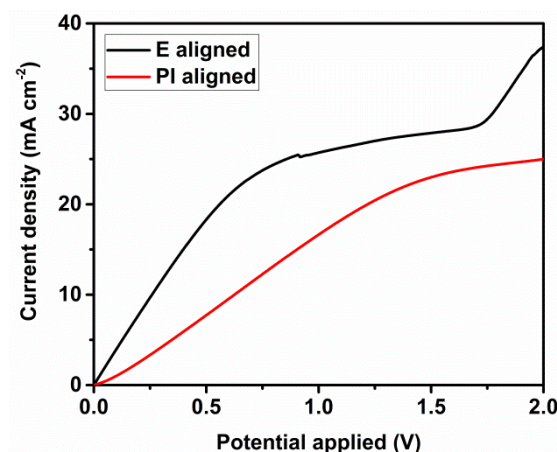


Figure 6.12 Linear sweep voltammetry curve of the **E** aligned sample and the PI aligned sample measured at 25 °C in a symmetric 25 μm Pt-coated FTO-FTO cell.

Figure 6.12 shows the linear sweep voltammetry for the **E** aligned and PI aligned samples. The ionic diffusion of the samples was calculated to be $3.54 \times 10^{-7} \text{ cm}^2 \text{ s}^{-1}$ for the **E** aligned sample and $3.23 \times 10^{-7} \text{ cm}^2 \text{ s}^{-1}$ for the PI aligned sample. The ionic diffusion for the **E** aligned sample is slightly higher than the PI aligned sample. Since the **E** aligned sample is more porous, the ionic transport is better than for the PI aligned sample.

Table 6.412 Ionic diffusion and conductivity data of the **E** aligned sample and the PI aligned sample measured at 25 °C at 1 kHz.

Sample	Ionic diffusion ($\text{cm}^2 \text{ s}^{-1}$)	Ionic conductivity (S m^{-1})
E aligned	3.54×10^{-7}	1.78×10^{-3}
PI aligned	3.23×10^{-7}	1.49×10^{-3}

6.3.6 Photovoltaic properties

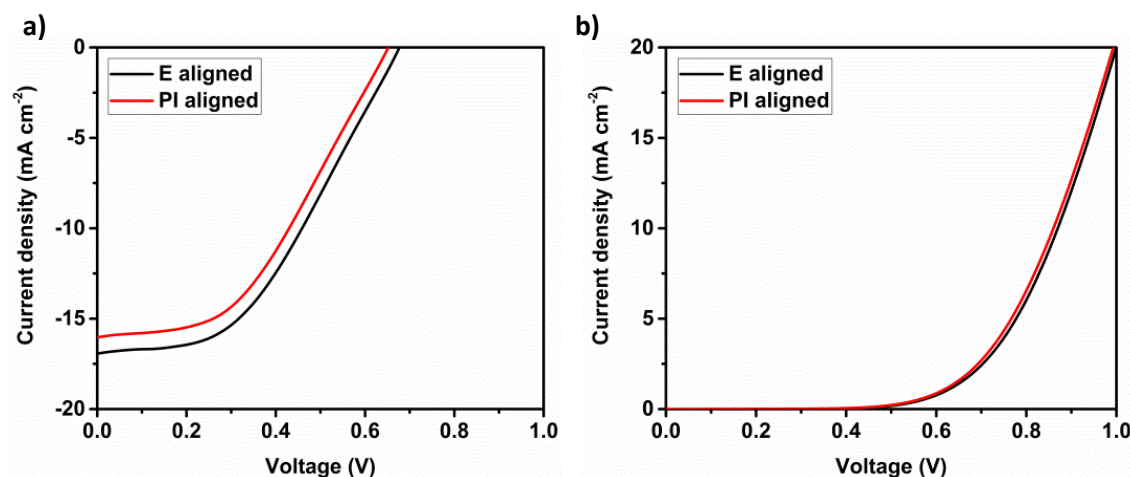


Figure 6.13 a) Light and b) dark J - V of the best performing solar devices for the **E** aligned sample and the PI aligned sample measured at 25 °C.

Subsequently, DSSCs were fabricated as an example of an application for these electrolytes. The J - V curves of the two different devices are shown in Figure 6.15 and the measured photovoltaic parameters of the two devices are summarised in Table 6.5. The **E** aligned sample showed a $J_{sc} = 16.93 \text{ mA cm}^{-2}$, $V_{oc} = 0.68 \text{ V}$ and FF of 43.73 %, corresponding to an efficiency of 5.02 %. The performance obtained with the cell prepared using a PI alignment layer was $J_{sc} = 16.03 \text{ mA cm}^{-2}$, $V_{oc} = 0.65 \text{ V}$ and a fill factor of 43.73 %, corresponding to an efficiency of 4.57 %.

Table 6.5 Photovoltaic properties of DSSC devices prepared using the **E** aligned and the PI aligned samples. The value is the average of four different samples and the value for the best performing is given in the parentheses.

Sample	J_{sc} (mA cm^{-2})	V_{oc} (V)	FF (%)	η (%)
E aligned	13.61 (16.93)	0.69 (0.68)	47.10 (43.73)	4.35 (5.02)
PI aligned	13.29 (16.03)	0.68 (0.65)	48.41 (43.73)	4.23 (4.57)

As can be seen from Table 6.5, apart from the J_{sc} , all other parameters are almost similar across the two devices. This is to be expected because the materials used to fabricate the sample are the same, and only the morphology is different. The J_{sc} is highly dependent on the ionic conductivity of the sample. It has been shown that the ionic conductivity for the **E**

aligned sample is higher than that for the PI aligned sample due to the polymer structure of the sample.

6.3.7 Electrochemical impedance spectroscopy

Figure 6.16 shows the Nyquist and Bode plot of the devices measured under dark conditions at an applied bias of -0.7 V. The R_s for both devices is almost similar. This is as expected because they were fabricated with the same material. However, the R_{Pt} and R_{ct} for both DSSCs show a significant difference. In the case of the PI aligned device, since the width between neighbouring polymer fibres is very small, the charge transfer from the electrode to the electrolyte is limited, resulting in the higher R_{Pt} . This also explains why the J_{SC} is lower in the case of the PI aligned sample, as the catalytic surface area is small compared to that of the **E** aligned sample. For the same reason, the high R_{CT} means that the charge transfer from the electrolyte to the conduction band of TiO_2 is highly suppressed in the case of the PI aligned sample. As the **E** aligned sample is more porous compared to the PI aligned device, the ionic transport is expected to be more efficient, resulting in the lower R_{Pt} and R_{CT} . Table 6.6 summarises the charge resistances and the electron lifetime.

Table 6.6 Summary of EIS parameters for the **E** aligned and PI aligned polymer electrolyte DSSCs.

Device	R_s (Ω)	R_{Pt} (Ω)	R_{CT} (Ω)	τ_e (ms)
E aligned	16.19	45.00	86.78	21.9
PI aligned	13.82	64.47	113.09	18.3

The electron lifetime, τ_e , can be calculated from the Bode plot using equation 6.2. The electron lifetime shows the lifetime of the electron in the TiO_2 semiconductor before recombining with the I_3^- in the electrolyte. In an ideal DSSC, a longer τ_e is favourable. It is calculated that the τ_e for the **E** aligned device (21.9 ms) is longer than that of the PI aligned device (18.3 ms). This shows that the suppression of the back-recombination reaction is better in the case of the **E** aligned device. This result agrees well with the result observed in the dark $J-V$.

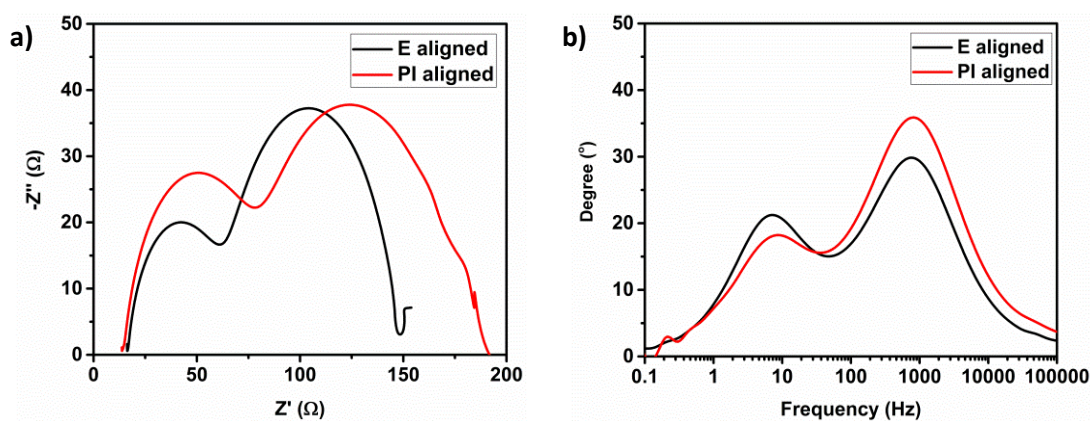


Figure 6.14 a) Nyquist plot and b) Bode plot used to determine the charge transfer characteristics and electron lifetime in the two devices measured in dark conditions at 25 °C.

6.4 Conclusion

In conclusion, binary mixtures of varying SmA and N compositions were prepared and characterised, and the mixture showing the most ordered textures under crossed polarisers was identified. It was shown that the structure of the phases depends strongly on the SmA component because the molecule is larger compared to E7. The function of this binary LC mixture is to provide a template for the reactive mesogen LCs that will be added later. The RM was then added to the optimised binary LC mixture and UV-polymerised to form a highly ordered, self-assembled reactive mesogen polymer network. As a potential application of the LC polymer templates, we prepared DSSC devices. DSSCs fabricated using these nanostructures show promising properties such as an increase in the V_{OC} , J_{SC} and η . The increase in the photovoltaic parameters is thought to be due to the formation of channels that aided the ionic conduction and the increase in the electron lifetime, which was supported by the EIS measurement. Further to this, the light scattering by the Sm-PE also played a role in increasing the efficiency as it increases the probability of the dye being excited by the incoming light.

New methods of preparing a highly ordered polymer electrolyte have been proposed either by manipulating the self-assembly nature of LCs or by applying an electric field. However, despite the more ordered structure in the case of the PI aligned sample, the **E** aligned sample showed higher ionic conductivity and therefore better solar cell performance. The efficiency of the **E** aligned DSSC is 5.02 % versus 4.57 % for the PI aligned device. This can be attributed to the morphology of the polymer network where the porosity is higher in the case

of the *E* aligned sample. In the PI aligned sample, the distances between polymer fibres are very close and thus reduce the porosity.

Further improvement could be attained by using different reactive mesogen that can respond well to the ionic liquid component used in this study. Further development of these templated electrolytes has the potential of enhancing the PCE even more. The self-assembly of micro-channels to contain the electrolyte to form a polymer electrolyte can be exploited in several energy storage/conversion applications. These results demonstrate a new pathway on the possibility of incorporating LCs to provide an ordered template in DSSC research, thus widening the possible application of these self-assembled nanostructures photovoltaic research. This could include applications in Li-ion batteries, fuel cells, capacitors and solar cells.

Chapter 7 Graphene counter electrodes

7.1 Foreword

In Chapter 6, we discussed the importance of controlling the morphology or structure of materials, especially in electronic device applications where these properties are greatly affected by structure. Although presenting a very attractive alternative, the control of morphology through the use of **E** or alignment layers is problematic and undesirable if high voltage is required. Gr, which is an sp^2 bonded carbon atom forming a hexagonal pattern, has been shown to act as a template for the synthesis of organic and inorganic materials (Boston et al. 2015; Wang et al. 2010). Gr supports the self-assembly of materials into novel nanostructures, which is directed by its two-dimensional morphology. Regarding LCs, there are several studies showing the use of Gr as the electrode in LC devices (Kim et al. 2011; Shehzad et al. 2015). The LCs are reported to align on the Gr due to strong epitaxial anchoring on the surface of the Gr. Gr fulfils all the requirements to be used as electrodes, such as high optical transmittance, excellent electronic transport, high flexibility and outstanding mechanical strength.

In this chapter, we first investigate the interaction of an NLC on a Gr surface under crossed polarisers. This will provide a qualitative evaluation of the possible alignment of the LC materials on a graphene Gr. Next, we compare the performance of different counter electrode configurations in DSSCs. LC-PEs investigated in Chapter 4 are then used in the Gr-based DSSCs, and the effect of the Gr on LC-PEs is examined using an optical microscope. An EIS study gives information on the charge transport properties occurring in these devices.

7.2 Interaction of LCs with graphene

Figure 7.1a shows a POM of a thin layer of BL006 spin-coated on a CVD-Gr layer where the different domains of Gr can be seen with the BL006. Rotating the sample from 0° to 90° changes the colours of the domains where the bright domains turned dark and vice versa. This showed that the LC materials were strongly aligned parallel to the Gr layer due to π - π stacking interactions exerted by the Gr domains. Alternatively, LC material in an ITO-ITO cell showed partial planar alignment in the case of a clean substrate. However, the presence

of impurities, such as oil, induce a partial planar and homeotropic alignment and only show a dark state under crossed polarisers, as seen in Figure 7.1b. Figure 7.1 shows POM images of spin-coated BL006 on a) a Gr substrate and b) an ITO substrate.

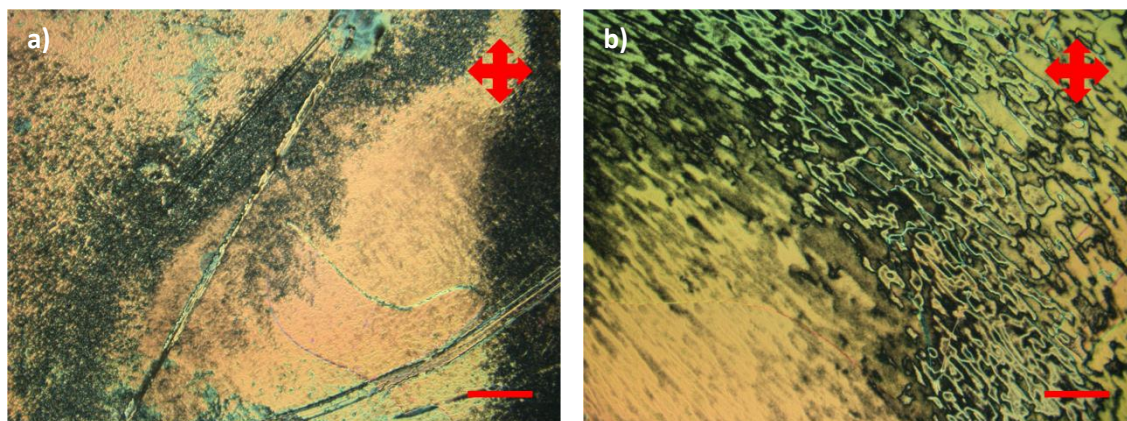


Figure 7.1 POM images of BL006 spin-coated onto a) a Gr electrode and b) ITO observed at 25 °C.

7.3 Graphene counter electrode DSSCs

7.3.1 Comparison of different Gr-based electrodes

Gr was transferred onto an FTO substrate using the wet transfer process, as explained in Chapter 3. The process of transferring clean and wrinkle-free Gr onto a Pt layer proved difficult, unlike the transfer process on FTO and ITO substrates. Cracks and holes were observed on Gr transferred on the Pt-coated substrate. These are reportedly due to the roughness of the surface of the substrate imparted by the Pt nanoparticles and also depend on the wettability of the substrates (Du et al. 2015; Hong et al. 2016). To overcome the issue of wrinkled Gr, a post-annealing process is recommended to obtain a clean Gr (Bao et al. 2009; Xie et al. 2015). Therefore, different architectures of Gr based counter electrodes- FTO+Gr, FTO+Pt+Gr without annealing (450 °C), FTO+Gr annealed, FTO+Pt+Gr annealed and FTO+Gr+Pt were prepared. All substrates were prepared using the wet transfer process. To determine the quality of Gr on these counter electrodes, Raman spectroscopy was performed. Figure 7.2 shows the Raman spectra. A typical Raman spectra is shown in Figure 7.2a where three major peaks-the 2D peak, the G peak and the D peak- can be observed. The 2D and G peaks are characteristic of Gr and these peaks give the information as to how many layers of Gr are deposited and if the Gr is doped/strained. The D peak tells if there are defects in the Gr. No D peak was observed for the Gr transferred

onto an FTO substrate; this was to be expected as no post-processing step was performed on this sample. However, upon annealing the FTO+Gr substrate, a small D peak started to appear. Yet, the 2D and G peaks were still observed, which means that the Gr had some defects. A similar spectrum was also observed for the FTO+Pt+Gr substrate where a small D peak was observed. However, for the FTO+Gr+Pt substrate, the signature peaks for Gr could no longer be observed, although the Gr layer on the substrate was still visible. This might be because the Raman laser could not penetrate the Pt layer on top of the Gr.

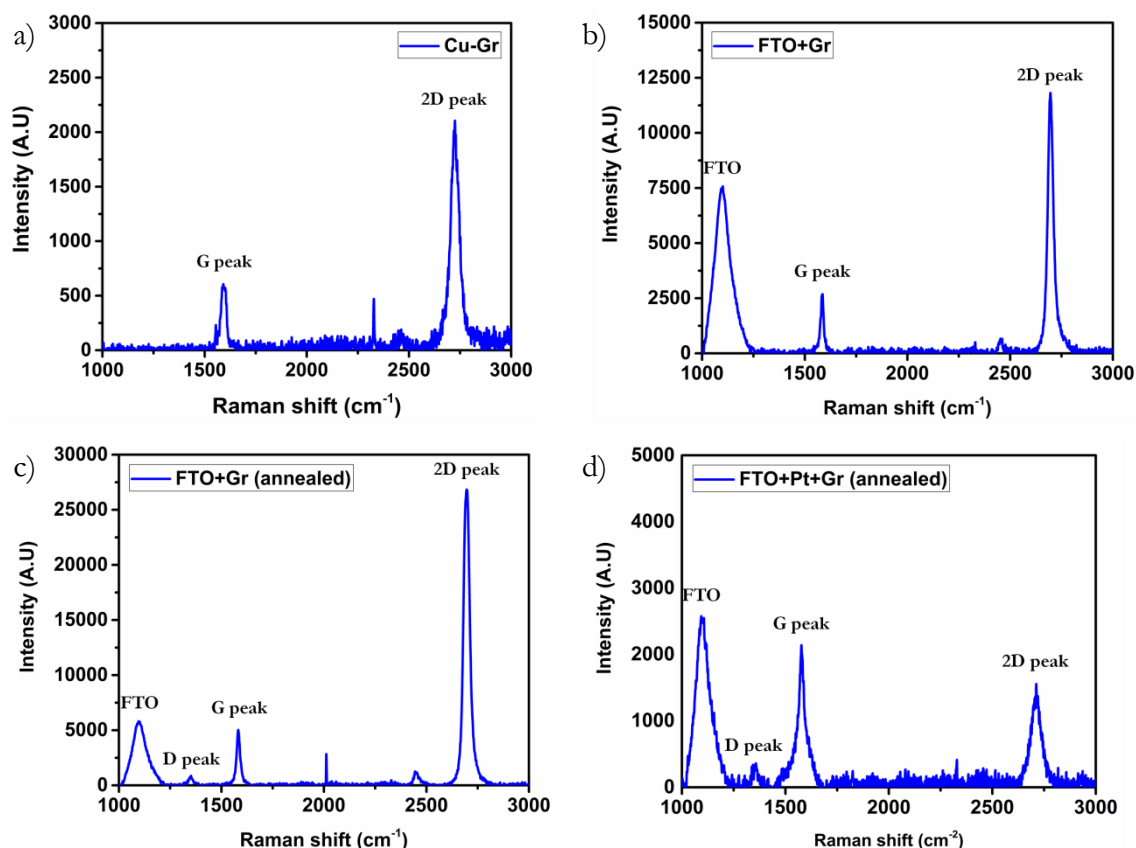


Figure 7.2 Raman spectroscopy of Gr on different electrodes and annealing conditions. a) Gr on copper foil, b) Gr transferred onto an FTO substrate, c) Gr transferred onto FTO substrate after annealing and d) Gr transferred onto a Pt-coated FTO substrate after annealing. The Raman spectra was provided by Mr. Philipp Braeuninger from Prof. Stephan Hoffman's group.

7.3.2 Photovoltaic properties

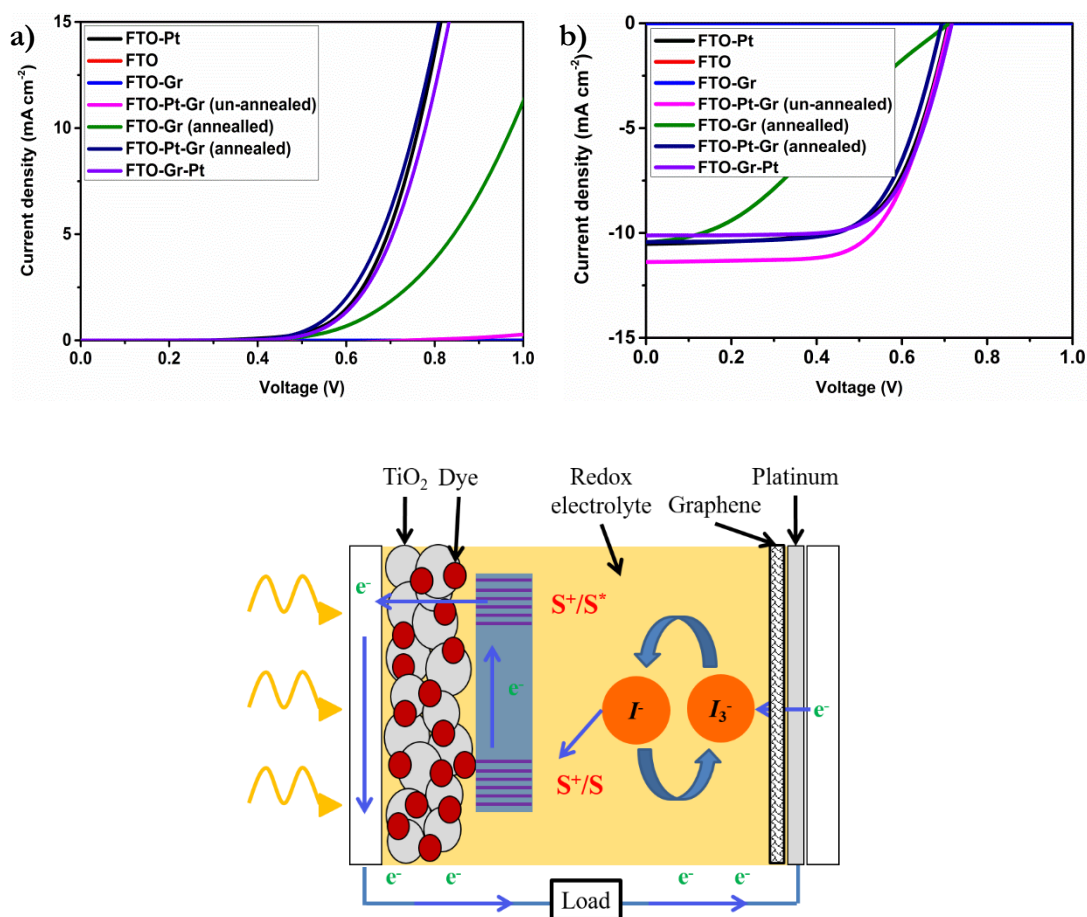


Figure 7.3 J - V curves for different photocathode configurations under a) dark and b) light condition measured at 25 °C under 1 sun illumination. c) Schematic diagram of Gr-based DSSC.

Table 7.1 Summary of photovoltaic parameters for different photoanode configurations.

Device	J_{sc} (mA cm ⁻²)	V_{oc} (V)	FF (%)	η (%)
FTO	1.14	0.39	8.2	0.04
FTO-Gr	3.57	0.66	7.6	0.17
FTO-Gr (annealed)	10.30	0.71	32.5	2.43
FTO-Pt	10.45	0.72	65.1	4.86
FTO-Pt-Gr (un-annealed)	11.52	0.71	66.7	5.48
FTO-Pt-Gr (annealed)	10.55	0.69	67.6	4.95
FTO-Gr-Pt	10.14	0.72	68.1	4.98

The DSSC fabricated with the FTO-only photocathode showed the lowest efficiency of 0.04 %. This is due to the lack of a catalytic layer for the redox process of the I/I_3^- redox

couple. The Pt-layer is important to reduce the oxidised I_3^- into I^- . Without this process, a charge cannot be generated; therefore, a low J_{sc} was observed. Next, a layer of Gr was transferred onto the FTO, and a photovoltaic device was fabricated. This resulted in the two-fold increase in the J_{sc} and V_{oc} . This means that the Gr can act as a catalyst for the I^-/I_3^- redox couple. This is as expected because Gr is made of carbon atoms. Carbon counter electrodes have been studied as alternatives to the more expensive Pt counter electrodes. However, the efficiency of this device was still very low. A study by Zhang *et al.* showed the effects of different temperatures in the annealing process of Gr counter electrodes on the performance of DSSC devices (Zhang et al. 2011). Therefore, an annealing treatment was performed on the Gr counter electrode, resulting in a significant improvement in performance. This can be attributed to a better surface connection between the Gr layer and the FTO substrate. It is also thought that the polymer sacrificial layer during the Gr transfer process might have been removed due to the annealing treatment, leading to better surface adhesion. This is evident from the high J_{sc} obtained for this device architecture.

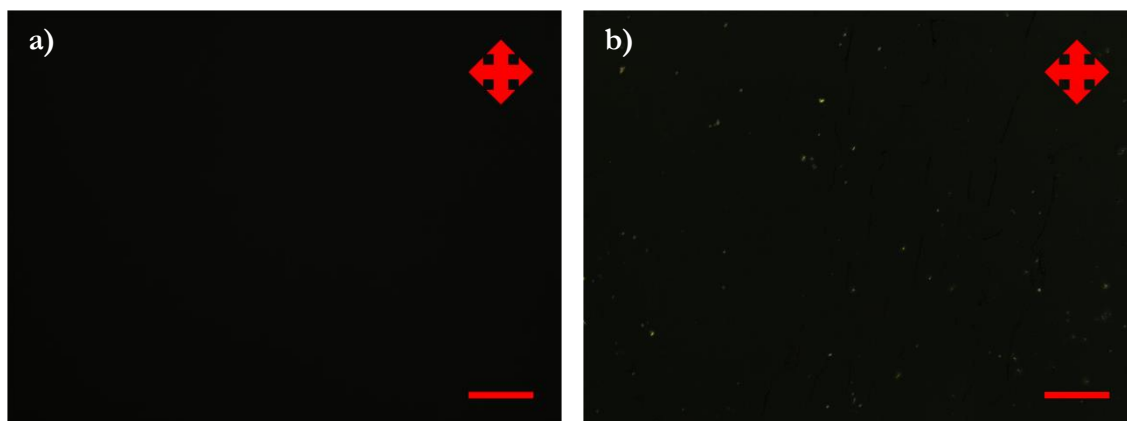
Next, hybrid Pt-Gr counter electrodes were studied. First, a device with an FTO-Pt-Gr (without post annealing) counter electrode was fabricated. This device showed high photovoltaic parameters of $J_{sc} = 11.52 \text{ mA cm}^{-2}$, $V_{oc} = 0.71 \text{ V}$ and $\eta = 5.48 \%$. This originates from the higher electrocatalytic properties when using the Gr layer together with the Pt layer. With the addition of the Gr layer, the surface area for the catalytic reaction was also improved. Next, the effect of thermal treatment on the same counter electrode structure was investigated. It was observed that the J_{sc} was reduced but the V_{oc} was improved. The reduction in the J_{sc} might be due to the degradation of the Gr layer at high temperatures, while the enhanced V_{oc} might be due to the positive shift of the redox potential of the I^-/I_3^- redox couple. Finally, an FTO-Gr-Pt counter electrode was used to fabricate a DSSC device. This type of device showed the lowest J_{sc} (10.14 mA cm^{-2}) amongst the devices tested. The degradation of the Gr layer is thought to be the cause of the low J_{sc} . This degradation affects the surface interaction between the FTO, Gr and Pt interfaces by impeding the charge transfer from the counter electrode to the electrolyte. In the Raman study above, it can be seen that annealing led to the formation of multilayered Gr from the 2D and G peaks where the G peak was higher than the 2D peak. However, the efficiency is still higher than that of the reference DSSC. In comparison, the reference electrolyte showed $J_{sc} = 11.45 \text{ mA cm}^{-2}$, $V_{oc} = 0.72 \text{ V}$ and $\eta = 4.86 \%$.

It was established that FTO-Pt-Gr architecture gave the best photovoltaic performance. Using this architecture, the interaction between LC-PE composites and Gr was investigated by studying DSSC devices. These electrolytes were capillary-filled into Gr-based DSSCs.

7.3 Interaction of LC-PEs with the graphene electrode

7.3.1 Polarising optical microscopy

A POM study was performed to elucidate the effect of the Gr interaction with the LC-PE composites. Figure 7.4 shows POM images of different LC-PEs filled in ITO-Gr cells under crossed polarisers. POM was performed from the Gr side. The birefringence observed in Figure 7.4 is generally lower than that observed in ITO-ITO cells (Figure 5.1). It is thought that the Gr electrode induces planar alignment of the LC materials; therefore, it can be observed under the microscope. As the LC content increases, it is expected that the birefringence increases at the same time since the composition of the LC increases. However, unlike in ITO-ITO cells, this was not the case. This can be attributed to the higher overall alignment effect in the LC materials. It can also be observed that the aggregations of the ionic liquids became more prominent with the increase in LC content. This also proves that there was indeed interaction between the ionic liquid and the LC molecules. Without the attractive interaction between the DMPII and 5CB, no birefringent images could be observed under crossed polarised POM since the DMPII molecule is not expected to show birefringence.



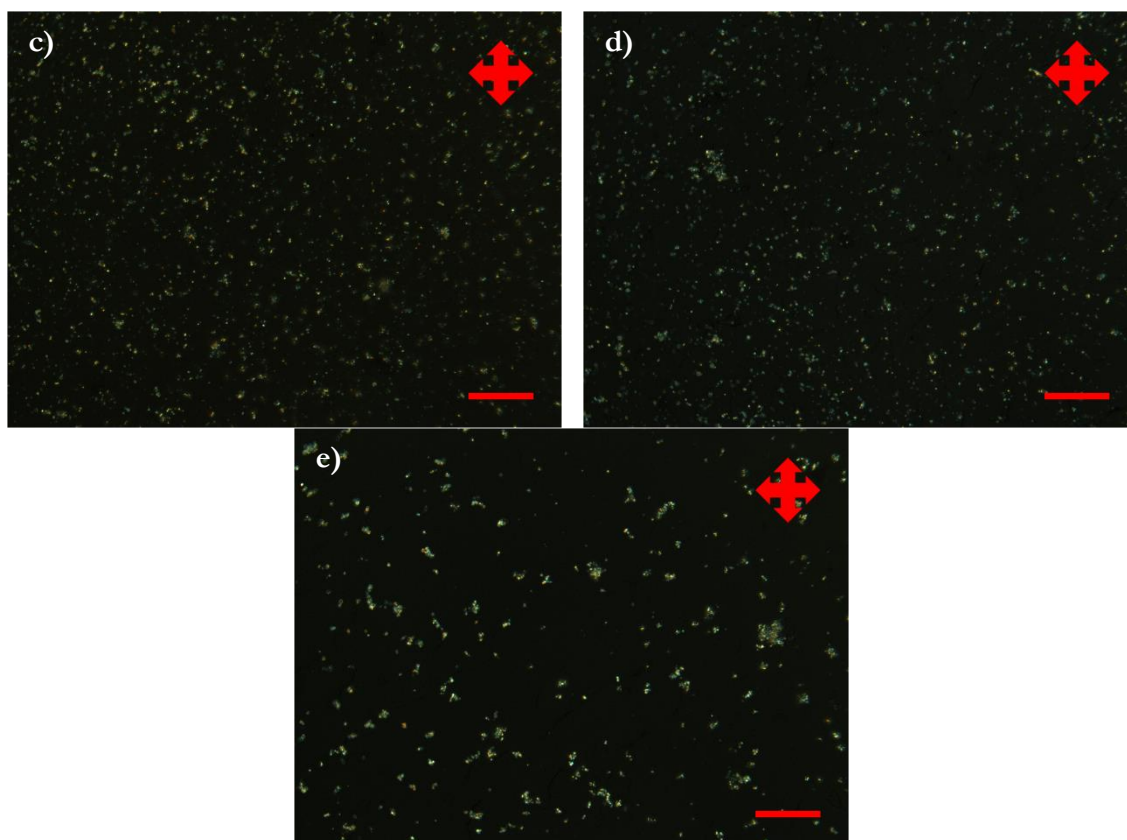


Figure 7.4 POM images of LC-PEs in a 25 μm Gr-ITO cell observed from the Gr side under crossed polarisers at 25 $^{\circ}\text{C}$. a) 0% 5CB, b) 5% 5CB, c) 10% 5CB, d) 15% 5CB and e) 20% 5CB.

7.4.2 Photovoltaic properties

Next, a pure polymer electrolyte and LC-PEs with different LC concentrations were used to fabricate Gr-based DSSCs. Figure 7.5 shows the dark and light J - V of the solar devices. Unlike with Pt-only electrodes, with a Gr counter electrode, the DSSC highest efficiency was obtained with the pure polymer electrolyte, showing $J_{\text{sc}} = 14.31 \text{ mA cm}^{-2}$, $V_{\text{oc}} = 0.68 \text{ V}$ and $\eta = 4.80 \%$. This value was several orders of magnitude higher than the DSSC prepared with only Pt. Increasing the content of the LCs in the polymer electrolyte also increased the efficiency. Interestingly, however, the improvement in the efficiency was seen to get smaller with higher concentrations of LCs. This can be related to how the LC molecules arrange themselves near the surface of the Gr layer. As explained previously, due to the π - π stacking interaction of Gr and the benzene rings of the LC molecules, the molecules tend to align themselves parallel to the Gr substrate. However, it is believed that this effect is strongest near the surface of the Gr and does not replicate to the whole cell.

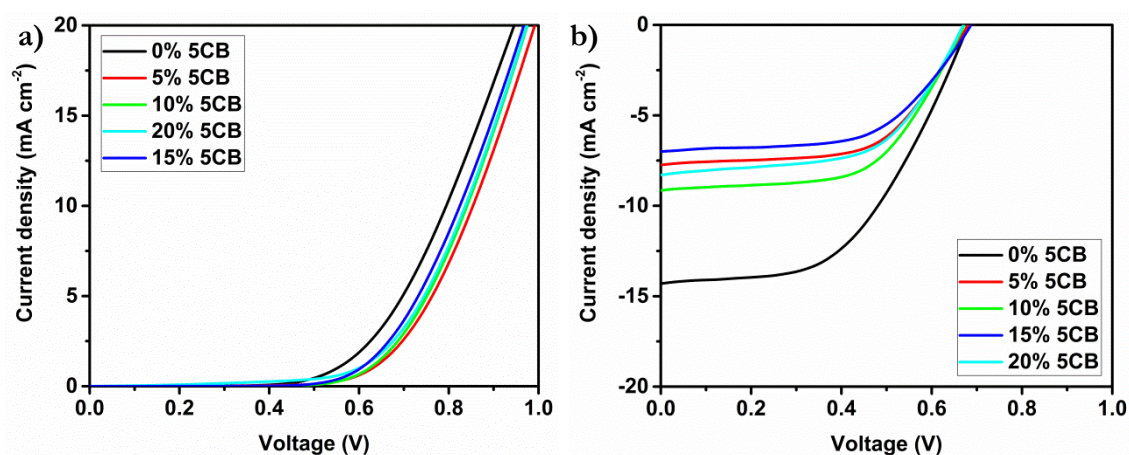


Figure 7.5 J - V curves of Gr-based DSSCs using a pure polymer electrolyte and LC-PEs a) in dark conditions and b) under 1 sun illumination measured at 25 °C.

Table 7.2 Photovoltaic performance of the Gr-based DSSCs fabricated with different LC-PEs.

5CB (%)	J_{sc} (mA cm ⁻²)	V_{oc} (V)	FF (%)	H (%)
0	14.31	0.68	51.16	4.80
5	7.75	0.68	59.36	3.13
10	9.15	0.67	58.52	3.60
15	7.00	0.69	57.94	2.79
20	8.28	0.67	57.98	2.30

Figure 7.5a shows the dark current-voltage characteristics of the four devices. The dark current gives information on the kinetics of the reaction of the electrons from mesoporous TiO_2 with I_3^- in the electrolyte. It is seen that the onset voltage for the higher LC contents, in particular 15 % and 20%, was lower than that of the other devices. As the amount of LCs was greater in these two devices, the effect of induced alignment by the Gr was higher. Instead of passivating the TiO_2 surface through the adsorption of cyano groups on the TiO_2 surface, the molecules were pulled towards the Gr surface where they tended to align parallel to the substrate.

7.4.3 Electrochemical impedance spectroscopy

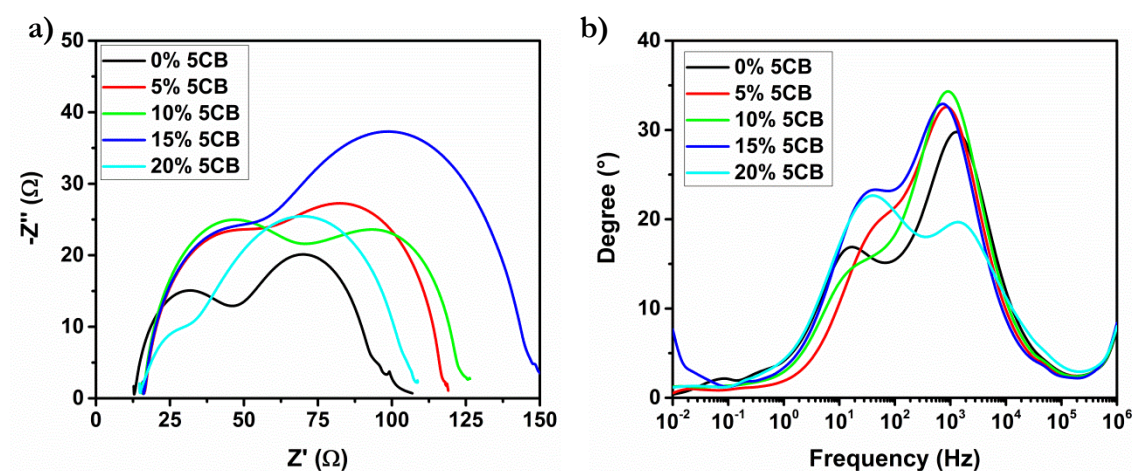


Figure 7.6 a) Nyquist plot and b) Bode plot of the photovoltaic devices for different LC-PEs fabricated using a Gr-based counter electrode measured at 25 °C under the dark conditions.

The Nyquist plot (Figure 7.6a) and the Bode plot (Figure 7.6b) obtained from the EIS measurement can give insight into the charge transport parameters within the solar device. As can be seen from the Nyquist plot, the onsets were similar across all devices, which is as expected because the same Gr counter electrode was used. The small difference between the R_s can be attributed to fabrication errors which can be neglected. R_{pt} is seen to increase with the increase of LCs which means that the charge transfer was hampered in this case.

The electron lifetime can be calculated from the Bode plot using Equation 5.2. As with the efficiency, the lifetime was also affected by ion transport within the polymer electrolyte. The lifetime gives information on how long an electron stays in the TiO_2 before being intercepted by the electrolyte. The longer the lifetime, the better the efficiency will be, although there are other parameters that govern the efficiency of the device. In this measurement, it was found that the 10% sample had the highest τ_n of 9.7 ms. Increasing the LC content decreased the τ_e , which supports the previous argument that the effect of the back-recombination reaction was greater with a higher LC content.

Table 7.2 Electron lifetime at different 5CB composition for Gr-based DSSCs measured at 25 °C under dark conditions.

5CB (%)	R_s (Ω)	R_{pt} (Ω)	R_{ct} (Ω)	τ_e (ms)
0	12.9	33.0	75.9	9.6
5	16.3	41.2	79.0	3.0
10	15.7	55.3	75.4	9.7
15	16.1	41.3	113.0	3.5
20	14.8	18.2	93.2	3.9

7.5 Summary

We have shown that Gr exerted an alignment effect on LC materials. The strong interaction between LCs and Gr induced planar alignment, despite the mismatch of structure between the two. In addition, the use of Gr as the counter electrode improved the performance of the DSSCs. This is due to the catalytic properties of Gr that improve the redox reaction of the electrolyte. Regardless of the presence of defects in Gr after the transfer onto FTO substrates, higher efficiency was observed with the FTO-Pt-Gr DSSC. The integration of LC-PEs in Gr-based DSSCs also improved the overall performance of the devices. It was observed that the increase in the efficiency got smaller with the increase in LCs. Higher LC content means that the LC components have a more dominant role in the polymer electrolyte system. Therefore, the interaction between the LC molecules and Gr becomes more prominent.

Chapter 8 Conclusion and Future Work

8.1 Conclusion

This thesis primarily explores the application of self-assembled LC materials and new fabrication methods for electrolyte development in relation to DSSCs and utilising LCs. LCs have been well studied and LC-related industries revolving around displays and imaging are worth more than \$100 billion. The flat panel display industry alone contributed \$129 billion to the economy in 2015. Despite being widely researched, the application of LCs is traditionally limited to display applications. In more recent years, there has been intense research of non-display applications of LCs, such as in electronic and photonic devices. The intrinsic ability of LCs to self-assemble has allowed the exploitation of their electronic, magnetic and optical properties for a potentially wide range of applications. This thesis has focused on the application of LCs in DSSCs, namely their role in the electrolyte redox couple component of DSSCs. The key findings are summarised as follows:

- The polymer electrolyte was doped with LCs (LC-PEs) for DSSCs. A higher electrical conductivity and photovoltaic response was observed. The LC-PEs also demonstrated a higher scattering effect, resulting in higher DSSC performance.
- The variation in alkyl chain length of a homologous series of cyanobiphenyl (nCB) LCs, the ionic conductivity and the ionic diffusion showed an inverse relationship with the alkyl chain length. Similar trends were also observed for the DSSC devices where η reduced from 3.63 % for 5CB to 2.06 % for 10CB.
- Dielectric permittivity also affects the performance of the DSSCs. A positive $\Delta\epsilon$ LC material yielded better ionic conductivity and better overall DSSC efficiency. The improved ionic conductivity is attributed to the switching effect of LC molecules.
- Templating of the polymer electrolyte in a DSSC was achieved using a self-assembled LC template. A highly ordered reactive mesogen polymer network was prepared using E7:8/2 organosiloxane (80:20 vol:vol) mixture as the template. This highly porous polymer electrolyte showed higher ionic conductivity, ionic diffusion and overall photovoltaic properties compared to a reference DSSC. This is due to a more ordered ionic conduction and better ion dissolutions by the oxygen unit in the polymerised reactive mesogen.

- The morphology of the smectic-templated polymer network can be controlled using applied the \mathbf{E} and the PI alignment layer on the substrate. The electrical and photovoltaic response of the \mathbf{E} aligned sample was higher than the PI aligned sample, which can be attributed to the porosity of the templates. The PI aligned sample was observed to provide better alignment compared to the \mathbf{E} aligned sample. In addition, the \mathbf{E} aligned sample was less porous.
- Self-assembly of nematic (BL006) LCs was compared for a Gr-coated substrate and an ITO substrate. Use of the polycrystalline Gr substrate resulted in multi-domain LCs, whilst use of the ITO substrate resulted in a more ordered homeotropic alignment.
- The process of annealing the Gr-based electrodes resulted in the Gr having defects. Interestingly, despite these defects, it was found that the incorporation of Gr as the counter electrode in DSSCs improved the overall performance (post annealing).
- Increasing the LC content has a negative effect on the performance of Gr-based photovoltaic devices. This is assumed to be an effect of Gr which aligns the LC molecules parallel to the substrate and thus reduces the surface area for catalytic reaction of the redox electrolyte and impedes the ionic conduction mechanism.

8.2 Future work

8.2.1 Doping of liquid electrolytes with alkoxy cyanobiphenyl LCs

Here we have shown that improving the ionic conductivity and thus the efficiency of DSSCs can be achieved by doping with LC materials. The doping of liquid electrolytes with alkyl cyanobiphenyl LCs has been demonstrated by Koh *et al.* (Koh et al. 2013). It was shown that the cyano group attached to the surface of the TiO_2 semiconductor and thus passivated the surface from a liquid electrolyte. This improved the V_{OC} and the electron lifetime. In addition, it is a well-known fact that the presence of the oxygen unit acts as a reaction site for capturing the Li^+ ions, thus enhancing anion conduction. This can potentially be applied to LC molecules having oxygen groups. Interestingly, in our preliminary experiment with alkoxy cyanobiphenyl LCs in acetonitrile, gel formation was observed.

8.2.2 LC-templating with DLCs

In this thesis, we have shown that it is possible to prepare a highly ordered polymer network through the templating of reactive mesogens with an optimised NLC:SmA binary mixture.

The reactive mesogens conform to the polygonal structure of the binary mixture upon UV irradiation and the removal of the binary mixture, leaving a porous structure that is efficient at ionic conduction. Using the same idea, introducing DLCs as the template will allow the fabrication of planar alignment, which is excellent for in-plane conduction, or homeotropic alignment, which is good for out-of-plane conduction. As mentioned in Chapter 2, DLCs tend to self-assemble into a columnar structure due to the steric interactions and the π - π interactions between the cores.

8.2.3 DLC template with graphene electrode

In chapter 6, we discussed the possibility of preparing a highly ordered polymer structure using SmA LCs as the template, and in Chapter 7 the interaction between LC molecules and Gr was explored. Taking these two things into account, we proposed using a DLC template with a Gr electrode. As mentioned previously, the interaction between DLCs and Gr has not been studied extensively. Only a few works have been published on the interaction of DLCs and Gr (Shivanandareddy et al. 2014). As Gr layers have been shown to induce the alignment of nematic LC materials, it is expected that an even greater effect will be observed with DLCs because DLCs possess large aromatic cores, similar to the structure of Gr. The alignment of DLCs by a Gr layer will most likely result in a columnar structure with homeotropic alignment. Assuming the reactive mesogens are placed in between the columnar structures of DLCs, similar to the case of polygonal SmA structures, it is possible to control the size of the polymer network by changing the length of the alkyl chain of DLCs.

8.2.4 Thermoelectric devices

The working mechanism of a thermoelectric device is based on the thermal gradient to generate electricity. The efficiency of thermoelectric material is determined using the following equation:

$$ZT = \frac{S^2 \sigma T}{\kappa}$$

where ZT is the figure of merit, S is the Seebeck coefficient, σ is the conductivity, T is the temperature in Kelvin and κ is the thermal conductivity. To get a high ZT , a high S and high σ are required while keeping κ as low as possible. However, high σ comes with a trade-off high κ . The application of LCs in thermoelectrics research has been proposed in several

studies (Balagurusamy et al. 1999; Trashkeev and Kudryavtsev 2012). LC materials have been known to possess low κ . In this thesis, we have shown that the use of LCs in electrolytes, both in the case of LC-PEs and Sm-PEs, improves the ionic conductivity. The thermal conductivity of LCs has been shown to be extremely low (0.15~0.35 W/mK for 9CB) compared to other materials, such as metal (310 W/mK for gold). The thermal conductivity also shows a decreasing trend with an increase in the temperature as the LC materials become isotropic (Mercuri et al. 1998). Therefore, it is interesting to see the application of LC-based electrolytes as thermoelectric materials.

8.2.5 Batteries

Since the use of electronic devices has become widespread, batteries have become indispensable components. Batteries have three main components-an anode, a cathode and an electrolyte. Electrolyte materials must have excellent ionic conductivity, be inert to the electrodes and be thermally stable. Recently, the use of LCs as electrolyte components has been discussed by Sakuda *et al.* through the use of reactive mesogen (Sakuda et al. 2015). Furthermore, there are numerous studies on the use of Gr in the electrodes in battery systems (Wang et al. 2009; Yoo et al. 2008). The highly porous nature of the Sm-PEs allows for higher electrolyte uptake, which can provide higher ionic conductivity and prevent electrolyte leakage. By integrating LC-based electrolytes and Gr electrodes, it is thought that battery efficiency can be further improved.

References

- Ahmed, Saquib, Aurelien Du Pasquier, Tewodros Asefa, and Dunbar P. Birnie. 2011. "Improving Microstructured TiO₂ Photoanodes for Dye Sensitized Solar Cells by Simple Surface Treatment." *Advanced Energy Materials* 1(5): 879–87.
<http://onlinelibrary.wiley.com/doi/10.1002/aenm.201100121/full>.
- Ahn, Sung Kwang et al. 2012. "Development of Dye-Sensitized Solar Cells Composed of Liquid Crystal Embedded, Electrospun Poly(vinylidene Fluoride-Co-Hexafluoropropylene) Nanofibers as Polymer Gel Electrolytes." *ACS Applied Materials and Interfaces* 4(4): 2096–2100.
<http://pubs.acs.org/doi/full/10.1021/am3000598>.
- Akhtar, M Shaheer, Soonji Kwon, Florian J Stadler, and O Bong Yang. 2013. "High Efficiency Solid State Dye Sensitized Solar Cells with Graphene-Polyethylene Oxide Composite Electrolytes." *Nanoscale* 5(12): 5403–11.
<http://pubs.rsc.org/en/content/articlehtml/2013/nr/c3nr00390f>.
- Aldred, Mathew P et al. 2004. "Light-Emitting Fluorene Photoreactive Liquid Crystals for Organic Electroluminescence." *Chemistry of Materials* 16(24): 4928–36.
<http://pubs.acs.org/doi/full/10.1021/cm0351893>.
- Aldred, Matthew P. et al. 2005. "A Full-Color Electroluminescent Device and Patterned Photoalignment Using Light-Emitting Liquid Crystals." *Advanced Materials* 17(11): 1368–72. <http://onlinelibrary.wiley.com/doi/10.1002/adma.200500258/full>.
- Bach, U et al. 1998. "Solid-State Dye-Sensitized Mesoporous TiO₂ Solar Cells with High Photon-to-Electron Conversion Efficiencies." *Nature* 395(6702): 583–85.
<http://www.nature.com/nature/journal/v395/n6702/full/395583a0.html>.
- Balagurusamy, V. S K et al. 1999. "Quasi-One Dimensional Electrical Conductivity and Thermoelectric Power Studies on a Discotic Liquid Crystal." *Pramana - Journal of Physics* 53(1): 3–11. <http://link.springer.com/article/10.1007/s12043-999-0136-2>.
- Bandara, J, and J P Yasomanee. 2006. "P-Type Oxide Semiconductors as Hole Collectors in Dye-Sensitized Solid-State Solar Cells." *Semiconductor Science and Technology* 22(2): 20–

24. <http://iopscience.iop.org/article/10.1088/0268-1242/22/2/004>.
- Bao, Wenzhong et al. 2009. "Controlled Ripple Texturing of Suspended Graphene and Ultrathin Graphite Membranes." *Nature nanotechnology* 4(9): 562–66.
<http://www.nature.com/nnano/journal/v4/n9/full/nnano.2009.191.html>.
- Bella, Federico et al. 2014. "Additives and Salts for Dye-Sensitized Solar Cells Electrolytes: What Is the Best Choice?" *Journal of Power Sources* 264: 333–43.
<http://dx.doi.org/10.1016/j.jpowsour.2014.04.088>.
- Berreman, Dwight W. 1973. "Alignment of Liquid Crystals by Grooved Surfaces." *Molecular Crystals and Liquid Crystals* 23(3–4): 215–31.
<http://www.tandfonline.com/doi/abs/10.1080/15421407308083374>.
- Blinov, L.M. 1983. *Electro-Optical and Magneto-Optical Properties of Liquid Crystals*. UMI.
- Blinov, L.M., and V G Chigrinov. 1994. Springer-Verlag New York *Electrooptic Effects in Liquid Crystal Materials*. Springer New York.
- Boden, N, R Bushby, and J Clements. 1994. "Electron Transport along Molecular Stacks in Discotic Liquid Crystals." *Journal of Materials Science: Materials in Electronics* 5(2): 83–88.
<http://link.springer.com/article/10.1007/BF00187117>.
- Boschloo, Gerrit, Leif Häggman, and Anders Hagfeldt. 2006. "Quantification of the Effect of 4-Tert-Butylpyridine Addition to I⁻/I₃⁻ Redox Electrolytes in Dye-Sensitized Nanostructured TiO₂ Solar Cells." *Journal of Physical Chemistry B* 110(26): 13144–50.
<http://pubs.acs.org/doi/full/10.1021/jp0619641>.
- Boston, R. et al. 2015. "Graphene Oxide as a Template for a Complex Functional Oxide." *CrystEngComm* 17(32): 6094–97.
<http://pubs.rsc.org/en/content/articlehtml/2015/ce/c5ce00922g>.
- Bouteiller, L., and P. Le Barny. 1996. "Polymer-Dispersed Liquid Crystals: Preparation, Operation and Application." *Liquid Crystals* 21(2): 157–74.
<http://dx.doi.org/10.1080/02678299608032820>.
- Burschka, Julian et al. 2011. "Tris(2-(1 H -Pyrazol-1-yl)pyridine)cobalt(III) as P-Type Dopant for Organic Semiconductors and Its Application in Highly Efficient Solid-

- State Dye-Sensitized Solar Cells.” *Journal of the American Chemical Society* 133(45): 18042–45. <http://pubs.acs.org/doi/full/10.1021/ja207367t>.
- Bushby, Richard J, and Owen R Lozman. 2002. “Photoconducting Liquid Crystals.” *Current Opinion in Solid State and Materials Science* 6(6): 569–78. [http://dx.doi.org/10.1016/S1359-0286\(03\)00007-X](http://dx.doi.org/10.1016/S1359-0286(03)00007-X).
- Cahen, David, Gary Hodes, and Michael Gra. 2000. “Nature of Photovoltaic Action in Dye-Sensitized Solar Cells.” *The journal of physical chemistry. B* 9(104): 2053–59. <http://pubs.acs.org/doi/full/10.1021/jp993187t>.
- Cao, Fei, and Gerko Oskam. 1995. “A Solid State, Dye Sensitized Photoelectrochemical Cell.” *The Journal of Physical Chemistry* 99(47): 17071–73. <http://pubs.acs.org/doi/pdf/10.1021/j100047a003>.
- Carrasco-Orozco, Miguel et al. 2006. “New Photovoltaic Concept: Liquid-Crystal Solar Cells Using a Nematic Gel Template.” *Advanced Materials* 18(13): 1754–58. <http://onlinelibrary.wiley.com/doi/10.1002/adma.200502008/epdf>.
- Çavuş, S, and E Durgun. 2016. “Poly (Vinyl Alcohol) Based Polymer Gel Electrolytes : Investigation on Their Conductivity and Characterization.” *Acta Physica Polonica A* 129(4): 621–24. <http://przyrbwn.icm.edu.pl/APP/PDF/129/a129z4p052.pdf>.
- Chandra, S, B B Srivastava, and Neeraj Khare. 1986. “Liquid Crystal Assisted Photoelectrochemical Solar Cell With Chlorophyll Photoelectrode.” *Molecular Crystals and Liquid Crystals* 132(3–4): 265–74. <http://www.tandfonline.com/doi/abs/10.1080/00268948608079547>.
- Chandrasekhar, S. 1992. *Liquid Crystals*. Cambridge University Press.
- Chen, Song et al. 2014. “Dielectric Effect on the Photovoltage Loss in Organic Photovoltaic Cells.” *Advanced Materials* 26(35): 6125–31. <http://onlinelibrary.wiley.com/doi/10.1002/adma.201401987/full>.
- Chen, Yu, Shaoqing Zhang, Yue Wu, and Jianhui Hou. 2014. “Molecular Design and Morphology Control towards Efficient Polymer Solar Cells Processed Using Non-Aromatic and Non-Chlorinated Solvents.” *Advanced Materials* 26(17): 2744–49.

- <http://onlinelibrary.wiley.com/doi/10.1002/adma.201304825/full>.
- Cho, Chungyeon, Ju-Won Jeon, Jodie L Lutkenhaus, and Nicole S Zacharia. 2013. "Electric Field Induced Morphological Transitions in Polyelectrolyte Multilayers." *ACS applied materials & interfaces* 5(11): 4930–36.
<http://pubs.acs.org/doi/pdf/10.1021/am400667y>.
- Coles, Harry, and Stephen Morris. 2010. "Liquid-Crystal Lasers." *Nature Photonics* 4(10): 676–85. <http://dx.doi.org/10.1038/nphoton.2010.184>.
- Contoret, Adam. et al. 2001. "Electroluminescent Liquid Crystals." *Molecular Crystals and Liquid Crystals* 368(1): 271–78.
<http://www.tandfonline.com/doi/abs/10.1080/10587250108029956>.
- Costa, M. R., R. a. C. Altafim, and a. P. Mammanna. 2001. "Ionic Impurities in Nematic Liquid Crystal Displays." *Liquid Crystals* 28(12): 1779–83.
<http://www.tandfonline.com/doi/abs/10.1080/02678290110078757>.
- Cupelli, Daniela et al. 2009. "Self-Adjusting Smart Windows Based on Polymer-Dispersed Liquid Crystals." *Solar Energy Materials and Solar Cells* 93(11): 2008–12.
<http://dx.doi.org/10.1016/j.solmat.2009.08.002>.
- Dam, Tapabrata et al. 2014. "Observation of Ionic Transport and Ion-Coordinated Segmental Motions in Composite (Polymer-Salt-Clay) Solid Polymer Electrolyte." *Ionics* 21(2): 401–10. <http://link.springer.com/article/10.1007/s11581-014-1181-5>.
- Dell'Orto, Elisa, Luisa Raimondo, Adele Sassella, and Alessandro Abboto. 2012. "Dye-Sensitized Solar Cells: Spectroscopic Evaluation of Dye Loading on TiO₂." *Journal of Materials Chemistry* 22(22): 11364. <http://xlink.rsc.org/?DOI=c2jm30481c>.
- Diederichsen, Kyle M, Hilda G Buss, and Bryan D. McCloskey. 2017. "The Compensation Effect in the Vogel–Tammann–Fulcher (VTF) Equation for Polymer-Based Electrolytes." *Macromolecules*: acs.macromol.7b00423.
<http://pubs.acs.org/doi/abs/10.1021/acs.macromol.7b00423>.
- Ding, Xiaokang, and Kun-Lin Yang. 2012. "Liquid Crystal Based Optical Sensor for Detection of Vaporous Butylamine in Air." *Sensors and Actuators B: Chemical* 173: 607–

13. <http://www.sciencedirect.com/science/article/pii/S0925400512007472>.
- Doane, J. W. et al. 1988. "Polymer Dispersed Liquid Crystals for Display Application." *Molecular Crystals and Liquid Crystals Incorporating Nonlinear Optics* 165(1): 511–32.
<http://www.tandfonline.com/doi/abs/10.1080/00268948808082211>.
- Du, F., H. L. Duan, C. Y. Xiong, and J. X. Wang. 2015. "Substrate Wettability Requirement for the Direct Transfer of Graphene." *Applied Physics Letters* 107(14): 1–4.
<http://dx.doi.org/10.1063/1.4932655>.
- Dunmur, D. A., and K. Toriyama. 1995. "Dipole-Dipole Association of Polar Molecules in a Non-Polar Liquid Crystal Solvent." *Molecular Crystals and Liquid Crystals* 198: 201–13.
<http://www.tandfonline.com/doi/abs/10.1080/10587259508037307>.
- Dutt, Sunil, Prem Felix Siril, and Samy Remita. 2017. "Swollen Liquid Crystals (SLCs): A Versatile Template for the Synthesis of Nano Structured Materials." *RSC Adv.* 7(10): 5733–50. <http://xlink.rsc.org/?DOI=C6RA26390A>.
- Fang, Jian et al. 2016. "Enhancement of Ion Dynamics in Organic Ionic Plastic Crystal / PVDF Composite Electrolytes." : 9873–80.
- Ferguson, James. 1973. "Display Devices Utilizing Liquid Crystal Light Modulation." : 1–10. <http://www.google.co.uk/patents/US3731986>.
- Finkelmann, Heino et al. 2001. "Tunable Mirrorless Lasing in Cholesteric Liquid Crystalline Elastomers." *Adv. Mater.* 13(14): 1069–72.
[http://onlinelibrary.wiley.com/doi/10.1002/1521-4095\(200107\)13:14%3C1069::AID-ADMA1069%3E3.0.CO;2-6/epdf](http://onlinelibrary.wiley.com/doi/10.1002/1521-4095(200107)13:14%3C1069::AID-ADMA1069%3E3.0.CO;2-6/epdf).
- Frank, Frederick C. 1958. "I. Liquid Crystals. On the Theory of Liquid Crystals." *Discussions of the Faraday Society* 25: 19–28.
<http://pubs.rsc.org/en/content/articlepdf/1958/df/df9582500019>.
- Franklin, Jeffery, and Zhi Yuan Wang. 2002. "Refractive Index Matching: A General Method for Enhancing the Optical Clarity of a Hydrogel Matrix." *Chemistry of Materials* 14(11): 4487–89. <http://pubs.acs.org/doi/abs/10.1021/cm025541x>.
- Fréedericksz, Vsevolod, and V Zolina. 1933. "Forces Causing the Orientation of an

- Anisotropic Liquid.” *Transactions of the Faraday Society* 29(140): 919–30.
<http://pubs.rsc.org/en/content/articlelanding/1933/tf/tf9332900919#!divAbstract>.
- Funahashi, Masahiro. 2009. “Development of Liquid-Crystalline Semiconductors with High Carrier Mobilities and Their Application to Thin-Film Transistors.” *Polymer Journal* 41(6): 459–69.
<http://www.nature.com/pj/journal/v41/n6/abs/pj200978a.html>.
- Funahashi, Masahiro, and Jun-ichi Hanna. 2000. “High Ambipolar Carrier Mobility in Self-Organizing Terthiophene Derivative.” *Applied Physics Letters* 76(18): 2574.
<http://scitation.aip.org/content/aip/journal/apl/76/18/10.1063/1.126412> (August 19, 2014).
- Gardiner, D J, and H J Coles. 2006. “Highly Anisotropic Conductivity in Organosiloxane Liquid Crystals.” *Journal of Applied Physics* 100(12): 124903.
<http://scitation.aip.org/content/aip/journal/jap/100/12/10.1063/1.2398081>.
- Geary, J. M., J. W. Goodby, A. R. Kmetz, and J. S. Patel. 1987. “The Mechanism of Polymer Alignment of Liquid-Crystal Materials.” *Journal of Applied Physics* 62(10): 4100–4108. <http://aip.scitation.org/doi/abs/10.1063/1.339124>.
- Gi-Dong, Lee. 2010. “Homeotropic Aligned Liquid Crystal Molecules in Dye-Sensitized Solar Cell for High Efficiency.” *Journal of the Korean Physical Society* 56(5): 1519.
- Golodnitsky, D. et al. 2004. “New Generation of Ordered Polymer Electrolytes for Lithium Batteries.” *Electrochemical and Solid-State Letters* 7(11): A412.
<http://esl.ecsdl.org/content/7/11/A412.full>.
- Gong, J., K. Sumathy, and J. Liang. 2012. “Polymer Electrolyte Based on Polyethylene Glycol for Quasi-Solid State Dye Sensitized Solar Cells.” *Renewable Energy* 39(1): 419–23. <http://www.sciencedirect.com/science/article/pii/S0960148111003983> (July 22, 2014).
- Green, Martin A et al. 2014. “Solar Cell Efficiency Tables (Version 44).” *Progress in Photovoltaics Research and Applications* 7(22): 701–10.
<http://onlinelibrary.wiley.com/doi/10.1002/pip.2525/abstract>.

- Greenham, Neil C. 2013. "Polymer Solar Cells." *Philosophical Transactions of the Royal Society of London A: Mathematical, Physical and Engineering Sciences* 371(1996): 1–11.
<http://rsta.royalsocietypublishing.org/content/371/1996/20110414>.
- Gu, G Y et al. 2000. "2-Methoxyethyl (Methyl) Carbonate-Based Electrolytes for Li-Ion Batteries." *Electrochimica Acta* 45(19): 3127–39.
<http://www.sciencedirect.com/science/article/pii/S0013468600003947>.
- Hagfeldt, Anders et al. 2010. "Dye-Sensitized Solar Cells." *Chemical Reviews* 110(11): 6595–6663. <http://pubs.acs.org/doi/full/10.1021/cr900356p>.
- Halme, Janne, Paula Vahermaa, Kati Miettunen, and Peter Lund. 2010. "Device Physics of Dye Solar Cells." *Advanced Materials* 22(35): E210–34.
<http://onlinelibrary.wiley.com/doi/10.1002/adma.201000726/abstract> (August 1, 2014).
- Hiltrop, K., J. Hasse, and H. Stegemeyer. 1994. "On the Alignment of Thermotropic Nematic and Smectic Liquid Crystals on Lecithin Coated Surfaces." *Berichte der Bunsengesellschaft für physikalische Chemie* 98(2): 209–13.
<http://doi.wiley.com/10.1002/bbpc.19940980213>.
- Högberg, Daniel et al. 2014. "Nanostructured Two-Component Liquid-Crystalline Electrolytes for High-Temperature Dye-Sensitized Solar Cells." *Chemistry of Materials* 26(22): 6496–6502. <http://pubs.acs.org/doi/full/10.1021/cm503090z>.
- Hong, Jin Yong et al. 2016. "A Rational Strategy for Graphene Transfer on Substrates with Rough Features." *Advanced Materials* 28(12): 2382–92.
<http://onlinelibrary.wiley.com/doi/10.1002/adma.201505527/full>.
- Horowitz, Gilles. 1998. "Organic Field-Effect Transistors." *Advanced Materials* 10(5): 365–77. [http://onlinelibrary.wiley.com/doi/10.1002/\(SICI\)1521-4095\(199803\)10:5%3C365::AID-ADMA365%3E3.0.CO;2-U/epdf](http://onlinelibrary.wiley.com/doi/10.1002/(SICI)1521-4095(199803)10:5%3C365::AID-ADMA365%3E3.0.CO;2-U/epdf).
- Hwang, Kyung-Jun et al. 2014. "Light-Penetration and Light-Scattering Effects in Dye-Sensitised Solar Cells." *New J. Chem.* 38(12): 6161–67.
<http://pubs.rsc.org/en/Content/ArticleLanding/2014/NJ/c4nj01459f#!divAbstract>.

- Ileperuma, Oliver a., G.R. Asoka Kumara, Hong-Sheng Yang, and Kenji Murakami. 2011. "Quasi-Solid Electrolyte Based on Polyacrylonitrile for Dye-Sensitized Solar Cells." *Journal of Photochemistry and Photobiology A: Chemistry* 217(2–3): 308–12.
<http://www.sciencedirect.com/science/article/pii/S1010603010004508> (August 19, 2014).
- Jovanovski, Vasko et al. 2005. "Novel Polysilsesquioxane - I-/I₃ - Ionic Electrolyte for Dye-Sensitized Photoelectrochemical Cells." *Journal of Physical Chemistry B* 109(30): 14387–95. <http://pubs.acs.org/doi/full/10.1021/jp051270c?src=recsys>.
- Kamei, Hirotake, Yoshiro Katayama, and Takeo Ozawa. 1972. "Photovoltaic Effect in the Nematic Liquid Crystal." *Japanese Journal of Applied Physics* 11(9): 1385–86.
<http://iopscience.iop.org/article/10.1143/JJAP.11.1385>.
- Kang, S.-W., S.-H. Jin, L.-C. Chien, and S. Sprunt. 2004. "Spatial and Orientational Templating of Semiconducting Polymers in a Cholesteric Liquid Crystal." *Advanced Functional Materials* 14(4): 329–34.
<http://onlinelibrary.wiley.com/doi/10.1002/adfm.200305083/full>.
- Kapernaum, Nadia et al. 2012. "Formation of Smectic Phases in Binary Liquid Crystal Mixtures with a Huge Length Ratio." *Beilstein Journal of Organic Chemistry* 8: 1118–25.
<http://www.beilstein-journals.org/bjoc/content/pdf/1860-5397-8-124.pdf>.
- Karanikolos, Georgios N et al. 2005. "Templated Synthesis of ZnSe Nanostructures Using Lyotropic Liquid Crystals." *Nanotechnology* 16(10): 2372–80.
- Karat, P. P., and N. V. Madhusudana. 1976. "Elastic and Optical Properties of Some 4'-N-Alkyl-4-Cyanobiphenyls." *Molecular Crystals and Liquid Crystals* 36(1–2): 51–64.
<http://dx.doi.org/10.1080/00268947608084830>.
- Karim, Md. Anwarul et al. 2010. "Development of Liquid Crystal Embedded in Polymer Electrolytes Composed of Click Polymers for Dye-Sensitized Solar Cell Applications." *Dyes and Pigments* 86(3): 259–65.
<http://www.sciencedirect.com/science/article/pii/S0143720810000197> (April 11, 2013).
- Kato, Takashi. 2002. "Self-Assembly of Phase-Segregated Liquid Crystal Structures." *Science*

- (*New York, N.Y.*) 295(5564): 2414–18.
<http://science.sciencemag.org/content/295/5564/2414>.
- Katsaros, G et al. 2002. “A Solvent-Free Composite Polymer / Inorganic Oxide Electrolyte for High Efficiency Solid-State Dye-Sensitized Solar Cells.” 149: 191–98.
<http://www.sciencedirect.com/science/article/pii/S1010603002000278>.
- Kim, Dae Woo, Yun Ho Kim, Hyeon Su Jeong, and Hee-Tae Jung. 2011. “Direct Visualization of Large-Area Graphene Domains and Boundaries by Optical Birefringency.” *Nature Nanotechnology* 7(1): 29–34.
<http://www.nature.com/nnano/journal/v7/n1/pdf/nnano.2011.198.pdf>.
- Kim, Sung Chul et al. 2009. “Liquid Crystals Embedded in Polymeric Electrolytes for Quasi-Solid State Dye-Sensitized Solar Cell Applications.” *Macromolecular Chemistry and Physics* 210(21): 1844–50. <http://doi.wiley.com/10.1002/macp.200900289> (April 11, 2013).
- Koh, Teck Ming et al. 2013. “Photovoltage Enhancement from Cyanobiphenyl Liquid Crystals and 4-Tert-Butylpyridine in Co(II/III) Mediated Dye-Sensitized Solar Cells.” *Chemical Communications* 49(80): 9101–3.
<http://pubs.rsc.org/en/Content/ArticleLanding/2013/CC/C3CC43892A#!divAbstract> (August 18, 2014).
- Komiya, Ryoichi et al. 2004. “Highly Efficient Quasi-Solid State Dye-Sensitized Solar Cell with Ion Conducting Polymer Electrolyte.” *Journal of Photochemistry and Photobiology A: Chemistry* 164(1–3): 123–27.
<http://www.sciencedirect.com/science/article/pii/S101060300400111X> (March 7, 2013).
- Kopp, V I, B Fan, H K Vithana, and a Z Genack. 1998. “Low-Threshold Lasing at the Edge of a Photonic Stop Band in Cholesteric Liquid Crystals.” *Optics letters* 23(21): 1707–9. <https://doi.org/10.1364/OL.23.001707>.
- Kumara, G R A, S Kaneko, M Okuya, and K Tennakone. 2002. “Fabrication of Dye-Sensitized Solar Cells Using Triethylamine Hydrothiocyanate as a CuI Crystal Growth Inhibitor.” *Langmuir* 18(26): 10493–95.

- <http://pubs.acs.org/doi/abs/10.1021/la020421p>.
- Leahy, Michael et al. 2013. *International Energy Outlook 2013*.
<http://www.eia.gov/outlooks/archive/ieo13/>.
- Leones, R. et al. 2014. “Chitosan and Ionic Liquid Based Solid Polymer Electrolytes: The Anion Alkyl Chain Length Effect.” *ECS Transactions* 61(14): 51–59.
<http://ecst.ecsdl.org/content/61/14/51.abstract>.
- Leones, Rita et al. 2015. “Effect of the Alkyl Chain Length of the Ionic Liquid Anion on Polymer Electrolytes Properties.” *Electrochimica Acta* 184: 171–78.
<http://dx.doi.org/10.1016/j.electacta.2015.09.163>.
- Li, Lu-Lin, and Eric Wei-Guang Diao. 2013. “Porphyrin-Sensitized Solar Cells.” *Chemical Society reviews* 42(1): 291–304.
<http://pubs.rsc.org/en/content/articlelanding/2013/cs/c2cs35257e> (July 15, 2014).
- Liao, Hsueh Chung et al. 2013. “Additives for Morphology Control in High-Efficiency Organic Solar Cells.” *Materials Today* 16(9): 326–36.
<http://dx.doi.org/10.1016/j.mattod.2013.08.013>.
- Liu, Yongsheng et al. 2013. “Solution-Processed Small-Molecule Solar Cells: Breaking the 10% Power Conversion Efficiency.” *Scientific reports* 3: 3356.
<http://www.nature.com/articles/srep03356> (July 9, 2014).
- Ma, Shou Yuan et al. 2012. “Morphological Modification Induced by External Electric Field during Solution Process of Organic Solar Cells.” *Organic Electronics: physics, materials, applications* 13(2): 297–301. <http://dx.doi.org/10.1016/j.orgel.2011.11.009>.
- Maekawa, Hideki et al. 2004. “Size-Dependent Ionic Conductivity Observed for Ordered Mesoporous Alumina-LiI Composite.” *Solid State Ionics* 175(1–4): 281–85.
<http://www.sciencedirect.com/science/article/pii/S0167273804006101>.
- Majewski, Pawel W. et al. 2010. “Anisotropic Ionic Conductivity in Block Copolymer Membranes by Magnetic Field Alignment.” *Journal of the American Chemical Society* 132(49): 17516–22. <http://pubs.acs.org/doi/abs/10.1021/ja107309p>.
- Mathew, Simon et al. 2014. “Dye-Sensitized Solar Cells with 13% Efficiency Achieved

- through the Molecular Engineering of Porphyrin Sensitizers.” *Nature Chemistry* 6(3): 242–47. <http://www.nature.com/doi/10.1038/nchem.1861>.
- Matsuhiro, Kikuo, and Yoichi Takaoka. 1996. “A Dye Sensitized TiO₂ Photoelectrochemical Polymer Solid Electrolyte.” *Solid State Ionics* 89(3–4): 263–67. <http://www.sciencedirect.com/science/article/pii/0167273896003475>.
- Mercuri, F., M. Marinelli, U. Zammit, and F. Scudieri. 1998. “Thermal Conductivity and Thermal Diffusivity Anisotropy in a Liquid Crystal.” *Journal of Thermal Analysis and Calorimetry* 52(3): 739–44. <http://link.springer.com/10.1023/A:1010102304781>.
- Mie, Gustav. 1908. “Beiträge Zur Optik Trüber Medien, Speziell Kolloidaler Metallösungen.” *Annalen der Physik* 330(3): 377–445. <http://onlinelibrary.wiley.com/doi/10.1002/andp.19083300302/abstract>.
- Miesowicz, M. 1946. “The Three Coefficients of Viscosity of Anisotropic Liquids.” *Nature* 158: 27. <http://www.nature.com/nature/journal/v158/n4001/abs/158027b0.html>.
- Miyamoto, Teruo, and Kyoichi Shibayama. 1973. “Free-Volume Model for Ionic Conductivity in Polymers.” *Journal of Applied Physics* 44(12): 5372–76. <http://aip.scitation.org/doi/abs/10.1063/1.1662158>.
- Morris, Stephen M. et al. 2008. “Polychromatic Liquid Crystal Laser Arrays towards Display Applications.” *Optics Express* 16(23): 18827. <http://www.osapublishing.org/viewmedia.cfm?uri=oe-16-23-18827&seq=0&html=true>.
- Noor, M. M. et al. 2011. “Performance of Dye-Sensitized Solar Cells with (PVDF-HFP)-KI-EC-PC Electrolyte and Different Dye Materials.” *International Journal of Photoenergy* 2011: 1–5. <https://www.hindawi.com/journals/ijp/2011/960487/>.
- O'Regan, Brian, and Michael Grätzel. 1991. “A Low-Cost, High-Efficiency Solar Cell Based on Dye-Sensitized Colloidal TiO₂ Films.” *Nature* 353(6346): 737–40. <http://www.nature.com/nature/journal/v353/n6346/abs/353737a0.html>.
- Oh, Chulwoo, and Michael J. Escuti. 2007. “L-6: Late-News Paper : Achromatic Diffraction Using Reactive Mesogen Polarization Gratings.” *SID Symposium Digest of*

- Technical Papers* 38(1): 1401–4. <http://doi.wiley.com/10.1889/1.2785576>.
- Ohta, Takashi et al. 2004. “Monodomain Film Formation and Lasing in Dye-Doped Polymer Cholesteric Liquid Crystals.” *Japanese Journal of Applied Physics* 43(9R): 6142–44. <http://iopscience.iop.org/article/10.1143/JJAP.43.6142>.
- Oliver, Scott R J, and Geoffrey A Ozin. 1998. “Phosphate Liquid Crystals: Novel Supramolecular Template for the Synthesis of Lamellar Aluminophosphates with Natural Form.” *Journal of Materials Chemistry* 8(4): 1081–85. <http://pubs.rsc.org/en/Content/ArticleLanding/1998/JM/A708598B#!divAbstract>.
- Osman, Z., Z. A. Ibrahim, and A. K. Arof. 2001. “Conductivity Enhancement due to Ion Dissociation in Plasticized Chitosan Based Polymer Electrolytes.” *Carbohydrate Polymers* 44(2): 167–73. <http://www.sciencedirect.com/science/article/pii/S0144861700002368>.
- Pal, Santanu Kumar, Shilpa Setia, B.S. Avinash, and Sandeep Kumar. 2013. “Triphenylene-Based Discotic Liquid Crystals: Recent Advances.” *Liquid Crystals* 40(12): 1769–1816. <http://www.tandfonline.com/doi/abs/10.1080/02678292.2013.854418> (July 13, 2014).
- Parent, Lucas R. et al. 2012. “Direct in Situ Observation of Nanoparticle Synthesis in a Liquid Crystal Surfactant Template.” *ACS Nano* 6(4): 3589–96. <http://pubs.acs.org/doi/abs/10.1021/nn300671g>.
- Park, Yeong Don, Jung Ah Lim, Hwa Sung Lee, and Kilwon Cho. 2007. “Interface Engineering in Organic Transistors.” *materials to* 10(3): 46–54. <http://www.sciencedirect.com/science/article/pii/S1369702107700196>.
- Penny, Melissa, Troy Farrell, Geoffrey Will, and John Bell. 2004. “Modelling Interfacial Charge Transfer in Dye-Sensitised Solar Cells.” *Journal of Photochemistry and Photobiology A: Chemistry* 164(1–3): 41–46. <http://www.sciencedirect.com/science/article/pii/S1010603004000942>.
- Pouzet, Eric et al. 2009. “Homeotropic Alignment of a Discotic Liquid Crystal Induced by a Sacrificial Layer.” *Journal of Physical Chemistry C* 113(32): 14398–406.

- Que, Ya Ping et al. 2016. "High Open Voltage and Superior Light-Harvesting Dye-Sensitized Solar Cells Fabricated by Flower-like Hierarchical TiO₂ Composed with Highly Crystalline Nanosheets." *Journal of Power Sources* 307: 138–45.
<http://dx.doi.org/10.1016/j.jpowsour.2015.12.061>.
- Raimond, J M et al. 2004. "Electric Field Effect in Atomically Thin Carbon Films." *Science* 306(5696): 666–69. <http://science.sciencemag.org/content/306/5696/666>.
- Reiffenrath, V, J Krause, H J Plach, and G Weber. 1989. "New Liquid-Crystalline Compounds with Negative Dielectric Anisotropy." *Liquid Crystals* 5(1): 159–70.
<http://www.tandfonline.com/doi/pdf/10.1080/02678298908026359>.
- Reinitzer, Friedrich. 1888. "Beiträge Zur Kenntniss Des Cholesterins." *Monatshefte für Chemie und verwandte Teile anderer Wissenschaften* 9(1): 421–41.
<http://dx.doi.org/10.1007/BF01516710>.
- Ren, Y. et al. 2001. "A Dye-Sensitized Nanoporous TiO₂ Photoelectrochemical Cell with Novel Gel Network Polymer Electrolyte." *Journal of Applied Electrochemistry* 31(4): 445–47. <http://link.springer.com/article/10.1023/A:1017523901804>.
- Ryu, Sang-Woog et al. 2005. "Effect of Counter Ion Placement on Conductivity in Single-Ion Conducting Block Copolymer Electrolytes." *Journal of the Electrochemical Society* 152(1): A158–63. <http://jes.ecsdl.org/content/152/1/A158.full>.
- Sakuda, Junji et al. 2015. "Liquid-Crystalline Electrolytes for Lithium-Ion Batteries: Ordered Assemblies of a Mesogen-Containing Carbonate and a Lithium Salt." *Advanced Functional Materials* 25(8): 1206–12.
<http://onlinelibrary.wiley.com/doi/10.1002/adfm.201402509/abstract>.
- Sangiorgi, Alex et al. 2014. "Optimized TiO₂ Blocking Layer for Dye-Sensitized Solar Cells." *Ceramics International* 40(7 PART B): 10727–35.
<http://dx.doi.org/10.1016/j.ceramint.2014.03.060>.
- Schröder, C., M. Haberler, and O. Steinhauser. 2008. "On the Computation and Contribution of Conductivity in Molecular Ionic Liquids." *The Journal of Chemical Physics* 128(13): 134501.
<http://scitation.aip.org/content/aip/journal/jcp/128/13/10.1063/1.2868752>.

- Seki, Shiro et al. 2005. "Distinct Difference in Ionic Transport Behavior in Polymer Electrolytes Depending on the Matrix Polymers and Incorporated Salts." *Journal of Physical Chemistry B* 109(9): 3886–92.
- Serbutoviez, C, J G Kloosterboer, H M J Boots, and F J Touwslager. 1996. "Polymerization-Induced Phase Separation . 2 . Morphology of Polymer-Dispersed Liquid Crystal Thin Films." *Macromolecules* 29(24): 7690–98.
<http://pubs.acs.org/doi/abs/10.1021/ma960293%2B>.
- Sergeyev, Sergey, Wojciech Pisula, and Yves Henri Geerts. 2007. "Discotic Liquid Crystals: A New Generation of Organic Semiconductors." *Chemical Society reviews* 36(12): 1902–29. <http://pubs.rsc.org/en/content/articlehtml/2007/cs/b417320c> (August 19, 2014).
- Shehzad, Muhammad Arslan et al. 2015. "Nematic Liquid Crystal on a Two Dimensional Hexagonal Lattice and Its Application." *Sci Rep* 5: 1–10.
<http://www.nature.com/articles/srep13331>.
- Shi, Guozheng et al. 2015. "Combinative Effect of Additive and Thermal Annealing Processes Delivers High Efficiency All-Polymer Solar Cells." *Journal of Physical Chemistry C* 119(45): 25298–306.
<http://pubs.acs.org/doi/full/10.1021/acs.jpcc.5b08861>.
- Shibata, Y et al. 2003. "Quasi-Solid Dye Sensitised Solar Cells Filled with Ionic Liquid-- Increase in Efficiencies by Specific Interaction between Conductive Polymers and Gelators." *Chemical Communications* (21): 2730–31.
<http://pubs.rsc.org/en/Content/ArticleLanding/2003/CC/b305368g#!divAbstract>.
- Shim, Youngseon, and Hyung J. Kim. 2008. "Dielectric Relaxation, Ion Conductivity, Solvent Rotation, and Solvation Dynamics in a Room-Temperature Ionic Liquid." *Journal of Physical Chemistry B* 112: 11028–38.
<http://pubs.acs.org/doi/abs/10.1021/jp802595r>.
- Shirakawa, Hideki et al. 1988. "Synthesis, Characterization, and Properties of Aligned Polyacetylene Films." *Journal of Macromolecular Science: Part A - Chemistry* 25(5–7): 643–54. <http://www.tandfonline.com/doi/abs/10.1080/00222338808053390> (August 19,

2014).

- Shivanandareddy, Avinash B, Suvratha Krishnamurthy, V Lakshminarayanan, and Sandeep Kumar. 2014. "Mutually Ordered Self-Assembly of Discotic Liquid Crystal-Graphene Nanocomposites." *Chemical communications (Cambridge, England)* 50: 710–12.
<http://www.ncbi.nlm.nih.gov/pubmed/24287783>.
- Sima, Cornelia, Constantin Grigoriu, and Stefan Antohe. 2010. "Comparison of the Dye-Sensitized Solar Cells Performances Based on Transparent Conductive ITO and FTO." *Thin Solid Films* 519(2): 595–97. <http://dx.doi.org/10.1016/j.tsf.2010.07.002>.
- Singh, Shri, and David A Dunmur. 2002. *Liquid Crystals: Fundamentals*. World Scientific.
- Soberats, Bartolome et al. 2015. "Zwitterionic Liquid Crystals as 1D and 3D Lithium Ion Transport Media." *Journal of Materials Chemistry A* 3: 11232–38.
<http://dx.doi.org/10.1039/C5TA00814J>.
- Stathatos, By Elias, Panagiotis Lianos, Angela Surca Vuk, and Boris Orel. 2004. "Optimization of a Quasi-Solid-State Dye-Sensitized Photoelectrochemical Solar Cell Employing a Ureasil/Sulfolane Gel Electrolyte." *Advanced Functional Materials* 14(1): 45–48. <http://onlinelibrary.wiley.com/doi/10.1002/adfm.200304479/abstract>.
- Stephan, A. Manuel. 2006. "Review on Gel Polymer Electrolytes for Lithium Batteries." *European Polymer Journal* 42(1): 21–42.
<http://www.sciencedirect.com/science/article/pii/S0014305705003733> (July 9, 2014).
- Stergiopoulos, Thomas, Evangelia Rozi, Chaido-stefania Karagianni, and Polycarpos Falaras. 2011. "Influence of Electrolyte Co-Additives on the Performance of Dye-Sensitized Solar Cells." *Nanoscale research letters* 6(1): 307.
<http://www.nanoscalereslett.com/content/6/1/307>.
- Subramania, A. et al. 2013. "Effect of Different Compositions of Ethylene Carbonate and Propylene Carbonate Containing Iodide/triiodide Redox Electrolyte on the Photovoltaic Performance of DSSC." *Ionics* 19(11): 1649–53.
<http://link.springer.com/10.1007/s11581-013-0892-3> (August 19, 2014).

- Sun, Kuan et al. 2015. "A Molecular Nematic Liquid Crystalline Material for High-Performance Organic Photovoltaics." *Nature communications* 6: 6013.
<http://www.nature.com/articles/ncomms7013>.
- Taheri, B., A. F. Munoz, P. Palffy-muhoray, and R. Twieg. 2001. "Low Threshold Lasing in Cholesteric Liquid Crystals." *Molecular Crystals and Liquid Crystals Science and Technology. Section A. Molecular Crystals and Liquid Crystals* 358(1): 73–82.
<http://dx.doi.org/10.1080/10587250108028271>.
- Thejo Kalyani, N., and S.J. Dhoble. 2012. "Organic Light Emitting Diodes: Energy Saving Lighting technology—A Review." *Renewable and Sustainable Energy Reviews* 16(5): 2696–2723. <http://www.sciencedirect.com/science/article/pii/S1364032112001153> (July 10, 2014).
- Trashkeev, S I, and A N Kudryavtsev. 2012. "New Type of Thermoelectric Conversion of Energy by Semiconducting Liquid Anisotropic Media." *Arxiv*: 1–10.
<https://arxiv.org/abs/1211.0474>.
- Uchida, Tatsuo. 2014. "40 Years Research and Development on Liquid Crystal Displays." *Japanese Journal of Applied Physics* 53: 1–6.
<http://iopscience.iop.org/article/10.7567/JJAP.53.03CA02/meta>.
- United Nations. 2017. *World Population Prospects: The 2017 Revision, Key Findings and Advance Tables*.
- Wallace, P. R. 1947. "The Band Theory of Graphite." *Physical Review* 71(9): 622–34.
<http://journals.aps.org/pr/abstract/10.1103/PhysRev.71.622>.
- Wang, Caiyun, Dan Li, Chee O. Too, and Gordon G. Wallace. 2009. "Electrochemical Properties of Graphene Paper Electrodes Used in Lithium Batteries." *Chemistry of Materials* 21(13): 2604–6. <http://pubs.acs.org/doi/abs/10.1021/cm900764n>.
- Wang, Mingkui, Carole Grätzel, Shaik M. Zakeeruddin, and Michael Grätzel. 2012. "Recent Developments in Redox Electrolytes for Dye-Sensitized Solar Cells." *Energy & Environmental Science* 5(11): 9394.
<http://pubs.rsc.org/en/Content/ArticleLanding/2012/EE/c2ee23081j#!divAbstract>.

- Wang, Qing et al. 2006. "Characteristics of High Efficiency Dye-Sensitized Solar Cells." *The journal of physical chemistry. B* 110(50): 25210–21.
<http://pubs.acs.org/doi/abs/10.1021/jp064256o>.
- Wang, Shuai et al. 2010. "Graphene as Atomic Template and Structural Scaffold in the Synthesis of Graphene-Organic Hybrid Wire with Photovoltaic Properties." *ACS Nano* 4(10): 6180–86. <http://pubs.acs.org/doi/pdf/10.1021/nn101800n>.
- Watanabe, Kazuyoshi, Kiyoshi Suda, and Kazuo Akagi. 2013. "Hierarchically Self-Assembled Helical Aromatic Conjugated Polymers." *Journal of Materials Chemistry C* 1(16): 2797.
<http://pubs.rsc.org/en/Content/ArticleLanding/2013/TC/C3TC00045A#!divAbstract>.
- Wei, Mingdeng et al. 2006. "Highly Efficient Dye-Sensitized Solar Cells Composed of Mesoporous Titanium Dioxide." *Journal of Materials Chemistry* 16(13): 1287–93.
<http://dx.doi.org/10.1039/b514647j>.
- Woon, Kai L et al. 2006. "Electronic Charge Transport in Extended Nematic Liquid Crystals." *Chem. Mater.* 18(11): 2311–17. [cm0601335.pdf](#).
- Wu, H. M. et al. 1996. "Liquid-Crystal Alignment of Rubbed Polyimide Films: A Microscopic Investigation." *Applied Physics B Laser and Optics* 62(6): 613–18.
<http://link.springer.com/article/10.1007/BF01081700>.
- Wu, Yu-june et al. 2008. "Stereoscopic 3D Display Using Patterned Retarder." *Society for Information Display* 39(1): 260–63.
<http://onlinelibrary.wiley.com/doi/10.1889/1.3069640/abstract>.
- Xie, Wenjing et al. 2015. "Clean Graphene Surface through High Temperature Annealing." *Carbon* 94: 740–48.
<http://www.sciencedirect.com/science/article/pii/S0008622315300695>.
- Xu, Jinlei et al. 2016. "Bilayer Film Electrode of Brookite TiO₂ Particles with Different Morphology to Improve the Performance of Pure Brookite-Based Dye-Sensitized Solar Cells." *Journal of Power Sources* 327: 77–85.
<http://www.sciencedirect.com/science/article/pii/S0378775316308734>.

- Xue, Zhigang, Dan He, and Xiaolin Xie. 2015. "Poly(ethylene Oxide)-Based Electrolytes for Lithium-Ion Batteries." *J. Mater. Chem. A* 3(38): 19218–53.
<http://pubs.rsc.org/en/content/articlelanding/2015/ta/c5ta03471j#!divAbstract>.
- Yang, Guangtao et al. 2011. "Light Scattering Enhanced Photoanodes for Dye-Sensitized Solar Cells Prepared by Carbon spheres/TiO₂ Nanoparticle Composites." *Current Applied Physics* 11(3): 376–81.
<http://www.sciencedirect.com/science/article/pii/S1567173910002622>.
- Yang, Wenxing, Yan Hao, Pedram Ghamgosar, and Gerrit Boschloo. 2016. "Thermal Stability Study of Dye-Sensitized Solar Cells with Cobalt Bipyridyl-based Electrolytes." *Electrochemical acta* 213: 879–86.
<http://dx.doi.org/10.1016/j.electacta.2016.07.112>.
- Yi, Zuo et al. 2014. "Effect of Thermal Annealing on Active Layer Morphology and Performance for Small Molecule Bulk Heterojunction Organic Solar Cells." *Journal of Materials Chemistry C* 2: 7247–55.
<http://pubs.rsc.org/en/Content/ArticleLanding/2014/TC/c4tc00994k#!divAbstract> .
- Yim, C T, and D F R Gilson. 1971. "Orientation of Solute Molecules in Nematic Liquid Crystal Solvents." *Canadian Journal of Chemistry* 49(13): 2345–49.
<http://www.nrcresearchpress.com/doi/abs/10.1139/v71-377#.WFfubfmLTmZ>.
- Yokoyama, Shiyoshi et al. 2006. "Laser Emission from a Polymer-Stabilized Liquid-Crystalline Blue Phase." *Advanced Materials* 18(1): 48–51.
<http://onlinelibrary.wiley.com/doi/10.1002/adma.200501355/abstract>.
- Yoo, Eun Joo et al. 2008. "Large Reversible Li Storage of Graphene Nanosheet Families for Use in Rechargeable Lithium Ion Batteries." *Nano Letters* 8(8): 2277–82.
<http://pubs.acs.org/doi/abs/10.1021/nl800957b>.
- Yu, Hua et al. 2009. "An Efficient and Low-Cost TiO₂ Compact Layer for Performance Improvement of Dye-Sensitized Solar Cells." *Electrochimica Acta* 54(4): 1319–24.
<http://www.sciencedirect.com/science/article/pii/S0013468608011353>.
- Yu, Mingzhe, Gayatri Natu, Zhiqiang Ji, and Yiyang Wu. 2012. "P-Type Dye-Sensitized

- Solar Cells Based on Delafossite CuGaO₂ Nanoplates with Saturation Photovoltages Exceeding 460 mV.” *The Journal of Physical Chemistry Letters* 3(9): 1074–78.
<http://pubs.acs.org/doi/abs/10.1021/jz3003603>.
- Zakerhamidi, M. S., M. H Majles Ara, and A. Maleki. 2013. “Dielectric Anisotropy, Refractive Indices and Order Parameter of W-1680 Nematic Liquid Crystal.” *Journal of Molecular Liquids* 181: 77–81. <http://dx.doi.org/10.1016/j.molliq.2013.02.011>.
- Ze Yu, Nick Vlachopoulos, Mikhail Gorlovb, and Lars Kloo. 2011. “Liquid Electrolytes for Dye-Sensitized Solar Cells.” *Dalton Transactions* 40(40): 10289–10303.
<http://pubs.rsc.org/en/content/articlelanding/2011/dt/c1dt11023c#!divAbstract>.
- Zhang, Chunyang et al. 2015. “Cooperation of Multifunction Composite Structures and Fluorescein for Photovoltaic Performance-Enhanced ZnO-Based Dye-Sensitized Solar Cells.” *Journal of Power Sources* 297: 16–22.
<http://dx.doi.org/10.1016/j.jpowsour.2015.07.092>.
- Zhang, D.W. et al. 2011. “Graphene-Based Counter Electrode for Dye-Sensitized Solar Cells.” *Carbon* 49(15): 5382–88.
<http://www.sciencedirect.com/science/article/pii/S0008622311006440> (July 22, 2014).
- Zhang, Qifeng et al. 2012. “Applications of Light Scattering in Dye-Sensitized Solar Cells.” *Physical Chemistry Chemical Physics* 14(43): 14982.
<http://pubs.rsc.org/en/Content/ArticleLanding/2012/CP/C2CP43089D#!divAbstract>.
- Zhang, Zhuo et al. 2007. “A Blue Electroluminescence Organic Material with Liquid Crystal Property.” *Thin Solid Films* 515(7–8): 3893–97.
<http://www.sciencedirect.com/science/article/pii/S004060900601296X>.
- Zhao, Jingbo et al. 2016. “Efficient Organic Solar Cells Processed from Hydrocarbon Solvents.” *Nature Energy* 1(2): 15027.
<http://www.nature.com/articles/nenergy201527>.
- Zheng, Qiao et al. 2011. “Efficiency Improvement in Organic Solar Cells by Inserting a Discotic Liquid Crystal.” *Solar Energy Materials and Solar Cells* 95(8): 2200–2205.

<http://www.sciencedirect.com/science/article/pii/S0927024811001772> (April 11, 2013).

Zhou, Yanfang et al. 2009. "Improvements of Photocurrent by Using Modified SiO₂ in the Poly(ether Urethane)/poly(ethylene Oxide) Polymer Electrolyte for All-Solid-State Dye-Sensitized Solar Cells." *Chemical Communications* (26): 3895–97.
<http://pubs.rsc.org/en/Content/ArticleLanding/2009/CC/b903877a#!divAbstract>.

Zistler, M. et al. 2006. "Comparison of Electrochemical Methods for Triiodide Diffusion Coefficient Measurements and Observation of Non-Stokesian Diffusion Behaviour in Binary Mixtures of Two Ionic Liquids." *Electrochimica Acta* 52(1): 161–69.
<http://www.sciencedirect.com/science/article/pii/S0013468606005408>.